Vertically Aligned Arrays of InSb Nanostructures for Tuning Light Absorption in the Mid-Infrared

Vertically Aligned Arrays of InSb Nanostructures for Tuning Light Absorption in the Mid-Infrared

Nicholas Collins

A Thesis in the Field of Bioengineering and Nanotechnology

for the Degree of Master of Liberal Arts

Harvard University

March 2018

Abstract

Infrared detection is valuable across a diverse range of fields. Military applications have long been the focus of development of infrared detection technology, but as accessibility to infrared detectors grows, industries ranging from waste management to medicine have shown broad uses for the technology. Imaging of biological samples is particularly well suited for near and mid infrared imaging as opaque superficial layers often inhibit the use of visible light to detect underlying structures which may hold diagnostic value. Infrared detecting devices are typically underutilized in a biomedical setting despite there being many potential applications. The primary objective of this research was to provide a proof of concept for a novel transmission filters system in the near and mid infrared range using vertically oriented indium antimonide (InSb) nanostructures. This was achieved by conducting optical simulations of InSb nanowires, developing an ICP-RIE etching process suitable for InSb, and, lastly, by measuring specular reflectance of the InSb nanostructure arrays using FT-IR microscopy. Optical simulations showed that nanowire diameter will shift spectral response, suggesting that InSb would make a suitable selective filter which can be tuned with geometry. Etching InSb nanostructures with a $CH_4/H_2/Ar$ based ICP-RIE process was shown to minimize re-deposition and tapering, but not to eliminate either. Preliminary data showed that an addition of HBr to the $CH_4/H_2/Ar$ process could potentially mitigate both issues. Finally, an FT-IR microscope was used to measure specular reflectance, and confirmed that spectral response can be tuned with InSb

nanowire dimensions in a 2 μm to 7 μm wavelength range. This confirms that InSb nanowire arrays are a candidate for wavelength specific absorbers which may be able to be used as passive transmission filters or even be developed as active detectors in the future.

Acknowledgments

This thesis has been an exercise in personal and academic growth for which I am very grateful to the entire Habbal lab. To that end, I would like to thank Dr. Fawwaz Habbal, my thesis director, for recognizing this cellular biologist's desire to expand his horizons, and for being generous with his support and guidance, despite being perhaps the busiest person on earth. I would also like to thank Dr. Amit Solanki for his tireless dedication to teaching me and working alongside me throughout this process which had such a steep learning curve. Many thanks are also owed to Dr. Handon Um, who also offered unwavering support during this project. It is hard to express my appreciation for not only the countless hours of help from Amit and Handon, but for the true friendship that has resulted. I must also express my gratitude to the Harvard community, which continues to inspire me, both because of the strength and support of the institution, and because of the diversity of the intellectual community which offers endless opportunity to learn from others across all fields. Lastly, but certainly not least, an enormous thank you to my wife, Caitlin.

Table of Contents

List of Figures

Chapter I.

Introduction

This chapter will introduce the fundamentals and provide the necessary background information for this thesis. It will begin with a description of electromagnetic (EM) waves and their interaction with matter, specifically semiconductors. Next, there will be a brief introduction to photodetectors, followed by an overview of how nanostructures can be used to manipulate light. A review of the state of infrared sensing technology will be provided before, lastly, a proposal of a novel infrared transmission filter system using InSb nanostructures is laid out.

Light and Electromagnetic Waves

To the human eye, light is one of the most readily observable natural phenomenon. At the most primitive level, sensing light can enable organisms to identify objects based on color, size, shape, movements, and to some degree, composition. Some biological systems further rely on light to trigger mechanisms relied upon for survival. Despite these seemingly obvious connections between light and life, the composition and interactions involving light and matter are profoundly complicated. At the present time, a deeper understanding of light, paired with rapidly developing technologies, has enabled unprecedented control over light manipulation, and has vastly transformed the existence of human kind. From creating light sources and detectors to devices capable of converting light to electrical energy, these developments continue to shape our landscape and way of life. After many years of research, it was established that light is EM radiation

consisting of EM waves. Waves can be broadly defined as disturbances in a medium that take the form of vibrations or oscillations. They can be characterized by wavelengths (the distance between crests of the wave), amplitude (the distance between the crest of the wave and the central point of rest), and frequency of the wavelength in a period of time. EM waves are composed of electric and magnetic field components, with one oscillating perpendicularly to the other. Figure 1 illustrates an EM wave with its two orthogonal components. The speed at which EM waves travel has been defined as the 'speed of light', and this speed is constant across the entire spectrum of electromagnetic radiation.

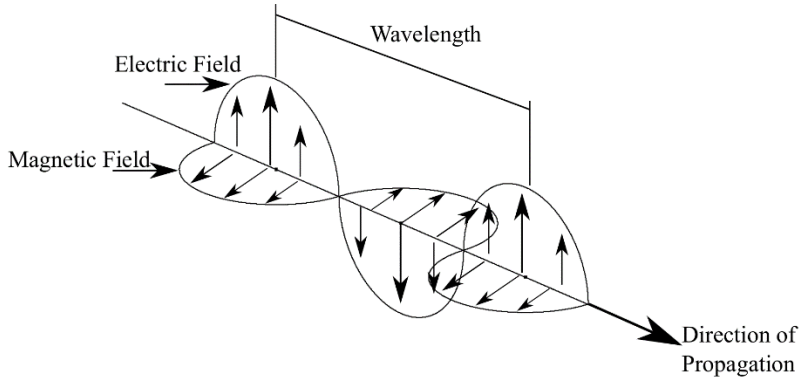

Figure 1. Electromagnetic Wave.
A depiction of an electromagnetic wave composed of an electric field and a magnetic field component which propagate together as they oscillate perpendicularly to each other.

The spectrum of EM radiation ranges from gamma rays to radio waves, which have wavelengths ranging from less than 0.01 nm to more than $1x10^8$ nm respectively. A depiction of the entire electromagnetic spectrum is shown in Figure 2. The area commonly referred to as 'light' has a very broad range, consisting of ultraviolet light,

from 10 nm to 400 nm wavelengths, visible light, from 400 nm to 700 nm wavelengths, and infrared light, with wavelengths ranging from 700 nm to 1 mm wavelengths.

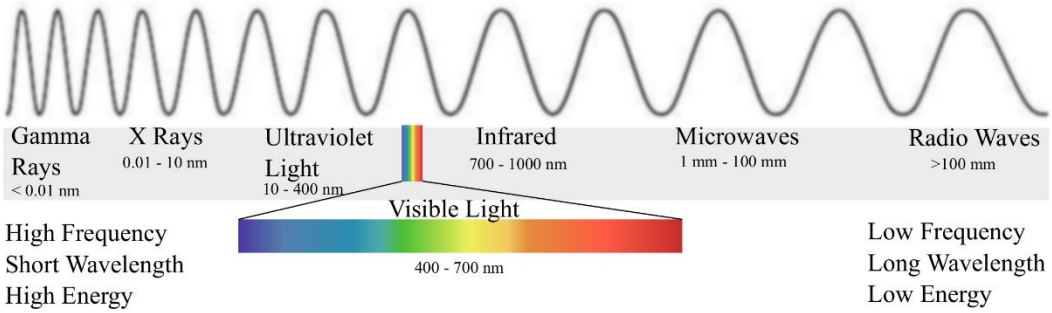

Figure 2. EM wave Spectrum.
The electromagnetic spectrum ranging from gamma rays, with short high energy wavelengths, to radio waves with long low energy wavelengths. The visible range of light is defined by the region sensitive to human eye, ranging from 400 nm to 700 nm. Infrared light follows just after the visible range and spans from 700 nm to 1 mm wavelengths. Figure adapted from (Averill and Eldredge, 2013).

EM waves propagate through a vacuum without energy loss, so long as they do not interact with any matter along the way. When these waves do encounter matter, the material properties will affect the wave's behavior. According to the classical interpretation of electromagnetism, Maxwell's Equations fully describe the propagation and interaction of EM waves in any media.

Maxwell's Equations were developed by combining several experimentally derived laws that help explain the interactions between magnetic-electric fields, currents, and matter. The interactions established by these equations in a stationary frame of reference defined the speed at which an EM wave propagates (determined to be the speed of light), and how that velocity changes when interacting with a material. As seen below, Maxwell's Equations are broken into four parts.

The first equation is known as “Gauss’ Law” and describes how electric fields behave in the presence of electric charge. It expresses that the divergence of electric displacement field ($\nabla \cdot D$) is determined by the charge density in a given volume (ρ_v). The second of Maxwell’s Equations is “Gauss’ Law for Magnetic Fields”. Like Gauss’ Law, the second equation assigns a null value to the divergence of magnetic field ($\nabla \cdot B$). While similar to the first equation, an important distinction is to be made in the magnetic field divergence due to the fact that, in classical electromagnetism, neither a singular magnetic charge nor magnetic monopoles exist, rather, magnetic fields exist as dipoles, always curling around to connect the positive and negative field loops. Due to this balance, the “magnetic charge” enclosed in a region would always equal 0. These interactions are further influenced by the varying material properties in which the interactions take place. Electric displacement current (D) depends on the medium’s permittivity and hence is given by (εE). Similarly, magnetic field density (B) depends on the medium’s permeability and is given by (μH) (Yariv & Yeh, 1984). These are called ‘constitutive equations’ and are listed below as Constitutive Equations 1 and 2.

Maxwell’s third and fourth equations are also closely tied and define how electric and magnetic fields are interrelated. The third law describes how a changing magnetic field ($-\frac{\partial B}{\partial t}$) will induce a curling or rotational electric field denoted by ($\nabla \times$ E). The fourth equation, “Ampere’s Law”, states that either a moving charge in terms of a current flow given by density (J) or a changing electric flux ($\frac{\partial D}{\partial t}$) will induce a rotational magnetic field which is orthogonal to the electric field ($\nabla \times H$) (Yariv & Yeh, 1984). The third and fourth equations ultimately determined that a change in electric field will cause a change in magnetic field and vice versa. Further, considering the “constitutive

equations", it is clear how this set of equations can be used to determine how propagating electromagnetic waves behave as they interact with materials of varying permittivity levels, or "refractive indices". This relationship will be discussed further in a following section. In fact, multiple numerical simulators which solve these equations in 3D are available in commercial or freeware form. We will use one such commercial solver – Lumerical FDTD (finite-difference time-domain) to simulate light interaction in our modelled nanostructures.

$$Maxwell's\ Equations$$

$$(1)\ \nabla \cdot D = \rho_v$$

$$(2)\ \nabla \times B = 0$$

$$(3)\ \nabla \times \mathrm{E} = -\frac{\partial \mathrm{B}}{\partial \mathrm{t}}$$

$$(4)\ \nabla \times H = J + \frac{\partial D}{\partial t}$$

$$Constitutive\ Equations$$

$$(1)\ D = \varepsilon E$$

$$(2)\ B = \mu H$$

Semiconductors, Photodetection, and Nanostructures

Semiconductors

Semiconductors are usually group IV, group III-V or group II-VI compounds. They are intrinsically insulators but have a unique band structure which allows for tuning the conductivity of such material by doping (Seeger, 2004). Metals, such as copper or

aluminum, are classified as conductors for their readily available reservoir of free electrons, therefore providing unrestricted flow of electric current. Insulators, such as silicon dioxide, are attributed with a very low propensity for transferring electric charge. Conductivity depends on the availability of free charge carriers which allow passage of electric current. A solid-state conductor, with some exceptions, will typically have free charge carriers either in conduction or valence band. The abundance of either free electrons or electron-vacancies, called 'holes,' allow for the high electrical conductivity. An insulator will have a full valence band but an empty conduction band, meaning there are no free charge carriers available for conduction. A semiconductor fits in between this classification as it has a band structure with a clear energy gap between the valence which is almost full, and conduction bands, which is nearly empty. A comparison of metal, semiconductor, and insulator band structure is illustrated in Figure 3. The energy required for an electron to transition from the valence to the conduction band is given by the 'band gap'. If a semiconductor receives an adequate energy from an external stimulus, an electron from valence band can jump to the conduction band, where it is no longer bound to an atom and is available for charge conduction. Thus, most semiconductors are intrinsically insulators whose conductivity can be changed by adding energy to the system (e.g. through heat or light).

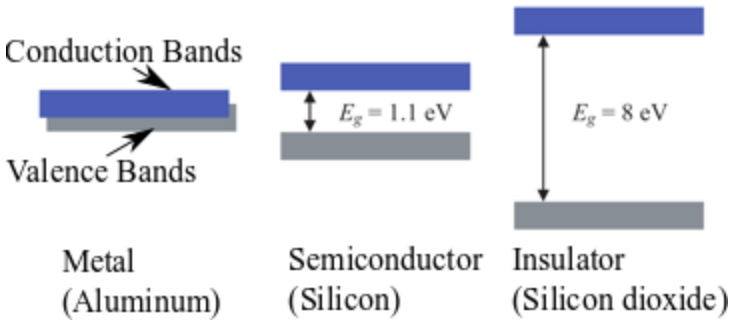

Figure 3. Comparison of Material Band Gaps
A generic illustration of the band gaps of materials from left to right; a metal, such as aluminum, a semiconductor, such as silicon, an insulator, such as silicon dioxide. Figure adapted from (Xiao, 2012).

Electrical conductivity in semiconductors can be further engineered by a process called “doping”. Doping is the process of introducing elemental impurities in a semiconductor. The elements introduced as dopants affect band gap, and if done appropriately will increase conductivity. For example, silicon is commonly doped with phosphorus, which has more valence electrons than silicon, making electrons more readily available to conduct electrical current. When additional electrons are introduced with a dopant, as they are with phosphorus doping, the material is described as n-type. Alternatively, there are p-type materials, where the driving force of increased conductivity results from having a majority of electron holes in the valence band, that is missing electrons which can be represented as the positively charged holes. Doping with an element that provides a hole from its outermost shell, such as boron, will also increase conductivity, as current will be carried by holes.

Photodetection

Because of the unique semiconductor band structure and the ability to engineer conductive properties via doping, semiconductors are widely utilized in the field of photonics. This is evident in the structure of a simple photodiode. Layering a p-type and an n-type material creates a PN junction. The interface of the two materials results in a space-charge or depletion region. This depletion region is formed by diffusion as p-type and n-type materials are brought in contact and the excess electrons in the n-type region rush into the p-type region to satisfy the electron vacancies near the interface. Thus, a region depleted of any free charge carriers is formed at the junction between p and n type region which prohibit further transfer of charge carriers as the system reaches equilibrium. A strong internal electric field is created by these transferring charges and exists only in the depletion region. When enough energy, for example from light, reaches the diode, an increase in voltage will occur from the electron hole pairs generated by the semiconductor, and, due to the electric field generated in the depletion region, an increase current can be measured in the circuit as it current is carried away the junction (Xiao, 2012).

A photodiode is a basic unit found in many electric and optoelectronic devices. The creation of large arrays of semiconductor photodiodes lead to the development of modern image sensors. The color distinction on image sensors is achieved by fabricating optical filters on top of the detection regions. The optical filters are typically organic dyes that will passively select which wavelengths will be transmitted through or reflected away from the sensor. This design results in defined regions which generate electrical

current relative to the intensity of the filtered light reaching the sensing material. Through post -processing steps, a color image can be generated.

The range of detectable light depends on the band gap of the material. Silicon, for example, is the leading material for visible light detection as it has a band gap of 1.1 electron volts (eV). 1.1 eV corresponds to a wavelength of roughly 1100 nm and longer. A lower energy wavelength will not be detectable by silicon (Xiao, 2012). Wavelengths with energy less than the band gap will lack sufficient energy to excite a valence electron enough to move the conductions band. High energy wavelengths also become undetectable due to either absorption very close to the surface and loss of carriers in surface trap states or the energy being too high for the electron stays in the conduction band and leads to photoelectron emission. The latter has its application in ultraviolet/x-ray photoelectron spectroscopy.

While the 1.1 eV band gap of silicon is responsive to the visible range, smaller band gap materials are responsive to much longer, lower energy wavelengths, and materials with larger band gaps are sensitive to ultraviolet, higher energy wavelengths. InSb has a band gap of 0.17 eV which corresponds to a wavelength around 7000 μm, giving InSb a detection range from roughly 1 μm to 7 μm (Rogalski, 2011). This range consists of near and mid-infrared light which is tremendously valuable for detection and has potential applications for security and surveillance or chemical and biological detection. Military focused applications have lead infrared detection development for decades (J. Keller, 2014), and industrial applications have proven useful in cases of identifying materials with specific infrared spectral responses (Vázquez-Guardado, Money, Mckinney, & Chanda, 2015). Biomedical applications are increasingly being

developed because many biomaterials absorb near and mid -infrared light (Wilson et al., 2014). Despite the broad range of potential applications, infrared imaging technology has not advanced nearly as quickly as other imaging technologies, and since much of infrared imaging advancement is geared toward military uses, development for industrial, medical, or civilian uses have lagged. The current state of infrared image sensors remains in many cases prohibitively expensive, and in some cases, has an inadequate spectral resolution. There have been recent reports of infrared detectors that surpassed these hurdles to image inner ear tissues. Medical doctors were limited to using infrared technology as these tissues were not imageable with visible sensors, and previously available infrared sensors were reported to lack the required resolution and be cost prohibitive (Carr, Valdez, Bruns, & Bawendi, 2016).

The current state of infrared detectors spans several materials and embodiments. Thermal sensitive bolometers, which measure thermal radiation with no regard to wavelength specificity, are widely available and can be fabricated with low -cost materials. This results in an affordable large infrared detection range, but with a low photosensitivity which is severely limiting for many applications. Quantum infrared detectors, though more complicated from an engineering perspective, offer wavelength dependent photosensitivity (Rogalski, 2002), which enables these devices to meet the driving market need for higher pixel density and sensitivity. Detector wavelength specificity requires either tuning of the detector material or the inclusion of filters as is commonly used in visible wavelength detectors. This is one of the main factors in the historically prevalent use of mercury-cadmium-telluride (HgCdTe) for infrared detection. Because the band gap of HgCdTe can be adjusted with changes in the mercury and

cadmium composition of the material, it was preferred over materials such as InSb despite it having very similar qualities to HgCdTe (Sprafke & Beletic, 2008). Despite the recent advancements in infrared image sensing, the demand for higher pixel density, higher sensitivity, increased functionality, and a lower cost continues to drive the need for further research and development.

Nanostructures and Photonics

It has been well-documented that nanostructures, particularly semiconductor nanostructures, show novel optical properties when compared to their bulk counterparts. The advancement of nanofabrication tools, techniques in patterning, doping, and interfacing materials permitted many innovations in light emission and detection (Law, Goldberger, & Yang, 2004). The power of nanostructures in photonics lies in the material property changes that occur with changes in dimensionality (Hu, Odom, & Lieber, 1999). Interest in low dimensional structures, such as quantum wells, wires, and dots increased as they were observed exhibited significantly different electrical and optical properties as their bulk material counterparts. These changes are due to altered charge density states, which effects interactions involving, for example, interactions between electron-hole pairs and EM waves (Selçuk, 2009).

Of the many interesting attributes of nanostructured semiconductor materials, nanowires, which have been widely studied, have substantially different absorption spectra relative to that of bulk materials. This effect has been studied in both horizontal nanowires and vertical nanowire arrays and can be attributed to size-dependent optical resonance effects. This change in spectral response is due to a specific resonant frequency, or wavelength, that matches to the geometry of the nanowire. With short

wavelengths, the absorption within a nanowire is highly confined, while a longer wavelength light will leak outside of the nanowire. A trade-off is reached at the resonant wavelength (between short and long wavelengths) where the light couples efficiently to the nanowire and the surround. This concept has been well studied in horizontal nanowires, where wavelength specific resonant modes shifted with changing nanowire diameters. There was also evidence of the role leaky mode resonance played in selective wavelength absorption in nanowires (Cao et al., 2009). Leaky-mode resonance has also been reported as the driving force in selective absorption in vertical nanowire arrays as well. Included in the number of materials applied to this concept are Silicon (Seo et al., 2011), Germanium (Solanki & Crozier, 2014), and compounds such as InAsSb (Svensson, Anttu, Vainorius, Borg, & Wernersson, 2013).

With vertical nanowire arrays, an orderly layout of the nanowires become critical to the absorption behavior of the system. This is due to the fact that along with individual nanowire resonance modes, the modes in the neighboring nanowire can couple with each other to give rise to coupled mode resonances. This coupling depends on the spacing in between nanowires (i.e. the array pitch). Even so, the absorption in fundamental HE_{11} mode plays a dominant role in wavelength selective light absorption in nanowires. This thesis will focus on the identification of this fundamental He_{11} mode of InSb nanowire arrays in the simulations results section. In the experimental section, we will work towards the fabrication of nanowire arrays which show resonant absorption in HE_{11} mode and we aim to achieve a diameter dependent tuning of this absorption from near IR- mid IR range using InSb nanowire arrays.

Indium Antimonide (InSb)

InSb is a III-V semiconductor material with a band gap of 0.17 eV at 300 K, and a very high carrier mobility (Rode, 1971). These are key attributes that make InSb a strong candidate material for infrared detection in the near and mid -infrared range. Single, horizontal InSb nanowires have been shown to be capable of detecting infrared light between 1 μm and 5.5 μm (Chen, Sun, Lai, Meyyappan, & Xi, 2009) (Shafa, Akbar, Gao, Fakhar-E-Alam, & Wang, 2011). Further, there have been reports of vertical nanostructures composed of III-V semiconductors, such as InAsSb (Svensson et al., 2013), InP (Jain et al., 2014), and InAs (Wook Shin et al., 2015), capable of infrared detection. Studies on orderly vertical arrays on InSb are limited, however optical simulations of vertical nanowire arrays composed of several III-V materials, including InSb have reported potential applications in optical devices (Azizur-Rahman & Lapierre, 2016) (Azizur-Rahman & Lapierre, 2015). Further, spectral analysis on grown InSb heterostructures has also supported that specific waveband detection can be tuned by changing nanowire diameter. Given the amount of promising research surrounding nanowire photonic devices in general and the prior studies regarding optical properties of InSb nanowire devices, it easily justified further research.

Proposed Optical System

Vertical InSb Nanowire Transmission Filters

Nanowires have been shown to hold great optical advantages over traditional mesa style micro-structure photodetectors. Diameter and pitch of nanowires arrays can be tuned to achieve high absorption efficiencies at specific wavelengths. This concept has

already proven valuable in many materials such as silicon (Seo et al., 2011), germanium (Solanki & Crozier, 2014), and other III-V semiconductors (Svensson, Anttu, Vainorius, Borg, & Wernersson, 2013). A vertical nanowire system relies on waveguide modes that dictate a structure's light absorbing properties. For any given nanowire, many resonance modes are supported, however, the efficiency of light collection is highest at the first resonant mode i.e. the HE_{11}. When used in conjunction with a photodetector, a nanowire of a certain diameter can act as a selective filter since it has the ability to selectively absorb at a narrow waveband region. Thus, the photodetector beneath the nanowire filter will see a selective response similar to selective response filtered by RBG filters in current CMOS cameras. A matrix of such nanowires filters each absorbing a specific part of the incident light spectrum when used with a monochrome CMOS chip, would allow for multispectral imaging as seen in (Park, 2016). The effectiveness of a material behaving in this capacity depends solely on its optical properties, therefore enabling nanowires of many different materials to be used as selective absorbers across a range of wavelengths. Figure 4 shows how material light absorbing are dictated by the complex refractive index (n and k). The plots of n, the refractive index, and k, the extinction coefficient, shows the change of light attenuation as it moves though a medium, changes relative to the wavelength. This behavior accounts for the dispersion effect that can be observed as a light propagates through a material, for example the visible color spectrum that exists a prism.

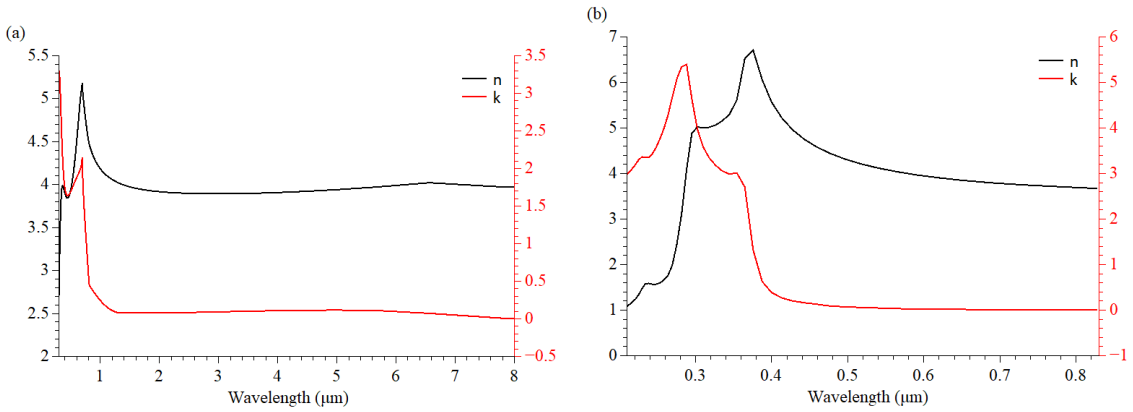

Figure 4. Comparison of InSb and Si n and k

Material optical properties dictate how effective they absorb across a range of wavelengths. (a) n and k of InSb. Data from (Adachi, 1989). (b) n and k of Si. Data from (Green, 2008).

This thesis will focus on the development of vertical nanowire arrays fabricated on a bulk InSb wafer to be spectrally analyzed to confirm the expected optical responses. This research can then transition to freestanding InSb nanowires on an infrared transparent substrate with the intended use being infrared transmission filters, and will further serve as a foundation to advance nanowire-based detection near and mid-infrared light.

This research began with simulations of InSb nanowire arrays to determine appropriate geometries to be fabricated. Developing a fabrication process for dry etching InSb nanowire arrays was then required as dry etching high aspect ratio InSb nanostructures has yet to be achieved. InSb nanowires were then etched directly into an InSb wafer and were used for specular reflection measurements to confirm geometric changes will shift spectral responsivity. The goal of this research, though beyond the scope of this thesis, is to create a novel vertically oriented InSb nanowire -based infrared image sensor. The aim of this thesis is to show InSb as a viable material for selective

light absorption in near-IR to mid-IR range. We achieve this by showing diameter dependent tuning of the reflection spectra from 1 μm to 7 μm wavelengths.

Chapter II.

Research Methods

This chapter contains sections explaining the simulations, fabrication, and analytical methods utilized for this research. The simulation section will explain the why and how the simulations were run. The fabrication section will outline a range of micro and nanofabrication techniques, including the parameters studied during the development of InSb reactive ion etching processes. Lastly, the analytical methods section will explain what tools were used to characterize the fabricated structures and their optical properties.

Optical Simulations of Light Absorption in InSb Nanowires

Software specifically designed for computing light-matter interactions in nanophotonic devices was used to evaluate the proposed InSb nanowire system. This software solves Maxwell's Equations with regard to material data and structure design. These simulations were run to confirm the feasibility of the proposed InSb nanowire transmission filter system. Simulations focus on InSb nanowire structures on top of bulk InSb, so a comparison of spectral response can be made between the simulated data and data measured on fabricated structures. Adapting this embodiment to the proposed transmission filter system would require the InSb nanowires be on top of, or embedded in an infrared transparent material. The feasibility of this adaptation will also be discussed.

Lumerical Mode Solutions and Lumerical FDTD Simulations

Lumerical Mode and FDTD (finite-difference time-domain) Solutions were selected for their targeted application of modal analysis in radial structures and light-matter interactions in nanophotonic devices, respectively. Lumerical Mode Solutions was used to determine waveguiding properties on a two-dimensional level, that is, effectively a cross -section of a nanowire which is infinitely long. These results point to what the optimal resonant frequency is in relation to a specific diameter of an InSb nanowire. The key outcome of these simulations was to identify the wavelength that resonates according to the fundamental HE_{11} mode for each diameter of interest. These results were then applied to more comprehensive simulations using Lumerical FDTD, which considers all aspects of a three-dimensional nanowire array.

Lumerical FDTD applies the Maxwell's Equations to a user -designed photonic system and solves the equations in a user -defined region of the system. Data produced from these computations can be collected at areas of interest by placing monitors within the simulation boundary. The layout of these simulations was created in the CAD environment of Lumerical FDTD. Nanowire geometry, light source position, simulation boundaries, and monitor placements, were all defined in this interface. Figure 5 shows the typical layout used in these simulations.

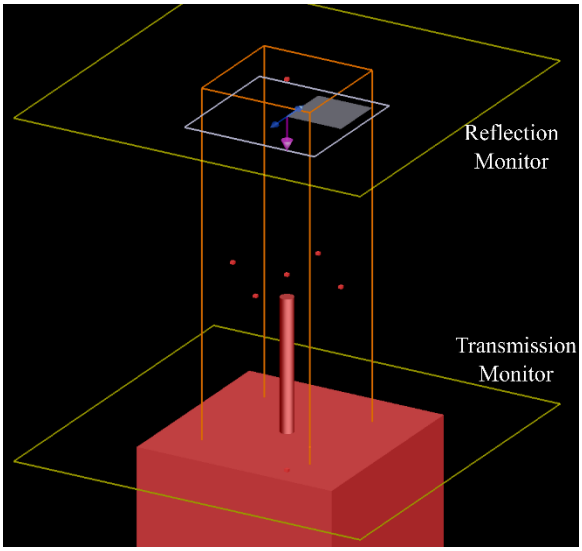

Figure 5. Lumerical FDTD Simulation Model Layout.
A single InSb nanowire stands on an InSb substrate. A source plane wave, white, was placed above the nanowire. Reflection and Transmission monitors, yellow, were placed above and below the nanowire. The 3-dimensional simulation boundary, orange, established the pitch between nanowires.

The nanowire diameter and height were first held constant and the simulation boundary dimensions were varied to change the pitch between nanowires. Simulating several pitches helped determine the optimal nanowire spacing of an array for a diameter. Ideally, we would only like to have a single absorption peak in the nanowire absorption or reflection spectrum. Hence the optimization parameters, for finding the right pitch, is to maximize HE_{11} absorption and to minimize the HE_{12} absorption. Nanowire height optimizations were also studied. The diameter and optimized pitch dimension were held constant and the height was varied. Optimized height values were also studied to understand what height requirements exist to optimize absorption.

Micro and Nanostructure Fabrication

Fabrication Overview

There are many approaches to fabricating micro and nanostructures, and utilizing the correct methods is key for a successful design execution. In broad terms, there are two approaches to fabrication – 'bottom-up' and 'top-down', with the term implying the direction in which a structure is formed. The proposed optical system would require a very fine control over the geometry of the individual nanowires and array. This can be difficult to achieve with bottom -up growth methods. To transmit light efficiently, the InSb system must be unobstructed by any materials that could also manipulate the targeted range of detection, a potential issue as growth methods often form heterostructures.

Beginning fabrication with a top -down approach required creating layers which act as masks to protect patterned regions which form structures during etching. For this research, a hard mask of amorphous silicon was used to etch InSb. To achieve this, a layer of amorphous silicon was deposited on InSb via plasma enhanced chemical vapor deposition (PECVD). For microstructure patterning, basic optical photolithography methods were used. The cured photoresists acted as a mask to etch the Si layer, which results in a -Si micropillar that becomes the hard mask for etching InSb. For nanostructure patterning, electron-beam lithography was used. Either alumina (Al_2O_3) via atomic layer deposition or aluminum via thermal evaporation was then deposited to fill the nano-holes patterned in the resists. These materials act as the mask for etching silicon via deep reactive ion etching (DRIE). The resulting silicon nanowires functioned as the hard mask for InSb etching. Etching both micro and nanostructures of InSb used reactive

ion etching (RIE). InSb structures were then analyzed with scanning electron microscopy (SEM) and energy dispersive spectroscopy (EDS) to make InSb etch process optimizations. An overview of these fabrication process can be seen in Figure 6. Fabrication was carried out in Harvard University's Center for Nanoscale Systems (CNS). The process details are given below.

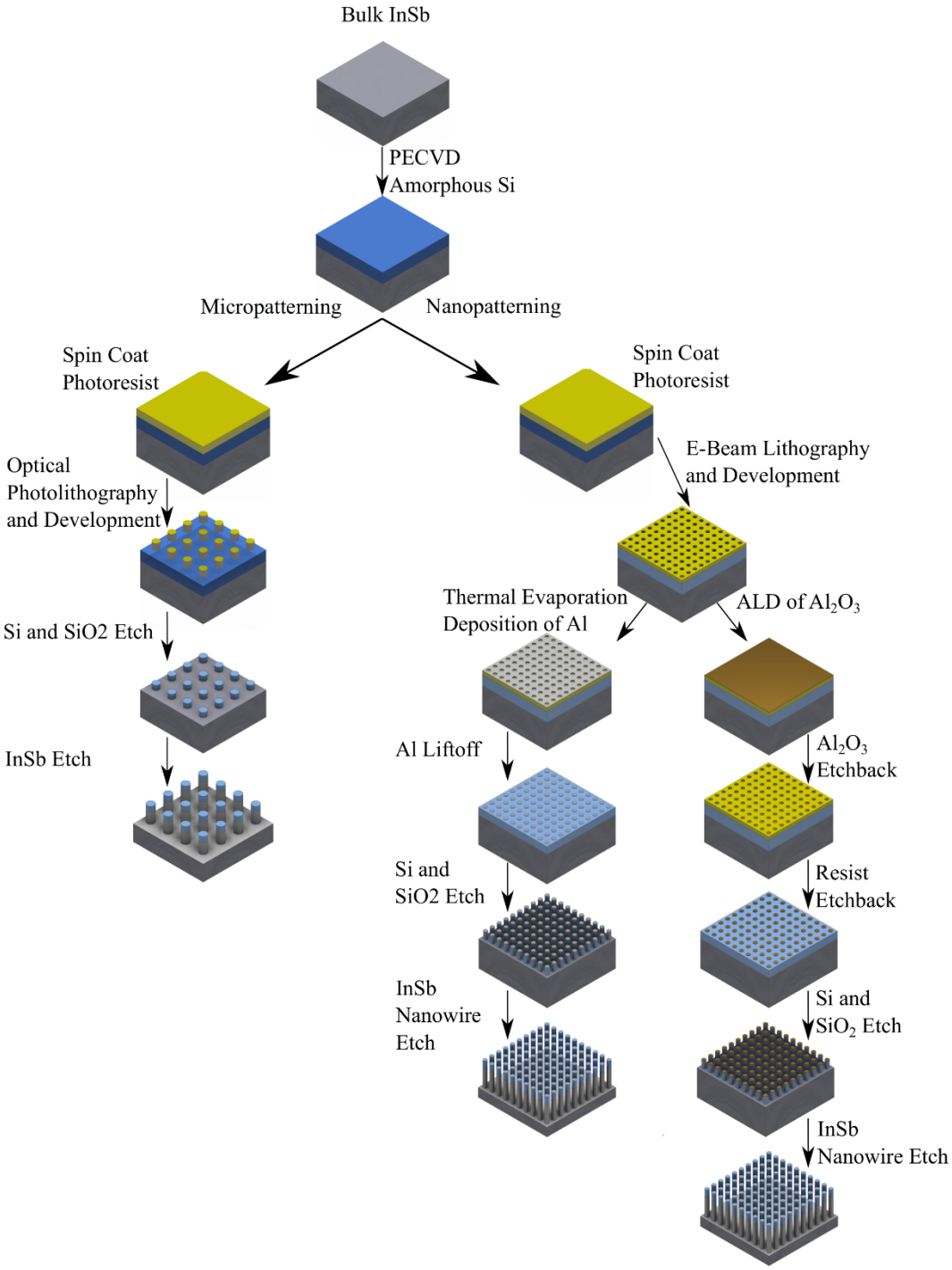

Figure 6. Overview of Fabrication Processes.
Microfabrication and nanofabrication process diverged due to the lithography methods required for nanopatterning. The divergence in deposition technique resulted in the same product, however, the ALD technique is capable of filling smaller features sizes.

Plasma Enhanced Chemical Vapor Deposition (PECVD)

Amorphous-Si was used as a hard mask throughout the fabrication processes, and was deposited on InSb (100) wafers on a STS PECVD system. PECVD utilized a combination of plasma chemistries to deposit solid layers of silicon dioxide and amorphous Si. The process recipe used was previously established and validated. The Si deposition process used SiH_4, NH_3, and N_2 gases. To ensure adequately clean chamber conditions, a 10 minute etch back process was run before loading the InSb sample. The Si deposition process also included a 30 nm layer of silicon dioxide (SiO_2). Without this layer, Si deposition was non-uniform and flaked off the substrate. This is likely caused by a substantial mismatch between the crystal lattices of InSb and Si. Layers deposited by PECVD were analyzed via ellipsometry to ensure the actual thickness was close to the desired thickness.

Optical Photolithography

Standard optical photolithography methods were used in fabricating 2-micron diameter InSb pillars for developing a dry etching process for InSb. Shipley 1813 Photoresist was spin coated at 5000 rpm for 40 seconds (with a 5 second 500 rpm ramp speed) on top of amorphous silicon which was deposited on top of InSb, creating a roughly 1.2 μm thick layer. These samples were then baked at 115° C for 60 seconds on a hotplate. A Suss MJB4 Mask Aligner was used to align a chrome mask containing the 2 μm dot array to the samples, which exposed for 2 seconds with hard contact. Following a post-exposure bake of 60 seconds on a 115° C hotplate, the samples were developed in Microposit MF-319 Developer for 35 seconds, rinsed in water and dried with nitrogen. This process resulted in roughly 1.2 μm tall S1813 pillars. Dose testing and development

time optimizations were completed with bare Si test samples prior to patterning InSb samples.

Electron Beam Lithography

Electron beam lithography was used to write nanoscale features required for nanowire array fabrication. As electron beam lithography writing times can be quite time -consuming, it was a requirement that the dots be written rather than the inverse, so a positive resist was used. A 1:1 mixture of ZEP photoresist and Anisole was used. Samples were cleaned by sonication in acetone for five minutes and rinsed with acetone and isopropyl alcohol, then dried with nitrogen. ZEP/Anisole photoresist was spin coated at 2000 rpm for 40 seconds (with a 5 second, 500 rpm ramp speed), and then annealed at 180° C for 3 minutes. Samples were then mounted onto an Elionix ELS-F125 electron beam lithography sample holder and loaded into the system. Patterns of various diameters and pitches were created using CLE-Win software and imported into the Elionix WecaS software. Nanowire patterns were written with a 500 μm field size, 200,000 dot/field, 450 μCoulombs/cm^2, 1 nanoamperes beam current, and a dose time of 0.02813 μ-seconds. After exposure, samples were developed in O-Xylene for 60 seconds, followed by 30 seconds in 1:3 MIBK:IPA developer, and lastly rinsed in IPA for 30 seconds. This yielded arrays with 150 nm deep holes in the photoresist layer. Dose testing and development optimizations were conducted with Si test samples prior to writing on InSb samples highlighted above.

Deposition and Liftoff

Thermal Evaporation Deposition was used to deposit aluminum after optical lithography as a masking material for Si etching. Samples were mounted on an inverted sample holder via taped edges, which also facilitated better liftoff. A tungsten boat with an alumina coating was clamped to the chamber electrode and loaded with two aluminum pellets with a purity of 99.99%. When an adequate pressure was reached (at or below $2x10^{-6}$ Torr), the boat was heated by slowly increasing current to the boat. Evaporation typically occurred around 90 Amps, and the targeted deposition rate was 0.5 to 1 angstrom per second. The deposition was stopped after roughly 30 nm of aluminum was deposited. Liftoff was achieved by placing samples in Remover PG at 80° C overnight. After 12 to 16 hours, samples were removed, rinsed with IPA, dried with nitrogen. This yielded roughly 30 nm tall aluminum disks which acted masks during silicon etching.

Atomic Layer Deposition (ALD) was used to deposit a masking material on after electron beam lithography. ALD was required to fill the pattern holes with alumina (Al_2O_3). By repeating a sequence of pulsing a precursor gas (trimethylaluminum), followed by purging, then pulsing a reacting gas (water vapor), and purging again, ALD assembles a film one atomic layer at a time. This layer by atomic layer deposition conforms to every surface of a sample, which effectively fills the patterned nanoholes. Since the holes are filled vertically and horizontally at the same rate, a hole of 100 nm diameter will be filled and will join the deposition occurring on the horizontal surface, creating a planar surface. Rather than traditional liftoff, the Al_2O_3 was then etched down just enough to expose the photoresist layer. This left Al_2O_3 filled holes surrounded by cured photoresist, which was

subsequently removed by oxygen plasma treatment. This yielded an approximately 30 nm diameter Al_2O_3 disk on the sample to act as a mask for silicon etching.

Reactive Ion Etching

Reactive ion etching (RIE) was the chosen nanowire fabrication method for several reasons. Dry etching with RIE typically offers greater flexibility in process control than bottom -up growth methods, wet etching, or purely physical ion bombardment etching. Silicon etching process has been developed extensively with RIE, and established processes were used for this research (Huang, Fang, & Zhu, 2007; Seo et al., 2011). RIE has also been used extensively with III-V materials (Pearton, 1996). While dry etched InSb nanowires have yet to fabricated, there was strong support that suitable etching results could be achieved. For example, there have been reports of several InSb etching processes with a variety of etching chemistry, such as methane/hydrogen (Diniz, Swart, Jung, Hong, & Pearton, 1998), chlorine (Vawter & Wendt, 1991), and hydrogen bromide (Pearton et al., 1992).

Silicon Etching was done on a Rapier Deep RIE instrument. A Bosch process using a SF_6/C_4F_8 etching chemistry was used to achieve high aspect ratio, vertical sidewall silicon structures. These structures acted as masked during InSb etching.

Al_2O_3 and Photoresist Etching was etched with an inductively coupled plasma (ICP) RIE system using an O_2 and Ar based process to etch Al_2O_3, and just O_2 to etch the ZEP photoresist layer.

InSb Etching was done on a Unaxis Shuttleline ICP-RIE system. Because prior work only shows micro-scale InSb structures being etched, process development was required to etch InSb nanowires. The initial process parameters that were used were based on several

prior studies (Abautret et al., 2015; Mileham, Lee, Lambers, & Pearton, 1997; Pusino, Xie, Khalid, Thayne, & Cumming, 2016; Zhang, Sun, Xu, & Zhao, 2009). The RIE process developed for etching InSb considered many parameters, which will be highlighted below. The physical layout of the ICP-RIE system used can be seen in Figure 7.

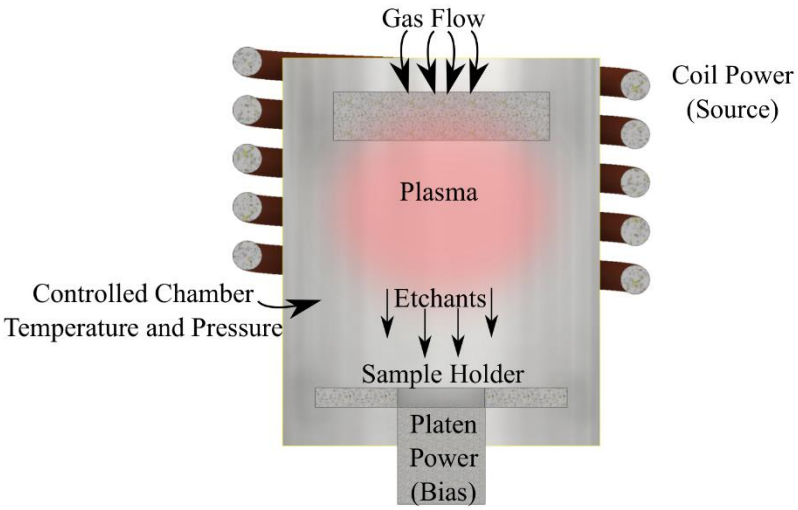

Figure 7. Overview of an ICP-RIE System.
The ICP-RIE system enabled control over the ICP source power, the platen power, chamber pressure, chamber temperature, and gas flow.

Source Power refers to the control over the power of the upper electrode. Increasing the power increases the velocity of electrons in the chamber, causing more frequent collisions between ions and gas molecules. This continues until the number of ions and activated neutral molecules that are formed reach an equilibrium. The density of this plasma is controlled by the source power. This dictates the number of reactive

species available for etching and can help control an anisotropic etch profile, and etch rate.

Chamber pressure can have a large impact on etch rate and anisotropic etching profiles. As pressure decreases in the chamber, it is expected that the mean free path will increase, that is the distance a molecule will travel without colliding into another molecule will increase. This effectively changes the velocity at which the plasma molecules move toward the sample. A higher velocity with fewer collisions will increase an etch rate and decrease isotropic etching effects. However, this can also increase the likelihood of unintentional sputtering from ion bombardment.

Platen Power, or bias power, controls the power of the lower electrode. This electrode is situated just below the sample holder, and is critical in controlling the velocity of the ionized species in the chamber. An increase in this power can cause the ions to travel with higher energy and directionality toward the sample, typically resulting in a faster, more anisotropic etching profile. This has an effect, similar to a decrease in pressure, which can lead to increase in sample sputtering.

Chamber temperature can have a substantial impact on the desorption of etch products. This is due to the fact that the volatility of the etch products is dependent on the process temperature. A product becomes more volatile as it's vapor pressure increases. By increasing temperature, it is expected that there will be better desorption of etch products, and therefore a faster etch rate and a decreased likelihood of re-deposition.

Gas chemistry was another key factor studied while developing the InSb etch process. Gas chemistries can change the mechanism responsible for etching a material. A process can be tuned etch more chemically than physical. Plasma chemistry also dictates

what is etched and what etch products will form. This is particularly useful when etching compounds like InSb as a stoichiometric etch rate can be obtained by control the ratio of etching gases. Some etch products may be more volatile than others, and therefore have improved desorption efficiency. These factors affected etch rates, profiles, micro masking, and re-deposition. Despite several potential etching gas chemistries (Hahn et al., 2000), this research focuses on a CH_4/ H_2/Ar process. This research briefly covers some hydrogen bromide and chlorine -based processes while troubleshooting undesired effects from the CH_4/ H_2/Ar process

Analysis

Analyzing the micro and nanostructures during the RIE process development was required to determine which optimizations were made for etching InSb. The processes were characterized by etch rate, etch profile, surface morphology, and surface composition. After developing a suitable etch process, InSb nanowire arrays with varying diameters and pitches were etched, and analyzed spectrally in the near and mid -infrared range. The methods used for this analysis are highlighted in this section.

Scanning Electron Microscopy

Scanning electron microscopy (SEM) was used to characterize the InSb etch process during development. Etch rates, etch profiles, surface morphologies, and general dimensions were analyzed with SEM and supporting software. Close attention was given to the surface morphology as there were prevalent re-deposition issues while developing the CH_4/ H_2/Ar InSb etch process. SEM data was collected on either a Hitachi SSU5000

or a Zeiss Ultra Plus, with an accelerating voltage of 3 kV, beam current of 5 μA, and a working distance between 3 and 4 mm

Energy Dispersive X-Ray Spectroscopy

As re-deposition free and stoichiometric etching were desired qualities of the etch process, understanding the elemental composition of etched InSb surfaces was key. Because of this, energy dispersive spectroscopy (EDS) was used to better understand re-deposition behavior that was observed from the RIE etch processes. EDS analysis was conducted on a Zeiss Ultra 55 SEM with an accelerating voltage of 10 kV, which targets the L energy levels of both indium and antimony. A working distance of 8.5 mm was used to accommodate the EDS detector on this system. The EDS data was collected with EDAX Genesis software

Spectral Analysis

Due to the fabrication limitation of etching InSb nanowire arrays directly into a bulk InSb wafer, spectral analysis was limited to specular reflection measurements. As, developing free -standing InSb nanowires on an infrared transparent substrate was outside the scope of this thesis, measuring transmission, and then calculating absorption was not possible. However, comparisons between the measured reflectance and simulation data provide strong support for what absorbing behavior is taking place in the InSb nanowire arrays. A Bruker LUMOS FT-IR microscope was used for mid -infrared measurements. Reflection data was collected from 2.5 μm to 7 μm wavelengths.

Chapter III.

Results

This chapter will cover three sections. First, the results from the optical simulations ran on InSb nanowire arrays. Second, the SEM and EDS results from the InSb RIE process development. Lastly, the results from the spectral analysis of InSb nanowire arrays with varying geometries will be covered.

Simulation Results

This section contains optical simulation results from Lumerical Mode Solutions and Lumerical FDTD. The first set of results focus on modal analysis on InSb nanowires, and the second set will consist of optical simulations carried out on 3-dimensions models of InSb nanowire arrays. Lastly, there will be a brief discussion covering how these results support the feasibility of the previously proposed transmission filter system.

Optical Simulations of InSb Nanowires on an InSb Substrate

InSb nanowire arrays with an InSb substrate were simulated to determine the HE_{11} resonant wavelengths for the smallest and largest diameter InSb nanowires. This was to determine the upper and lower limits of detection that can be expected in InSb nanowires. After this range of diameters were selected, a sweep of pitches per each diameter was simulated to find optimal diameter-pitch combinations. When working with leaky resonant modes, too small pitch can have a detrimental effect on the absorption efficiency due to evanescent wave interactions in between nanowires. Optimal conditions were determined at maximum differences in the HE_{11} and HE_{12} absorption peaks. The

HE_{12} modes are secondary, less intense modes, following the HE_{11}. Beyond HE_{12}, a tertiary mode HE_{13}, will begin to resonate as well. For spectrally selective absorbers, an optimal condition would have a larger HE_{11} intensity with minimal HE_{12} or HE_{13} absorption intensity. Lastly, a height sweep of the optimized diameter-pitch for the largest diameter was simulated to determine the minimum effective height which retains optimal absorption efficiency. This provided guidance for required etch depths during the fabrication process

Modal Analysis. It is well understood that nanowires are capable of spectrally selective absorption based on geometry. This absorption is due to wavelength specific resonance modes that fit corresponding nanowire dimensions (Park et al., 2014; Seo et al., 2011; Solanki & Crozier, 2014). A modal analysis was used to better understand this phenomenon in InSb nanowires. First, sweeps of wavelengths were done on 100 nm diameter nanowires. Resonant modes fitting the fundamental HE_{11} mode were unable to be located. However, a 200 nm diameter InSb nanowire fit the HE_{11} mode profile, at approximately 1.3 μm wavelength. Because of this, a 200 nm diameter was established as an effective minimum diameter. A 1000 nm diameter InSb nanowire model was found to resonate with the HE_{11} mode at approximately a 5.8 μm wavelength. This was established as the largest diameter to be used as its proximity to the band gap of InSb. Figure 8 illustrates the electric field distribution in a 200 nm and 1000 nm diameter InSb nanowires at several wavelengths. The center images show the resonant frequencies in accordance with the HE_{11} mode. Around this wavelength is where the light will be optimally absorbed in the upper and lower limit diameters. Wavelengths below this are fit resonant modes which are tightly confined within the structure, and larger wavelengths

show high intensities outside of the nanowire with little to no absorption within the structure. While other resonant modes do fit in these cases, absorption will be significantly greater in the fundamental HE_{11} mode.

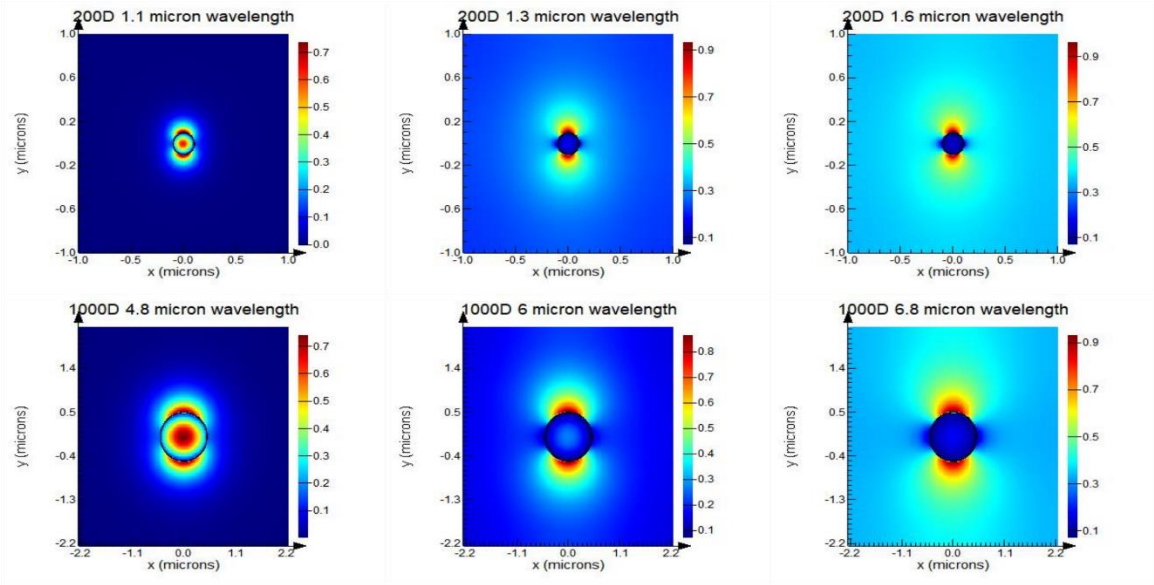

Figure 8. Modal Analysis of InSb Nanowires
The major transverse wave component (Ey) is shown on the top row for a 200 nm diameter InSb nanowire, and the bottom row for a 1000 nm diameter. Wavelengths below the resonant wavelength (left) can be seen tightly confined to the nanowire. Wavelengths greater than the resonant wavelength (right) show fields outside of the nanowire boundary. Resonant wavelengths that match with the fundamental HE_{11} leaky mode (center) show some intensity in the center of the nanowire and coupled to the walls of the nanowires.

Lumerical FDTD Results. Simulations were set up into three sequences. First, simulate a range of pitches to establish the optimal array dimensions. If the nanowires are spaced too far apart, the light would impinge upon the substrate, decreasing the absorption efficiency of the nanowire array. Contrast to this, if the pitch is too small, electric field outside of the nanowire boundaries will be coupled with neighboring nanowires, again decreasing the absorption efficiency of the array. Figure 9 illustrates the

typical pitch sweep for a single diameter nanowire array. The optimal absorption peak can be identified as largest HE_{11} peak relative the smaller, HE_{12} peak to its left. The pitch sweep simulation was done for each nanowire diameter in the range to identify the optimal absorption peaks, and the results can be found in Appendix 1 – Supplementary Figures 1 through 10. The absorption intensity for the pitch optimized nanowire arrays is shown in Figure 10. Figure 11 illustrates the HE_{11} peak intensities for given diameters. Though faint, the absorption in HE_{12} modes for these diameters can be seen as well. It is apparent from these simulations that vertical InSb nanowires can feasibly be used as transmission filters for near and mid-infrared light, as geometric changes result in a shifted spectral response.

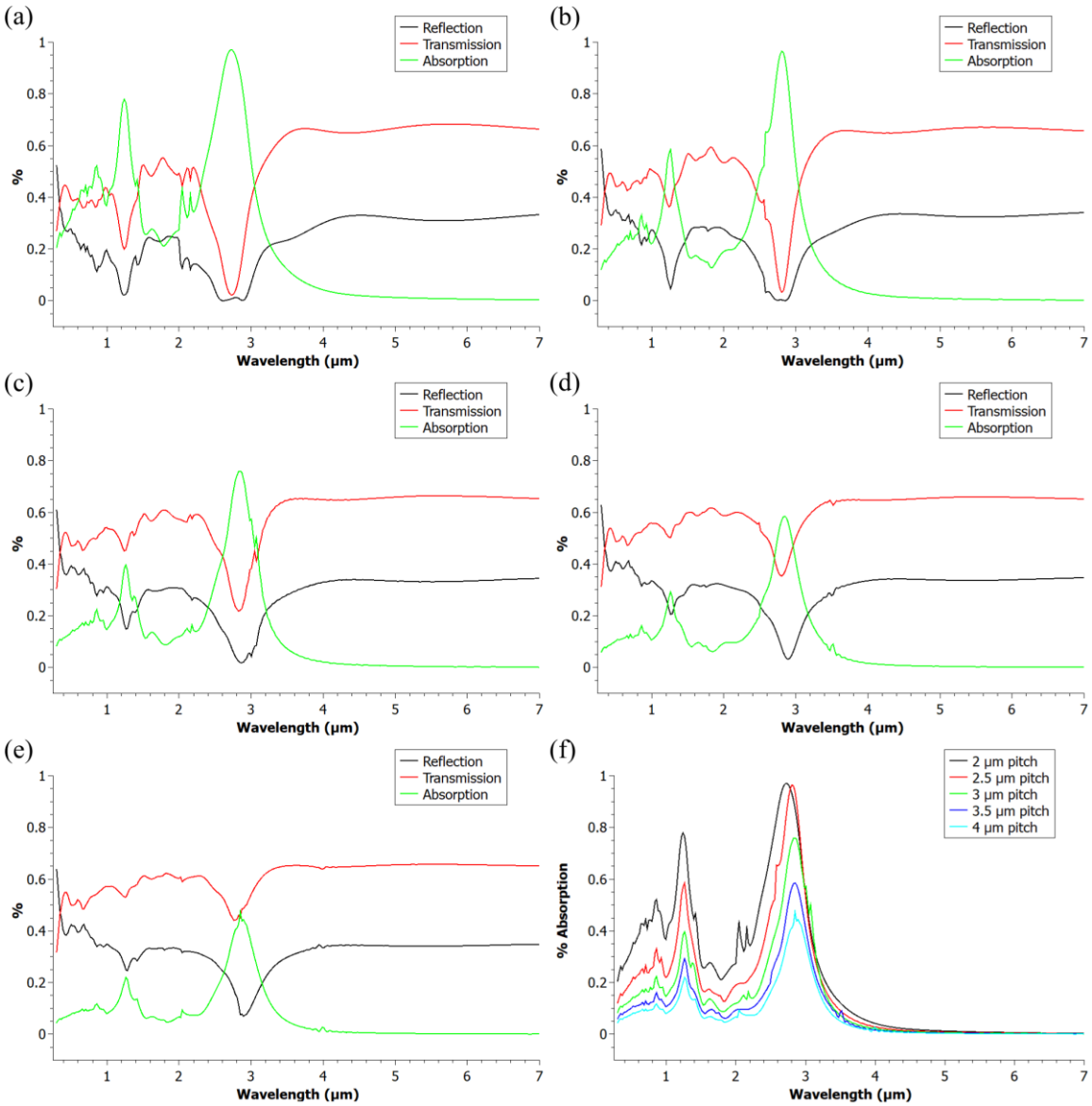

Figure 9. Simulated Spectral Response of a 500 nm Diameter Nanowire Array with Varied Pitch

(a) 2 µm pitch. (b) 2.5 µm pitch. (c) 3 µm pitch. (d) 3.5 µm pitch. (e) 4 µm pitch. (f) Percent absorption for each simulated pitch with a 500 nm diameter.

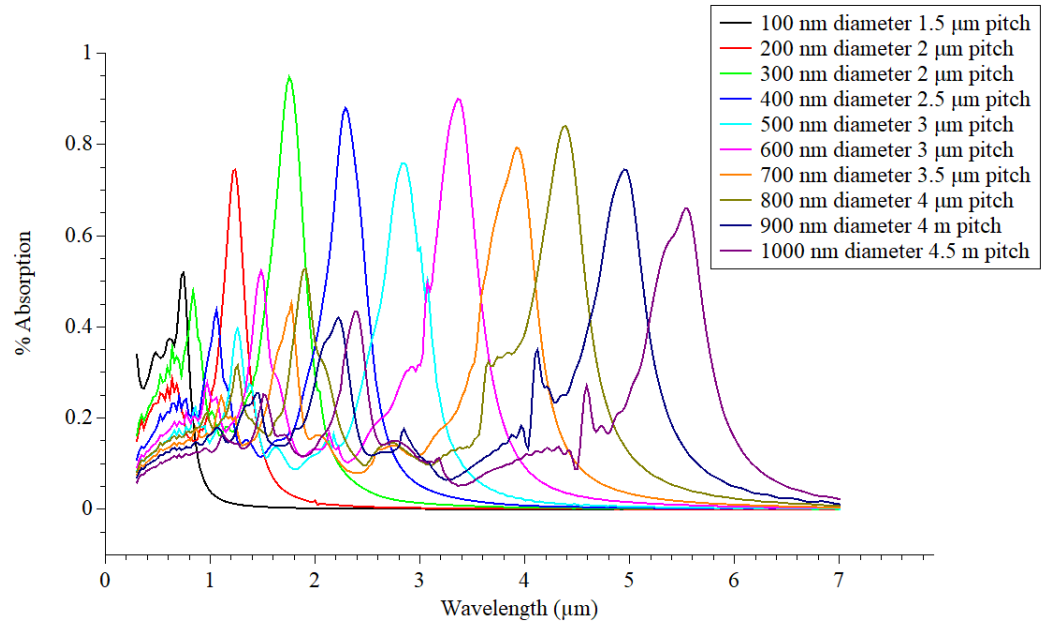

Figure 10. Pitch Optimized Absorption Peaks of InSb Nanowires ranging from 100 nm to 1000 nm in Diameter.

These results indicate the ability to tune InSb nanowire geometry to selectively filter near and mid-infrared wavelengths. The largest peak for each diameter corresponds to the HE_{11} mode, while the small peaks to the left correspond to the HE_{12}.

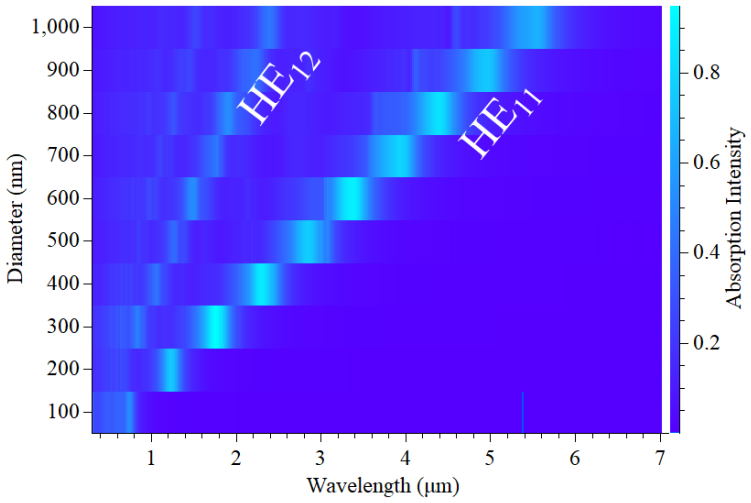

Figure 11. Absorption Plot Illustrating HE_{11} Intensities for InSb Nanowire Diameters.

HE_{11} and HE_{12} modes are labeled, showing the relationship between nanowire diameters and the wavelengths which fit the fundamental HE_{11} mode resonance.

The next set of simulations focused on the effects nanowire height might play on the absorption efficiencies. The goal of these simulations was to determine the minimum height, of the largest 1000 nm diameter nanowire, should be in order to maximize absorption efficiency. As shown in the previous two figures, a 1000 nm diameter InSb nanowire is expected to resonate according to the HE_{11} mode close to 6 µm wavelengths. With excessively long nanowires, higher energy wavelengths begin to absorb more efficiently at the secondary HE_{12} mode, and even the tertiary HE_{13} mode. If the increased absorbance from these modes is too great, the nanowires may lose the selectivity that is achieved by targeting the HE_{11} mode. If too short in length, a nanowire will show a decrease in absorption intensity, rendering it a suboptimal selective absorber. This can be seen in Figure 12.

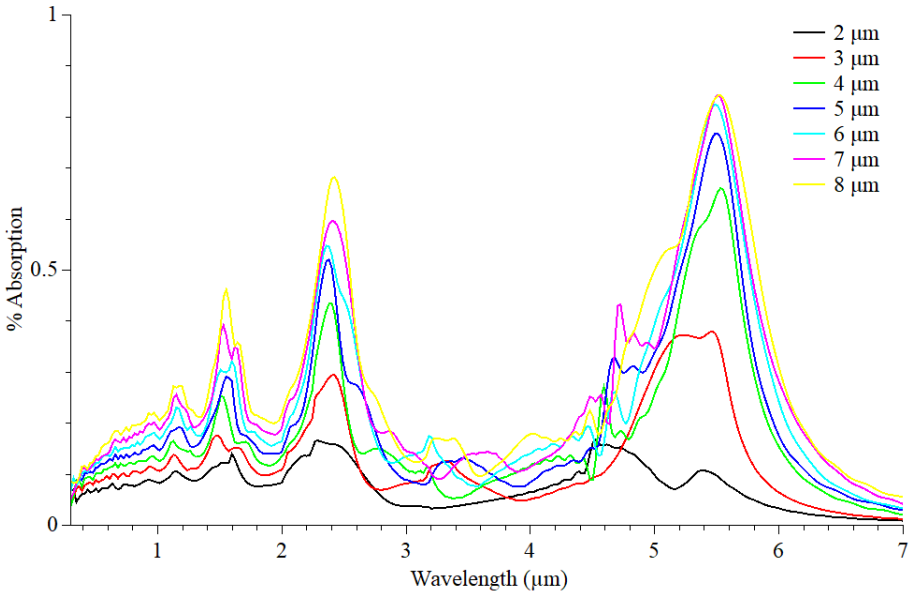

Figure 12. InSb Nanowire Height Effect on Absorption
A 1000 nm diameter InSb nanowire simulated with varying lengths. The maximum difference between the HE_{11} and HE_{12} modes was found to be at 6 µm tall

Fabrication Results

To dry etch vertical InSb nanowire arrays, a RIE process needed to be developed. This results sections will focus on this process development. High aspect ratio InSb structures are not commonly fabricated, and often relies on growth methods. In terms of dry etching InSb, a fair amount of research exists for microscale structures, such as mesas, however, since data pertaining to high aspect ratio or nanowire structures was lacking, a RIE process had to be further developed. RIE process performance was determined based on stoichiometric etch rates, smooth surface morphologies, and vertical side walls. Using profilometry, SEM, and EDS, this section will cover each step of the etch process development. All processes recipes tested are provided in Appendix 1 – Etch Processes.

InSb Dry Etch Process Development

The first tested InSb RIE processes were roughly based on previously reported $CH_4/H_2/Ar$ based recipes (Diniz et al., 1998; Zhang et al., 2009). Figure 13.1 shows the effects of changing CH_4 flow rates, and 13.2 shows those effects in terms of etch rate. The processes in Figure 13.1 suffered from a polymer deposition that covered both the sample and the sample carrier (shown in Figure 13.1(e)). Figure 13.2 suggests that CH_4 has a large role in etching rate. Addition of N_2 in a $CH_4/H_2/Ar$ process was used to inhibit the hydrocarbon polymer deposition which has been shown in prior research (R. C. Keller, Seelmann-Eggebert, & Richter, 1995). Figure 14.1 shows a variation of the Figure F1 processes with the addition of N_2. After etching, there were no longer visible signs of polymer deposition on samples with added N_2. Figure 14.2 again shows a correlation

between CH_4 flow rate and etch rate. Figure F14.1 (c) and (d) also show an increased etch rate with higher platen power. Trench depths were measured with surface profilometry.

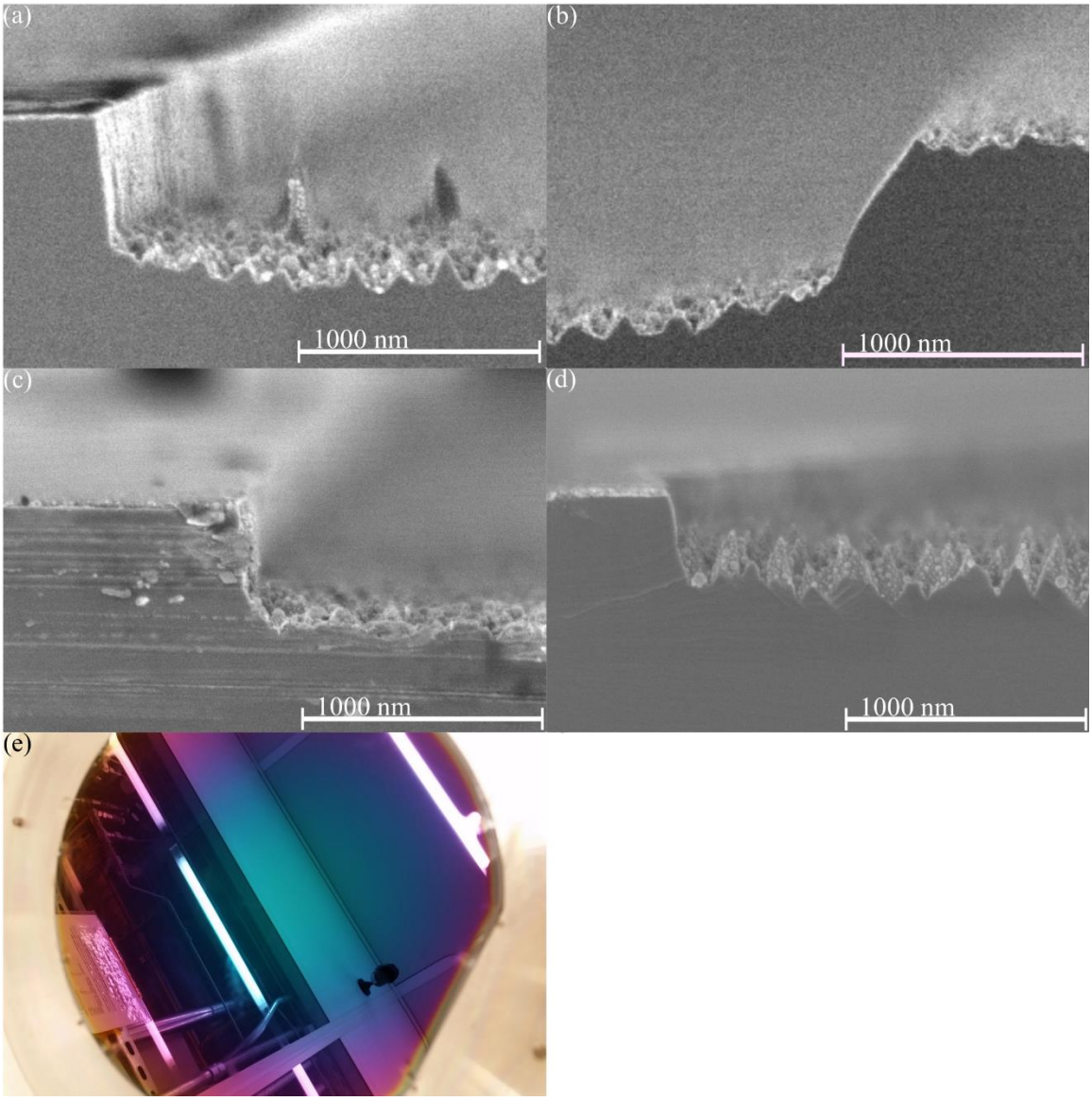

Figure 13.1. Effects of CH_4:H_2 Ratio and Etch Time on InSb Micro-Trench Etching. *(a) and (b) etch process varied only by time, 10 minutes and 30 minutes, respectively. (a) CH_4/H_2 flow of 15/50 sccm, (c) CH_4/H_2 flow of 10/50 sccm, and (d) CH_4/H_2 flow of 5/50 sccm. All other parameters were held constant with Ar flow of 5 sccm, 7 mTorr chamber pressure, 100 W platen power, 600 coil power, 20° C, and 10 min etch time. (e) Polymer deposition on sample carrier.*

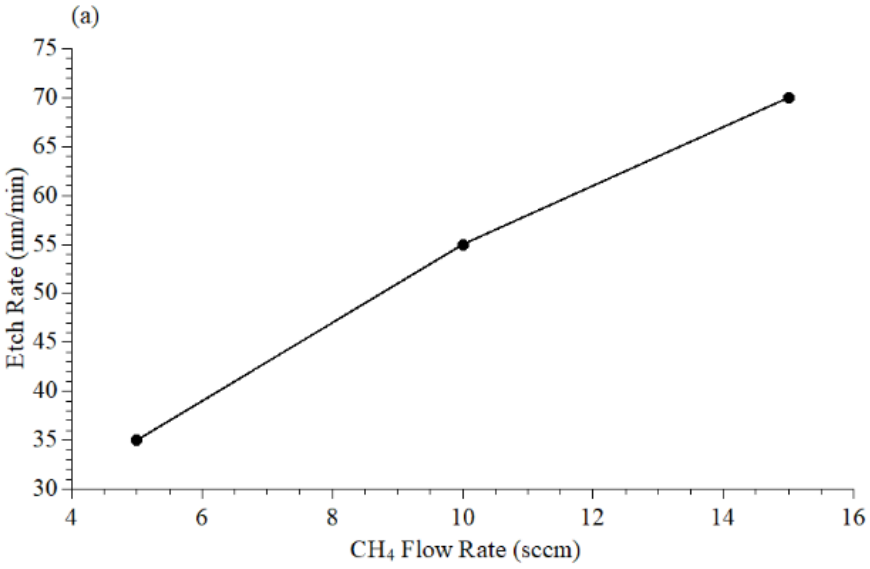

Figure 13.2. Effects of CH_4 Flow Rate on Etch Rate.
(a) Increased shows an etch rate with increasing CH_4 flow rate.

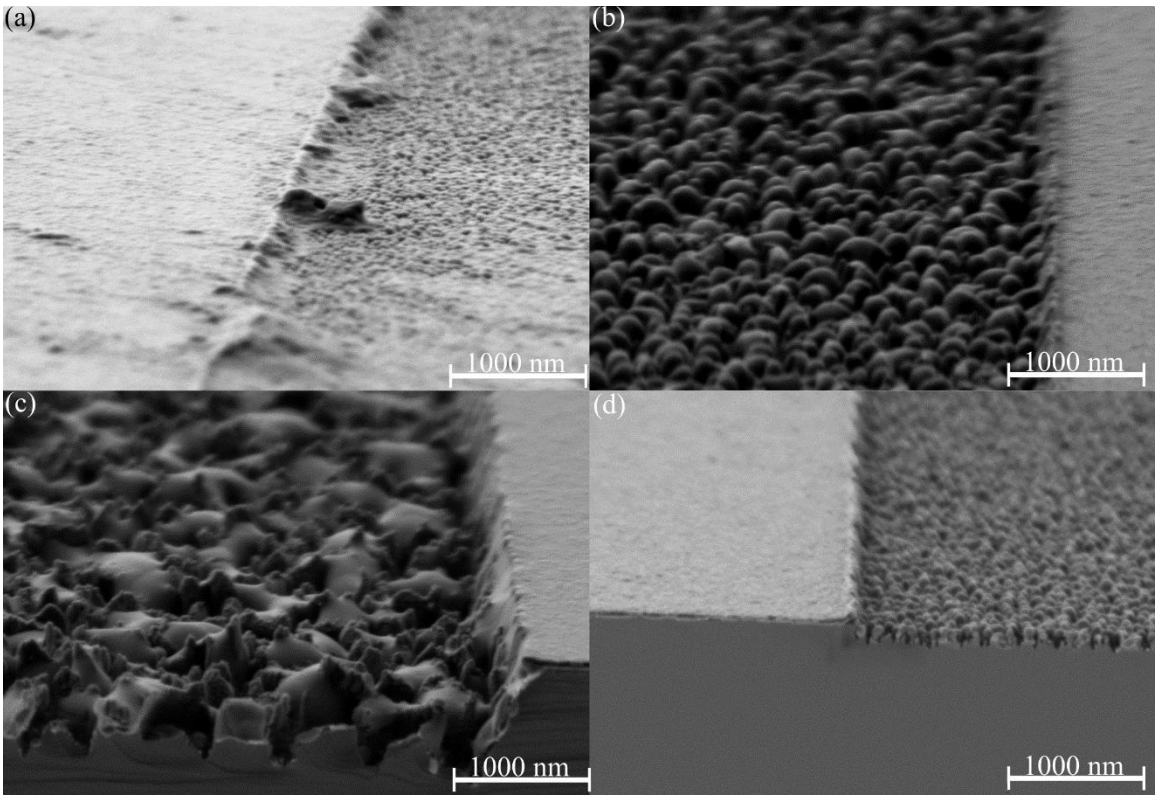

Figure 14.1. Effects of CH_4/H_2 Ratio with Added N_2 and Effect of Platen Power.
(a), (b), and (c) have varied CH_4/H_2 flow rates (sccm) of 10/50, 15/50, 25/50, respectively. (c) and (d) have varied platen power(W) of 20W and 100W, respectively. All

other process parameters were held constant with an Ar flow of 5 sccm, the N_2 flow of 5 sccm, a chamber pressure of 15 mTorr, platen power of 20 W (except for (d)), coil power of 800 W, the temperature of 20 C, and an etch time of 10 min.

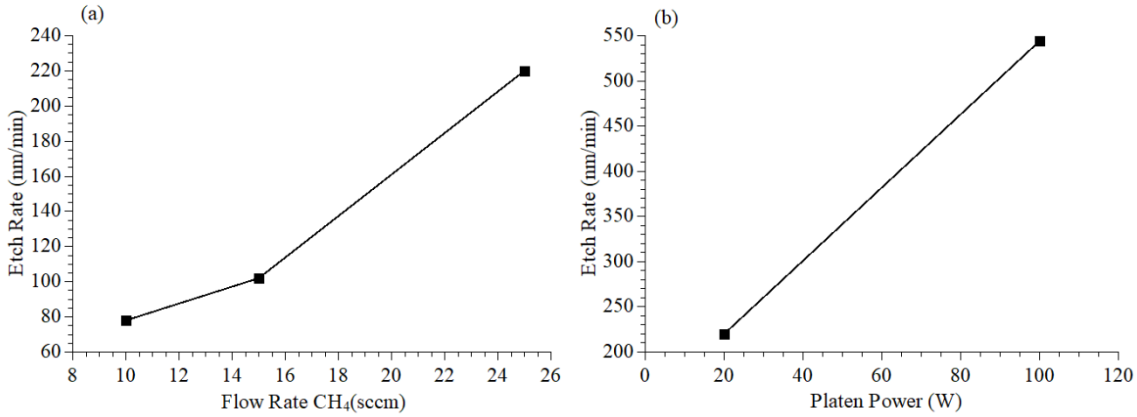

Figure 14.2. Effects of CH_4 Flow Rate and Platen Power on InSb Etch Rate.
(a) Changing etch rate corresponding to the increased CH_4 flow rate. (b) Shows an increased etch rate with increasing platen power.

With a basic understanding of the InSb etching behavior of this $CH_4/H_2/Ar$ process, it was applied to an array of micropillars with pitch and diameter of 2 µm. The effect temperature has on InSb etch was investigated as it has been reported to etch smoother surface morphologies (Pusino, Xie, Khalid, Thayne, & Cumming, 2016), and can also reduce or eliminate the deposition of hydrocarbon polymers. Figure 15 shows the effect of high chamber temperature. A higher etch rate and a smoother surface morphology (decreased micro-grass) were observed along with no visible signed of polymer deposition. Etch times were intended to be constant, however, Figure 15 (b) was an 8 minute etch opposed to 10 min due to a tool failure. Etch rates were calculated and are shown in Figure 15.2. While two data points is inadequate to conclude exactly how temperature etch rates of InSb, it provides some guidance in moving forward with the process development. The substantial difference in surface morphology was likely due to

better etch product desorption because of increasing volatility with increasing temperature.

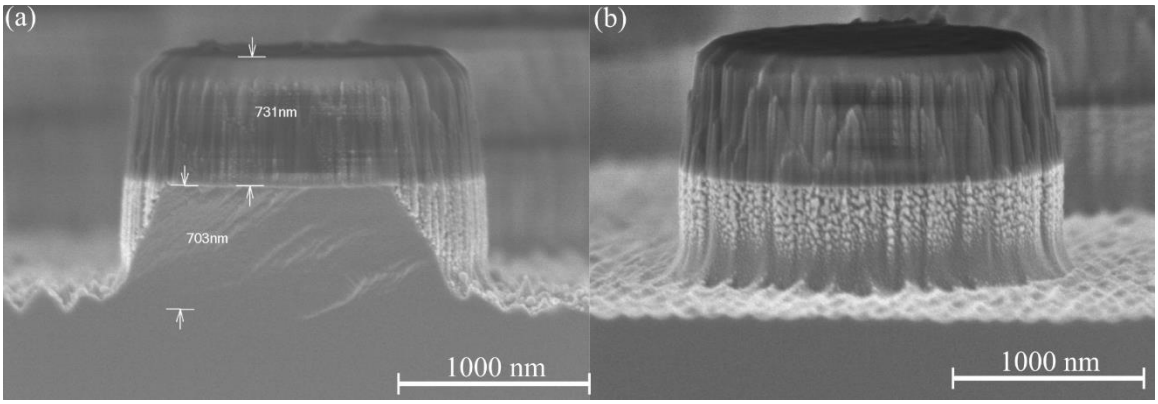

Figure 15.1. Effect of Temperature on InSb Micro Pillar Etching.
(a) was etched at 20° C for 10 minutes. (b) was etched at 130° C for 7.5 minutes. All other process parameters were held constant with a CH_4/H_2 flow rate of 15/50 sccm, Ar flow rate of 5 sccm, N_2 flow rate of 5 sccm, chamber pressure of 7 mTorr, platen power of 100 W, and coil power of 600 W.

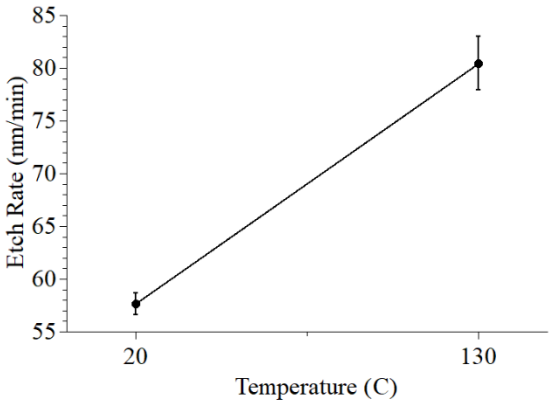

Figure 15.2. Effect of Temperature on InSb Etch Rate.
Increasing temperature from 20° C to 130° C showed an etch rate increase of 17 nm/minute.

A sweep of CH_4:H_2 ratios was conducted next by holding all etching parameters constant, including the total partial pressure of gases. With a total combined CH_4 and H_2 flow rate of 55 sccm, the CH_4:H_2 ratio was increased from 0.1 to 0.7. The results from this experiment are shown in Figure 16.1, and again in Figure 16.3 where the experiment was repeated with a longer chamber temperature stabilization period, along with a 5 minute chamber cleaning steps between each sample. Figures 16.2 and 16.4 show the effect of increasing CH_4 ratio has on the etch rate of InSb. Further, there appeared to be tapering when etched with smallest CH_4 flow rate, which became less severe with increased CH_4. However, with higher ratios of CH_4, there are faint signs of necking on sidewalls. These trends are consistent with Figure 16.3 as well

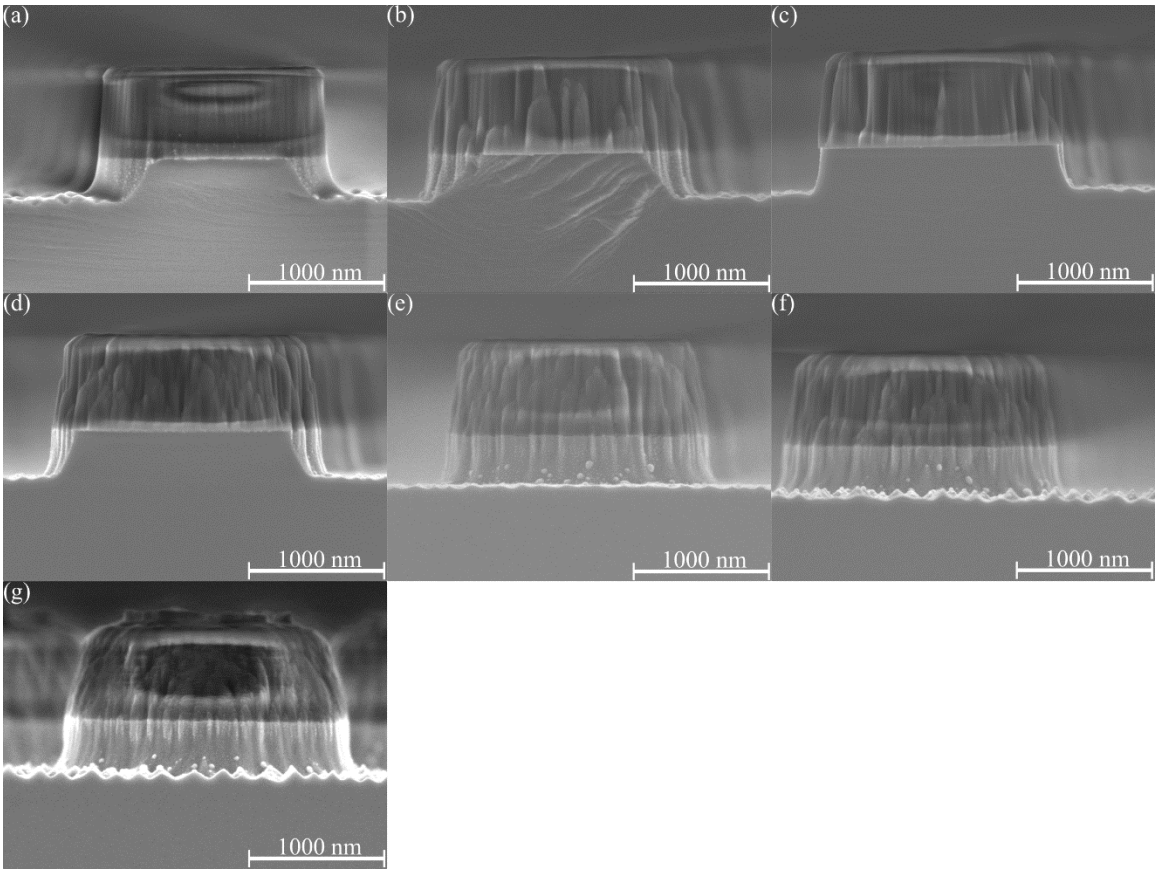

Figure 16.1. Effect of Increasing CH_4 Flow Rate on InSb Micro Pillar Etching.
The ratios of CH_4 increased as follows: (a) 0.1 (b) 0.2. (c) 0.3 (d) 0.4. (e) 0.5. (f) 0.6. (g) 0.7. A combined total of CH_4 and H_2 flow rates was held constant at 55 sccm. All other process parameters were held constant with a 5 sccm Ar, 10 mTorr chamber pressure, 100 W platen power, 800 W coil power, 130° C, and etched for 5 minutes.

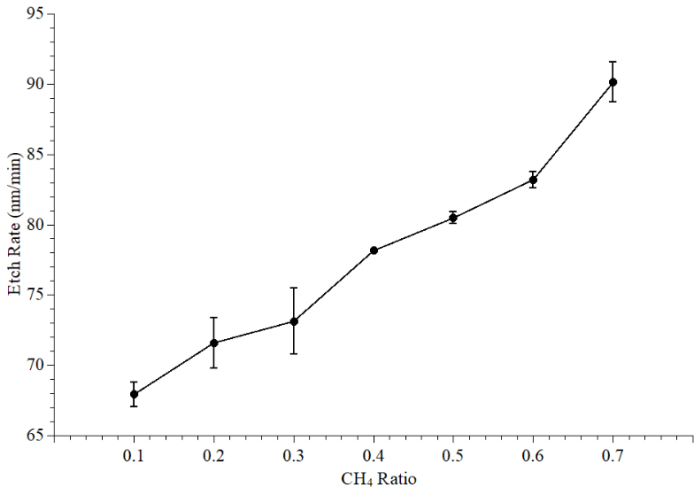

Figure 16.2. Etch Rate of InSb as a Function of CH_4 Ratio.
Increasing CH_4 ratio results in increased InSb etch rate.

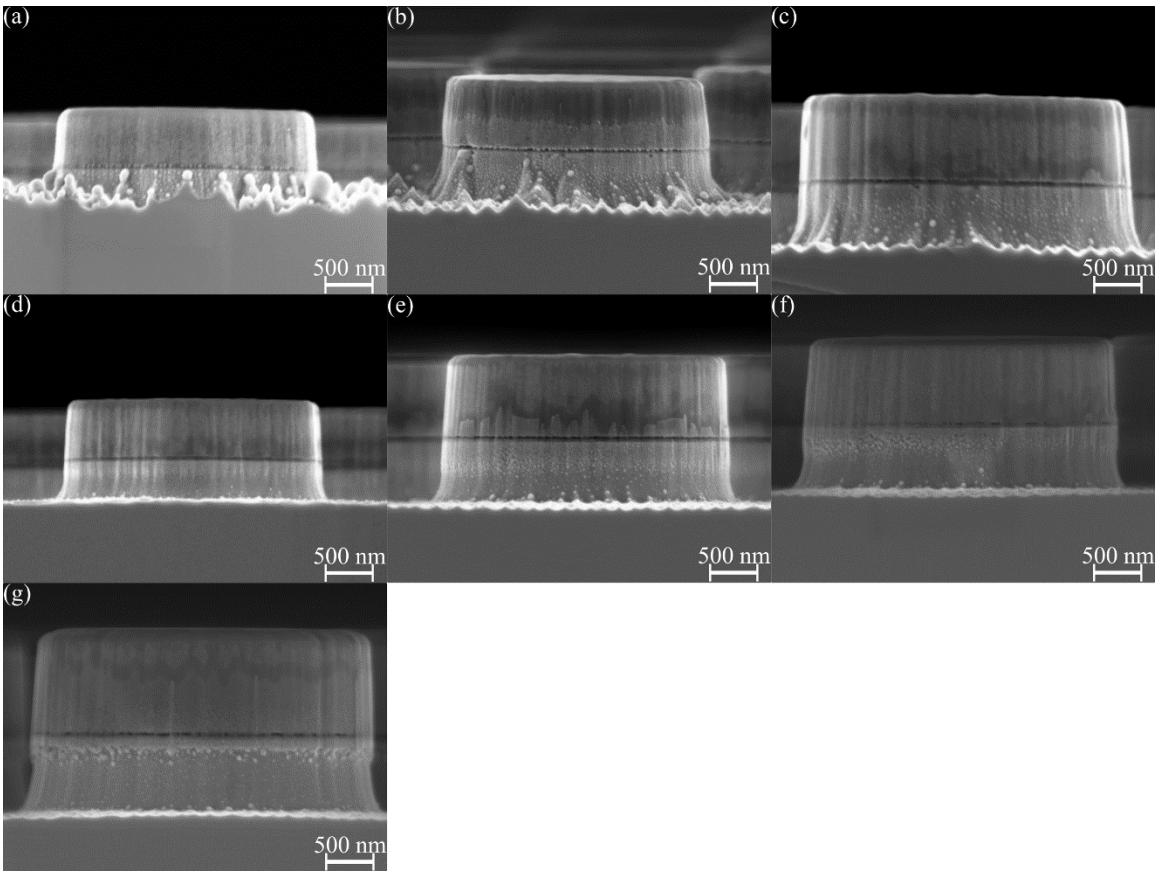

Figure 16.3. Effect of Increasing CH_4 flow rate on InSb Micro Pillar Etching.

Repeat test, same as Figure 16.1, but included a cleaning cycle in between each sample. The ratios of CH_4 increased as follows: (a) 0.1 (b) 0.2. (c) 0.3 (d) 0.4. (e) 0.5. (f) 0.6. (g) 0.7. A combined total of CH_4 and H_2 flow rates was held constant at 55 sccm. All other process parameters were held constant with a 5 sccm Ar, 10 mTorr chamber pressure, 100 W platen power, 800 W coil power, 130° C, and etched for 5 minutes.

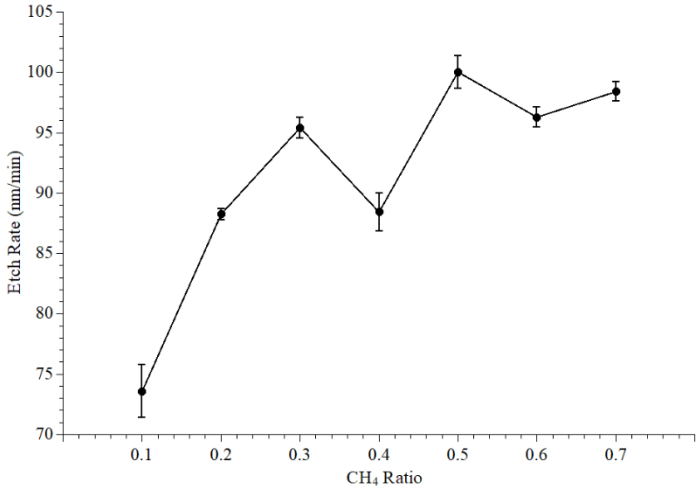

Figure 16.4. Etch Rate of InSb as a Function of CH_4 Ratio.
Although there is greater variation, the trend of increasing CH_4 ratio giving rise to greater InSb etch rate remains true.

Satisfied with the results, the process used to produce Figure 16 (d) was tested on the nanoscale using two nanowire arrays - one with a 200 nm diameter and 2 µm pitch, and a second with a 200 nm diameter and 500 nm pitch. Figure 17 shows the resulting etched InSb nanowire arrays. Two critical observations can be made from these images. First, a significant taper at the base. Second, there are signs of undesired re-deposition in surface morphology and nanowire diameter. Shown in Figure 17 (c), the taper is an obvious issue if attempting to etch nanowire arrays with small pitches, as the tapered bases connect with their adjacent nanowires.

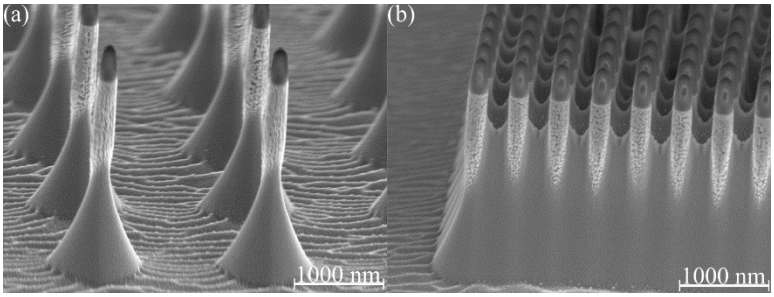

Figure 17. Dry Etched InSb Nanowires.
(a) 200 nm diameter 2 µm pitch nanowire array. (b) 200 nm diameter 500 nm pitch nanowire array. (a) and (b) were etched simultaneously, under the following conditions: 0.4 CH_4:H_2 ratio, 5 sccm Ar, 100 W platen power, 800 W coil power, 130° C, and a 45 minute etch time.

To address the tapering, the effects of increasing platen power and Ar flow rate were tested. It is expected that an increase in platen power will achieve more vertical sidewalls, greater anisotropy, due to the increased directionality of ions, and stronger physical etching effects. Similarly, an increased Ar flow rate was expected to provide more ions contributing to ion bombardment relative to the chemical etchants, further favoring an anisotropic etch profile. Figure 18.1 shows the effect of increasing platen power (a, b, and c) and of an increase of Ar flow (d). Together, these results suggest that increasing the platen power or the Ar flow can control etch rate (Figure 18.2 (a) and (b)) and sidewall profile (Figure 18.2 (c) and (d)). Again, while these limited data sets are not conclusive, they were used as guidance for further process development.

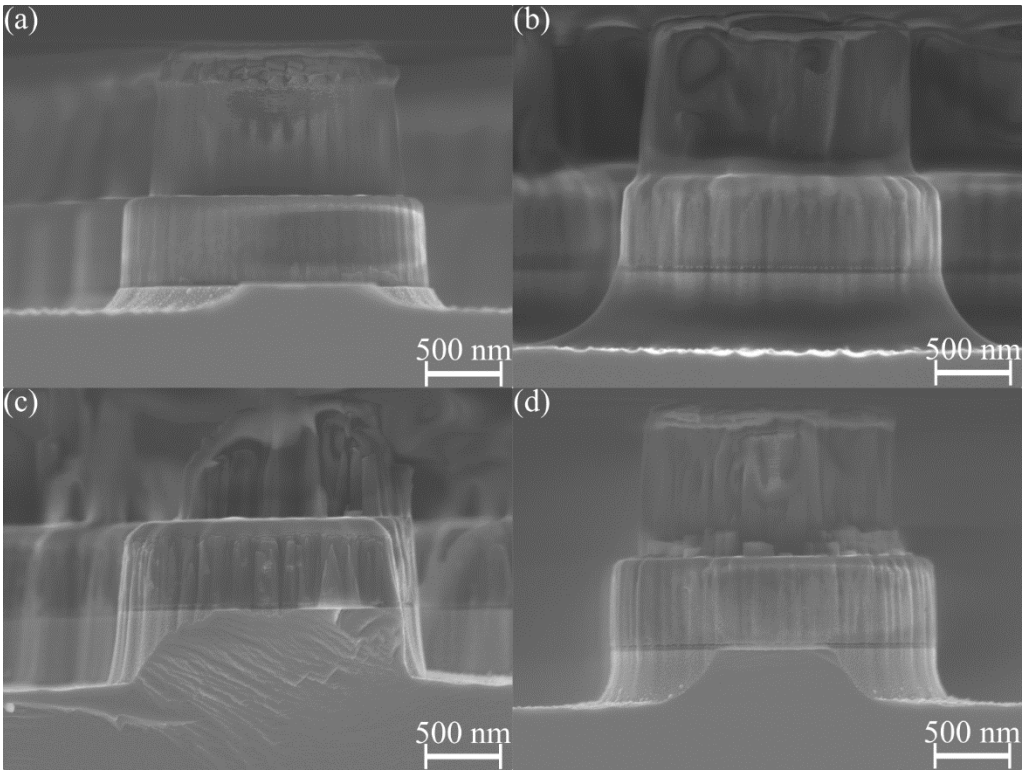

Figure 18.1. Effect of Increased Platen Power and Ar Flow on Miro Pillar Etch Profile. *(a) Platen power of 100 W and Ar flow rate of 5 sccm. (b) Platen power of 200 W and Ar flow rate of 5 sccm. (c) Platen power of 275 W and Ar flow rate of 5 sccm. (d) Platen power of 100 W and Ar flow rate of 15 sccm. All other process parameters were held constant with a 0.4 CH4:H2 ratio, 10 mTorr chamber pressure, 800 W coil power, 130° C, and a 5 min etch time.*

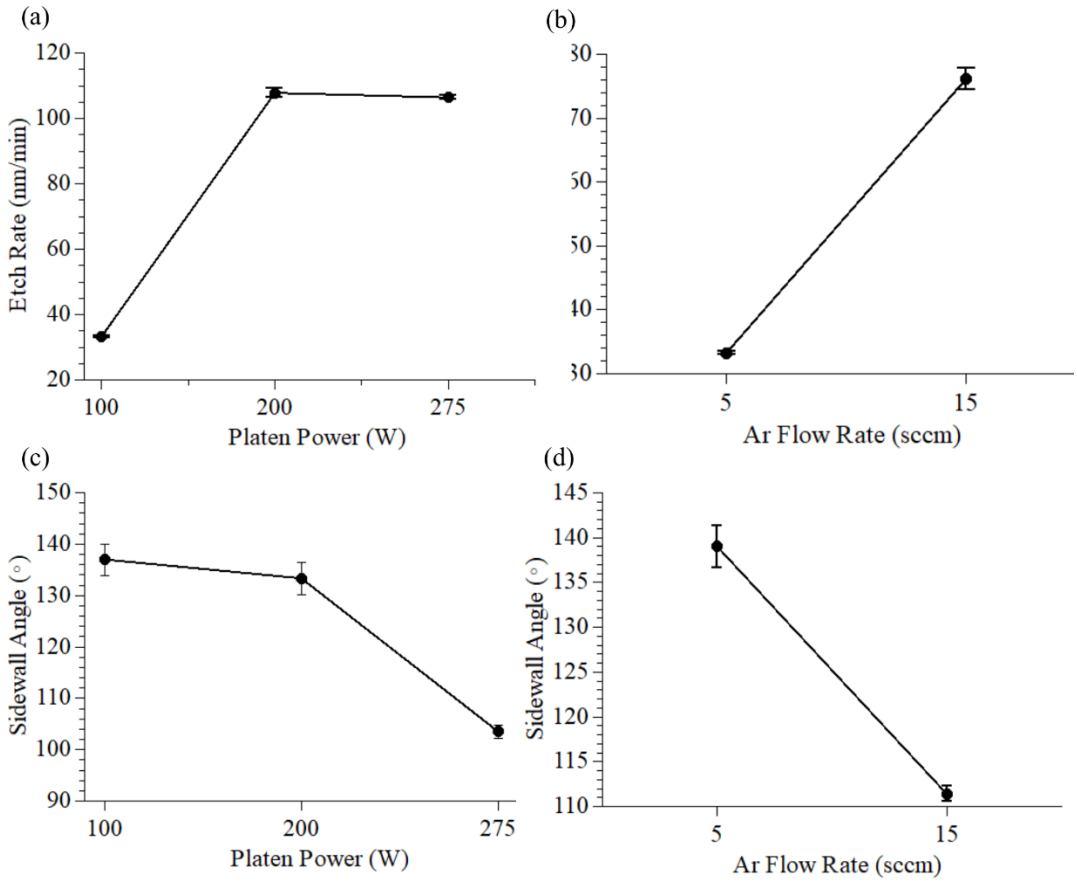

Figure 18.2. InSb Etch Rate and Sidewall Angle Relative to Platen Power and Ar Flow Rate

(a) Effect of increasing platen power on etch rate. (b) Effect of increased Ar flow on etch rate. (c) Effect of platen power on sidewall angle. (d) Effect of Ar flow rate on sidewall angle. All other process parameters were held constant with a 0.4 CH_4:H_2 ratio, 10 mTorr chamber pressure, 800 W coil power, 130° C, and a 5 min etch time.

The etch process used in Figure 18.1 (c) was deemed best and was used to etch samples for 30 minutes rather than 5. As shown in Figure 19 (a) the tapered base remains. One consideration causing this is that etch products may not have been desorbing efficiently, inhibiting chemical etching with increasing etch times. Figure 19 (b) was etched with a chamber temperature of 160° C to increase the volatility of etch products and facilitate desorption. An increase in Ar flow along with the higher temperature is shown in Figure 19 (c) to further influence an anisotropic etch profile. Etch rate decreased slightly from

104 nm/min to 92 nm/min when the temperature was raised from 130° C to 160° C, and an increased slightly from 92 nm/min to 103 nm/min when Ar flow was raised from 5 sccm to 15 sccm. Tapering was largely unaffected by the temperature increase. A slight variation in sidewall profile seen in 19 (c) is likely due to an increased Si etch rate, causing the more mask erosion, rather than a variation in the InSb etching behavior.

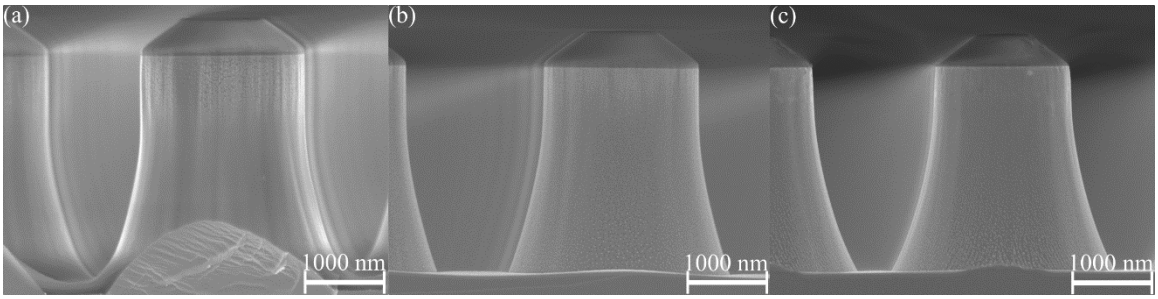

Figure 19. Effects of Increased Etching Temperature and Ar Flow.
(a) etched at 130° C with 5 sccm Ar. (b) etched at 160° C and 5 sccm Ar. (c) etched at 160° C, and 15 sccm Ar. All other process parameters were held constant with a 0.4 CH_4:H_2 ratio, 10 mTorr chamber pressure, 275 W platen power, 800 W coil power, and a 30 minute etch time.

The next attempt to correct the tapered etch profile looked again at the increasing CH_4 ratio, but at a higher chamber pressure. It was expected that increasing the chamber pressure would facilitate greater isotropic etching due to a smaller means free path. Figure 20.1 shows increasing CH_4 ratios in a chamber pressure of 30 mTorr. The results follow several trends. First, increasing the ratio of CH_4 showed an increase etch rate, but as CH_4 and H_2 came close to equal parts, shown in Figure 20.1 (i), the etch rate showed less change (shown in Figure 20.2), either plateauing of slightly decreasing. Second, a tapered sidewall will develop with too little CH_4, and sidewall necking seems to occur with too much CH_4. Lastly, there was evidence of some re-deposition seen on the surface,

and it seemed most substantial on the samples with the high CH_4. The process used in Figure 20.1 (c) yielded the most desirable results.

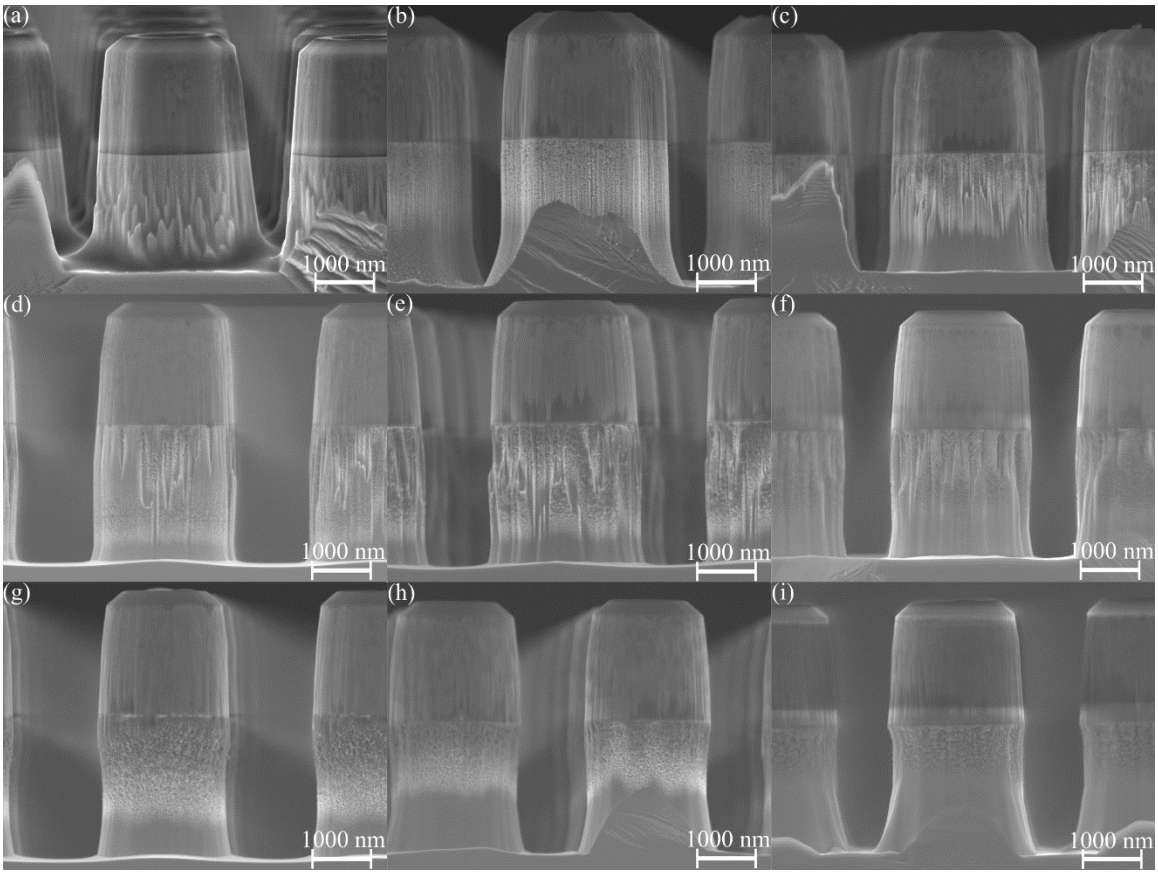

Figure 20.1. Effects of Increasing CH_4 with a 30 mTorr Chamber Pressure.
The ratios of CH_4 increased as follows: (a) 0.1 (b) 0.2. (c) 0.3 (d) 0.4. (e) 0.5. (f) 0.6. (g) 0.7. (h) 0.8. (i) 0.9. A combined total of CH_4 and H_2 flow rates was held constant at 55 sccm. All other process parameters were held constant with 5 sccm Ar, 30 mTorr chamber pressure, 200 W platen power, 800 W coil power, 160° C, and a 20 minute etch time.

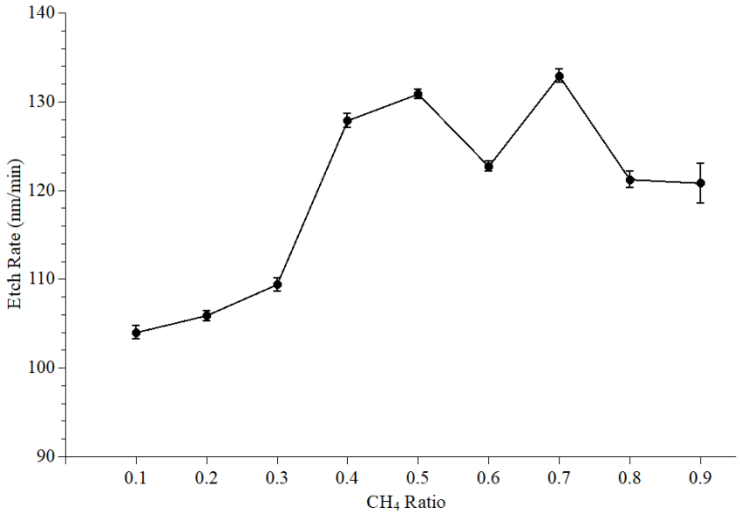

Figure 20.2. InSb Etch Rate with Increasing CH_4 Ratio at 30 mTorr.
Increasing InSb etch rates with higher CH_4 ratios with a chamber pressure of 30 mTorr.

The processes from Figure 20.1(b), (c), and (d) were then used to etch samples of 200 nm diameter and 2 µm pitch. Etch times were varied to target 4 µm tall InSb nanowires. These results are shown in Figure 21. All three samples have a re-deposited material which significantly increased the intended diameter - approximately by a factor of 2.5. During etching, the re-deposited material seemed to have covered the Si mask and effectively increased the mask diameter as etching continued.

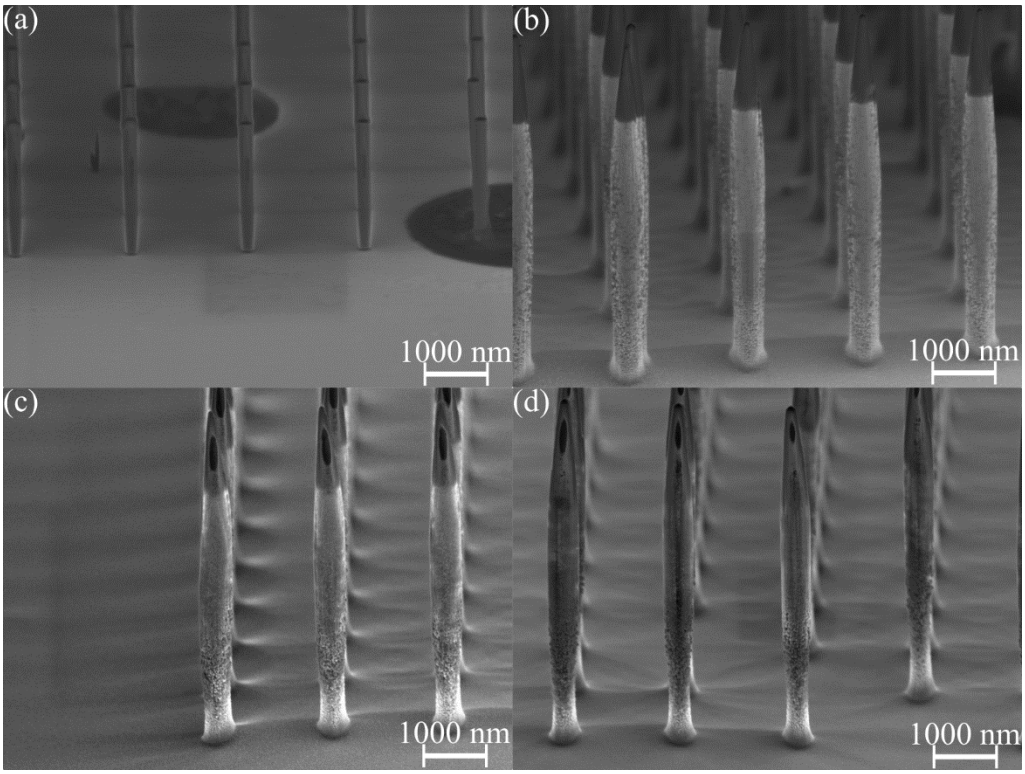

Figure 21. InSb Nanowires Etched with Varied CH_4 Ratio.
(a) Unetched InSb sample with only Si mask with a 200 nm diameter. Samples were etched as follows: (b) CH_4 ratio 0.2 for 37 minutes. (c) CH_4 ratio 0.3 for 35 minutes. (d) CH_4 ratio 0.4 for 32 minutes. All other process parameters were held constant with an Ar flow rate of 5 sccm, 30 mTorr chamber pressure, 200 W platen power, 800 W coil power, and 160° C.

Figure 22 shows the result of increased Ar flow on samples with 100 nm mask diameter. The resulting diameter increase was reduced from a factor of 4.2 to a factor of 3.5. Figure 22 also verifies that the re-deposition increases the mask diameter very early on – in this case by a factor of 2.0 after only 5 minutes of etching. This was an important distinction as it suggests that increased diameter is due to increasing mask diameter, due to the re-deposited, rather than the added thickness coming only from re-deposition. The re-deposited layer may be small enough to retain the desired optical properties. Two key observations can be made from Figures 21 and 22. First, Ar seems to mitigate the re-

deposition to some degree. This effect aligns with prior research on the effects of Ar in dry etching Indium based III-V materials as greater desorption of indium based etch products may occur due to better molecular dissociation caused by Ar ion bombardment (Abautret et al., 2015). Second, the issue seems to be less severe as the mask diameter increases. Assuming the thickness of the layer of re-deposition remains similar with all diameters, the ratio of re-deposition thickness to nanowire diameter would decrease. While this severely limits the smallest diameters that can be etched, it was likely to become less of an issue with larger diameter nanowires. Despite this, the composition of the re-deposition was studied with hopes of better addressing the problem.

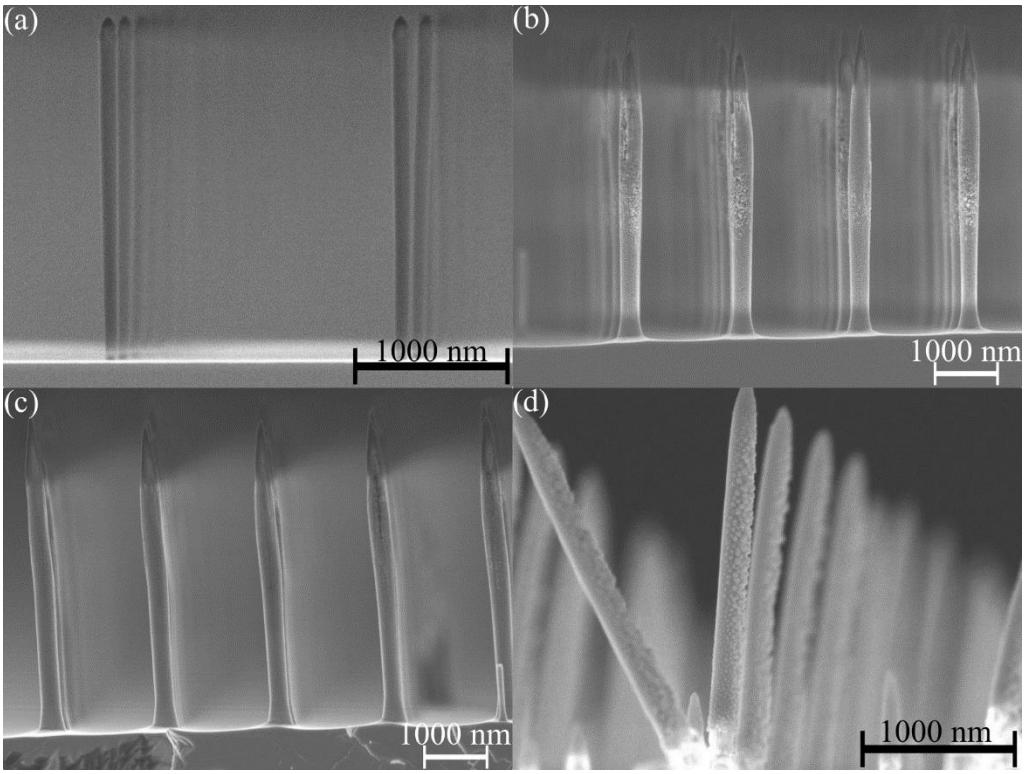

Figure 22. Effects of Increasing Ar on InSb Etching Re-Deposition.
(a)An unetched 100 nm diameter Si mask. (b) Ar flow rate of 20 sccm for 35 minutes. (c) Ar flow rate of 40 sccm for 35 minutes. (d) Ar flow rate of 40 sccm for 5 minutes. All

other process parameters were held constant with a CH_4 ratio 0.3, 30 mTorr chamber pressure, 200 W platen power, 800 W coil power, and 160° C.

EDS was used to determine the composition of the re-deposited material. It can be seen in Figure 23 that both indium and antimony are being re-deposited during etching, however indium is at a higher rate. This is particularly true toward the upper part of the nanowires.

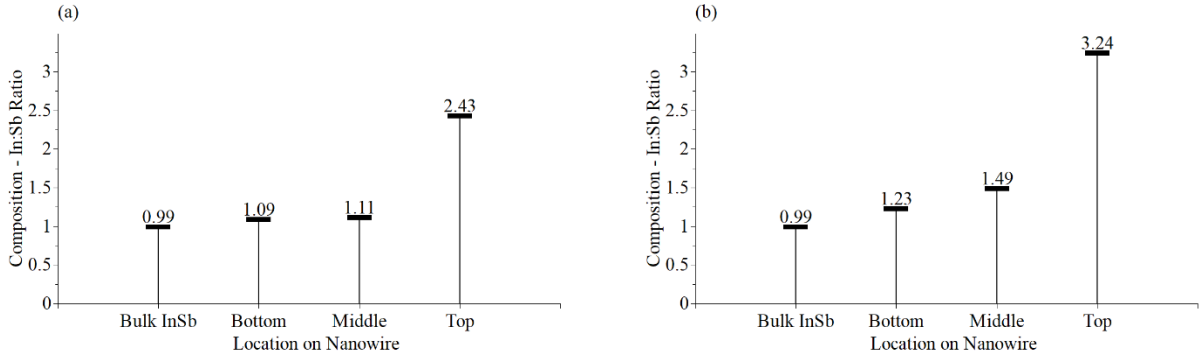

Figure 23. EDS Analysis of InSb Nanowires Etched with a $CH_4/H_2/Ar$ Process. *Samples (a) and (b) were etched with the same $CH_4/H_2/Ar$ process. A value of 1 is equal parts In:Sb. Over 1 corresponds to increasing indium composition, and under 1 is decreasing. Both samples show the re-deposition contains higher levels of indium toward the top of the nanowires.*

Three options were used to address the re-deposition. One option was to remove the material with a post -processing step. The second option was to change the dry etching process either by fine tuning the existing parameters, or altering the etching chemistry. The last option was to work around the re-deposition by either etching shorter nanowires to minimize the impact of re-deposition and work primarily with larger diameters of 300 nm and above, which would be less affected.

The first, post -processing option, was attempted with wet and dry etching. Wet etching in hydrochloric acid (HCl) and nitric acid (HNO_3) was performed but we soon realized the process lacked the required In/Sb etch selectivity. Etching the appropriate proportions of indium and antimony simultaneously proved difficult, and the non-uniform distribution of re-deposition limited the effectiveness even further. A dry etching post processes that targeted indium more than antimony seemed more desirable. Processes with high amounts of CH_4 and Cl_2 were used to disproportionately target indium, however, after several experiments, it was apparent that removing the re-deposition and not compromise the InSb nanowire was unlikely. This data was excluded from this thesis.

The second option to address the re-deposition was to change the dry etching process and required further investigation into the cause. Literature focused on the dry etching of indium based III-V compounds pointed to several potential factors contributing to re-deposition during a $CH_4/H_2/Ar$ process. Of them, physical sputtering of both elements (Fouad, 2014), more efficient desorption of the group V element - (antimony) (Diniz, Swart, Jung, Hong, & Pearton, 1998), and thermal decomposition of the etch product trimethylindium ($In(CH_3)_3$) (McDaniel & Allendorf, 2000), were likely contributors. Minimizing sputtering would require a decreased Ar flow rate and/or a decrease in platen power. Previous figures have shown how both Ar and platen power will affect the etch rate and etch profile of InSb micro and nanostructures. It was also shown that an increase of Ar flow rate can mitigate the effects of re-deposition. Figure 24 revisits these effects more closely on 100 nm diameter samples. Ar does not contribute much to the etch rate, while the platen power does. Further, a low platen power has a

strong decrease of isotropic etching, but the etch profile changes minimally as it increases beyond 100 W. Interestingly, if this is compared to Figure 22 (c), where Ar mitigated re-deposition, it seems reasonable to suggest that the role Ar plays in InSb etching is more in the desorption of etch products rather than physically etching itself. The diameters remained thinnest in Figure 24 (d) and (e), however (d) did exhibit greater isotropic etching, leaving the surface morphology much rougher. Taken together, the results supported limiting the platen power to the lowest effective wattage, as to minimize potential sputtering, and a high Ar flow to facilitate etch product desorption.

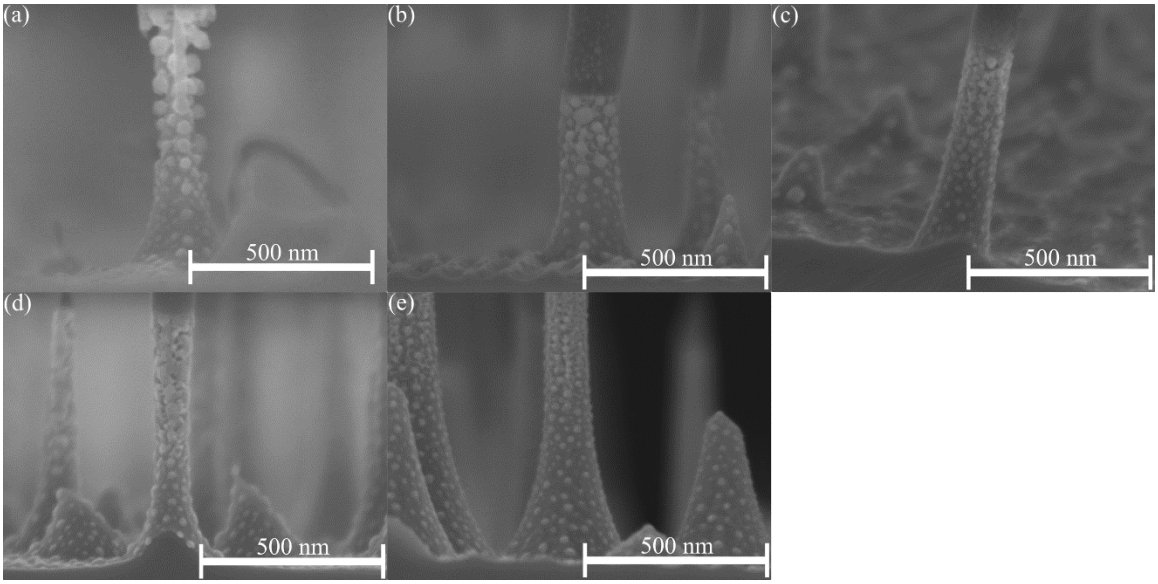

Figure 24.1. Platen Power and Ar Flow Rate Effect on InSb Nanowire Etch Behavior. *(a) 5 sccm Ar and 50 W platen power. (b) 5 sccm Ar and 100 W platen power. (c) 5 sccm Ar and 200 W platen power. (d) 40 sccm Ar and 50 W platen power. (e) 40 sccm Ar and 100 W platen power. All other process parameters were held constant with a CH_4 ratio 0.3, 10 mTorr chamber pressure, 800 W coil power, and 160° C. The small structures beside the nanowires in these samples were due to inadequate removal of masking materials, which left small, random micro masks around the samples.*

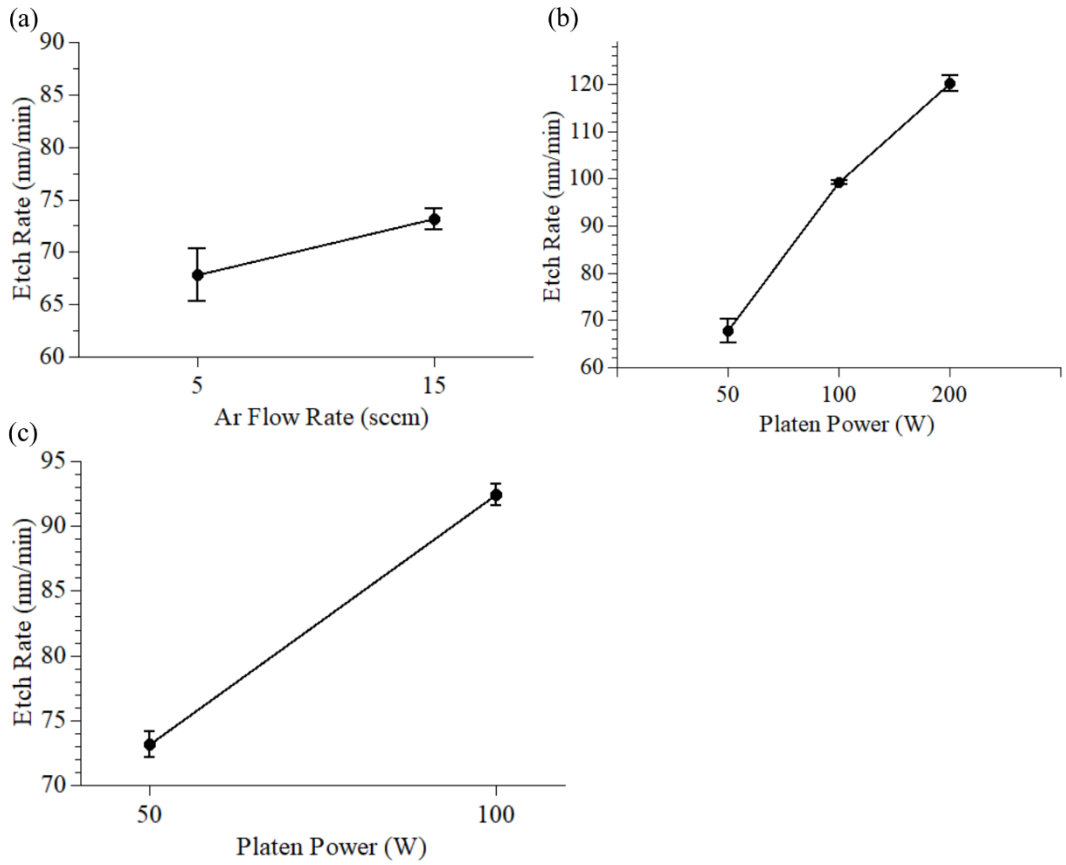

Figure 24.2. Effects of Ar Flow Rate and Platen Power on InSb Nanowire Etch Rate. *(a) Ar flow rate increase as platen power remained at 50 W. (b) Platen power increase with a constant 5 sccm Ar flow rate. (c) Platen power increase with a constant 40 sccm Ar flow rate.*

Despite the improvements, some re-deposition remained, but as stated previously the effects would become much less an issue when etching larger diameter nanowires. The results from the process in Figure 24 (e) were deemed most suitable despite having a slight taper. This process, while not perfect, was used to etch larger diameters and with minimized etch times to fabricate nanowire arrays that would be minimally affected by re-deposition. The results of the etching these samples, which would later be used for measuring spectral reflection, can be seen in Figure 25. The process yielded substantially tapered structures, which will affect the way they absorb light. This will be discussed in

the Analysis section. Also interesting is the varied etch profile is seen in 200 (a), 300 (b), 500 (d), 700 (f), and 900 (h) nm samples, compared to the others. These samples were etched the day after the others, during which the ICP-RIE system was serviced. This led to increased etch rates, which seemed to increase re-deposition and decrease taper. This will be reviewed in the next chapter.

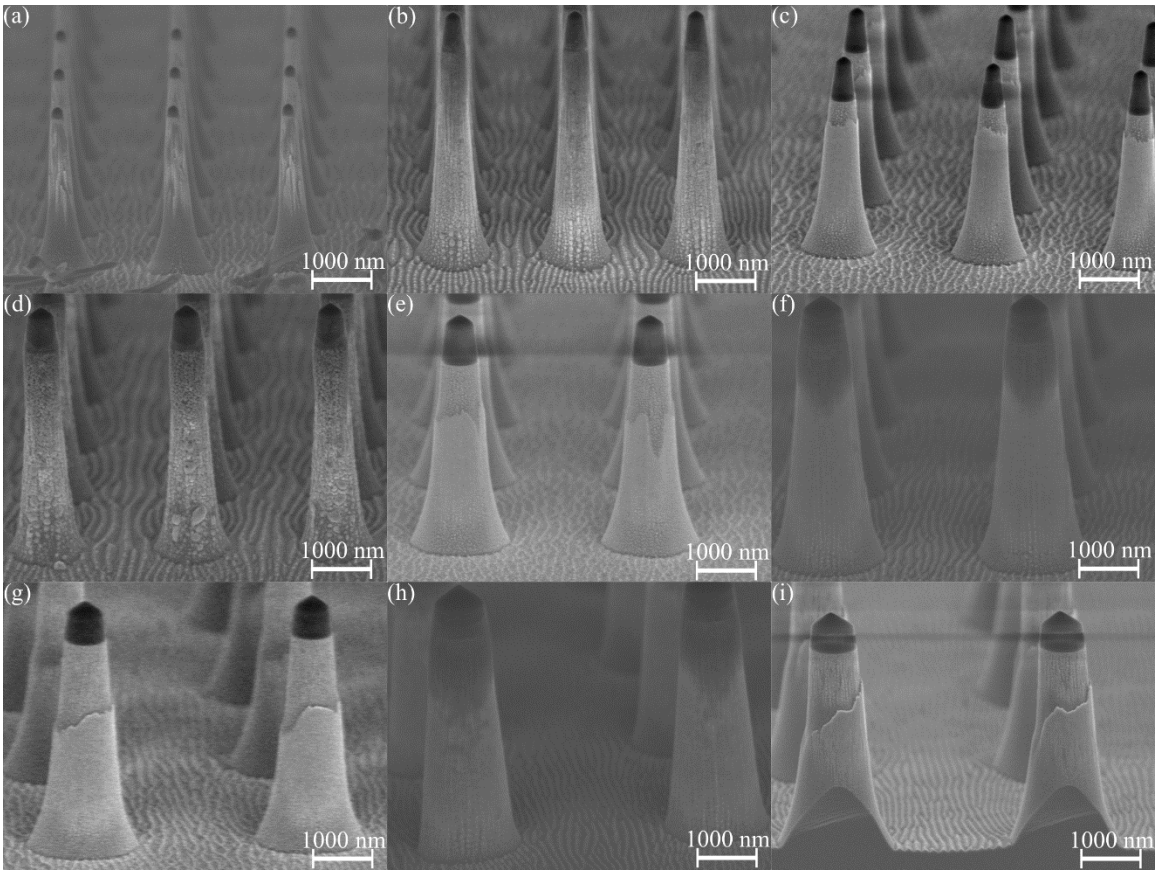

Figure 25. InSb Nanowires with Intended Diameters from 200 nm to 1000 nm.
A range of etched nanowire arrays that were used for spectral analysis. The mask diameters were as follows: (a) 200 nm, (b) 300 nm, (c) 400 nm, (d) 500 nm, (e) 600 nm, (f) 700 nm, (g) 800 nm, (h) 900 nm, (i) 1000 nm.

Because of the persistent re-deposition and tapering with the $CH_4/H_2/Ar$ process, alternate etching chemistries were also studied. From the development highlighted above,

it was established that indium is being re-deposited at a greater rate than antimony, and that it may be from a preferential loss of antimony, physical sputtering, thermal decomposition of the $In(CH_3)_3$ etch product or any combination of these. Regardless, removal of indium was central to the issue, so replacing or supplementing CH_4 as the sole indium etchant was of interest. CH_4, Cl_2, BCl_3, and HBr were available for etching InSb in the RIE system that was used. The next chapter will discuss the etching mechanisms for these gases and how the etch products affect the etch results. Initial testing made apparent that Cl_2, BCl_3, and HBr, processes yielded little if any visible re-deposition (results not shown for Cl_2 and BCl_3 test processes). However, large tapers persisted with these gas chemistries, even with changing parameters to obtain a more anisotropic etch. Because of this, HBr was added to the $CH_4/H_2/Ar$ process to test if a balance between etch profile and re-deposition could be achieved. HBr was selected over the chlorine - based gases due to the $InBr_3$ etch product being more volatile than $InCl_3$ (Pearton et al., 1992). Additional details on this selection will be covered in the next chapter. InSb was etched with 5 sccm and 2 sccm added HBr to the established $CH_4/H_2/Ar$ process. This resulted in a substantially less tapering, and minimal re-deposition, but did suffer from very rough surface morphology. The structures were analyzed with EDS, which verified that the added HBr effectively removes the re-deposition issue. SEM images of these two processes are shown in Figure 26.1 The respective EDS analysis can be found in Figure 26.2, which includes a comparison with the established $CH_4/H_2/Ar$ process. The addition of HBr yields promising results, and future research will attempt to optimize the HBr/ $CH_4/H_2/Ar$ process to etch InSb nanowires.

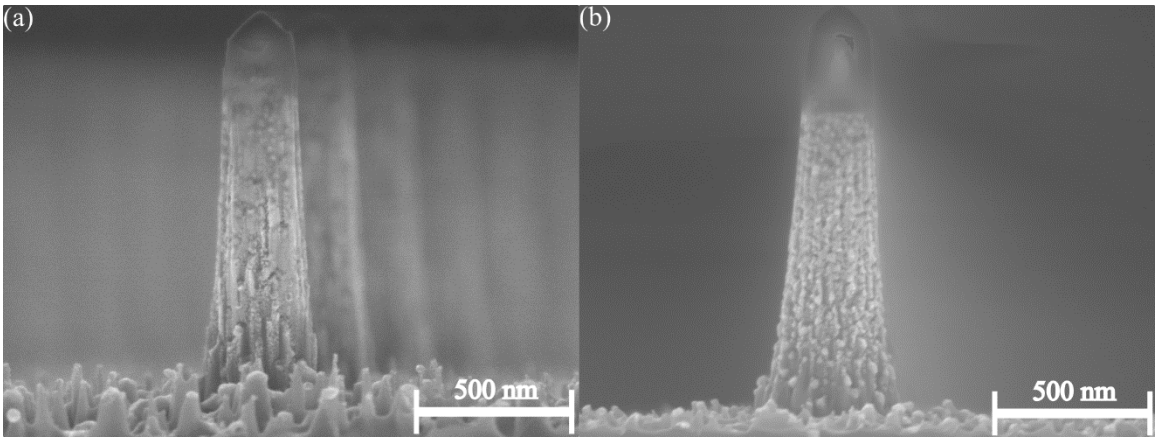

Figure 26.1. HBr Addition to $CH_4/H_2/Ar$ Etch Process with EDS Analysis.
(a) Addition of 5 sccm HBr to the $CH_4/H_2/Ar$ process. (b) Addition of 2 sccm HBr to the $CH_4/H_2/Ar$ process.

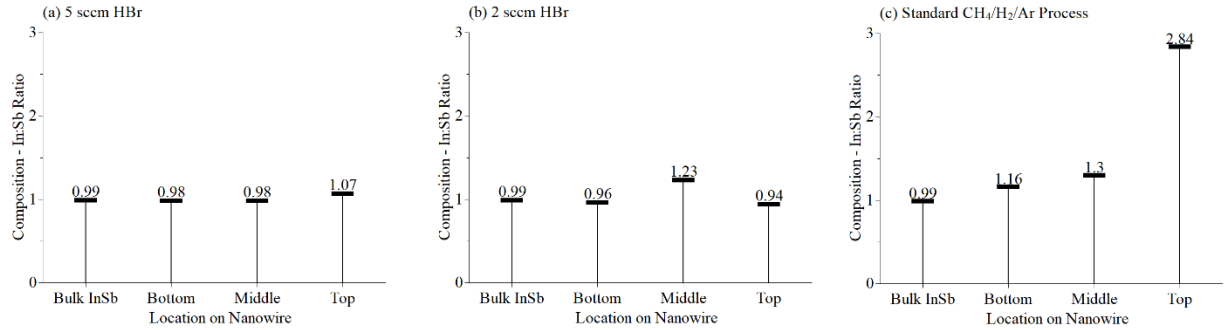

Figure 26.2. EDS Analysis of InSb Etched with HBr Added to the $CH_4/H_2/Ar$ Process.
EDS analysis showing the InSb ratio on different regions of the nanowires. A value of 1 means equal parts indium and antimony. Above 1, means greater indium composition, and below 1 means less indium relative to antimony. (a) EDS on 5 sccm HBr sample. (b) EDS on 2 sccm HBr sample. (c) EDS analysis showing the average surface composition without HBr added to the process.

Spectral Analysis

To determine if the fabricated InSb nanowires behave similarly to the results yielded from simulations, an FT-IR microscope was employed to measure specular reflection. As it was discussed in the fabrication section, due to some re-deposition and tapering, the RIE process resulted in structures that significantly varied from the ideal

nanowire arrays that were used in the simulations. The potential effects of these variations will be discussed in the next chapter.

Specular Reflection

Specular reflection was measured on the samples shown in Figure 25. These samples are labeled according to their intended diameters (i.e. the diameter of their mask prior to etching). A baseline reference measurement was made using a gold patch on the microscope stage prior to measuring each sample. Specular reflection was measured with a wavelength range of 2.5 μm to 7 μm. Figure 27 shows that the reflectance spectra of InSb nanowires shift with geometric changes. Some inconsistencies were introduced due to fabrication issues. As explained in Figure 25, some samples experienced an unintentional increased etched rate, which increased re-deposition and led to slightly larger diameters. This caused some samples, for example, the 900 nm and 1000 nm diameter samples, to have very similar geometries, with almost identical top diameters. The measured reflectance agrees with this as the curves follow each other closely. Table 1 shows the dimensions of the etched structures. Additional issues rooted in suboptimal nanowire dimensions caused measured reflectance results to vary from what was expected based on simulated data. These variations will be addressed in the next chapter.

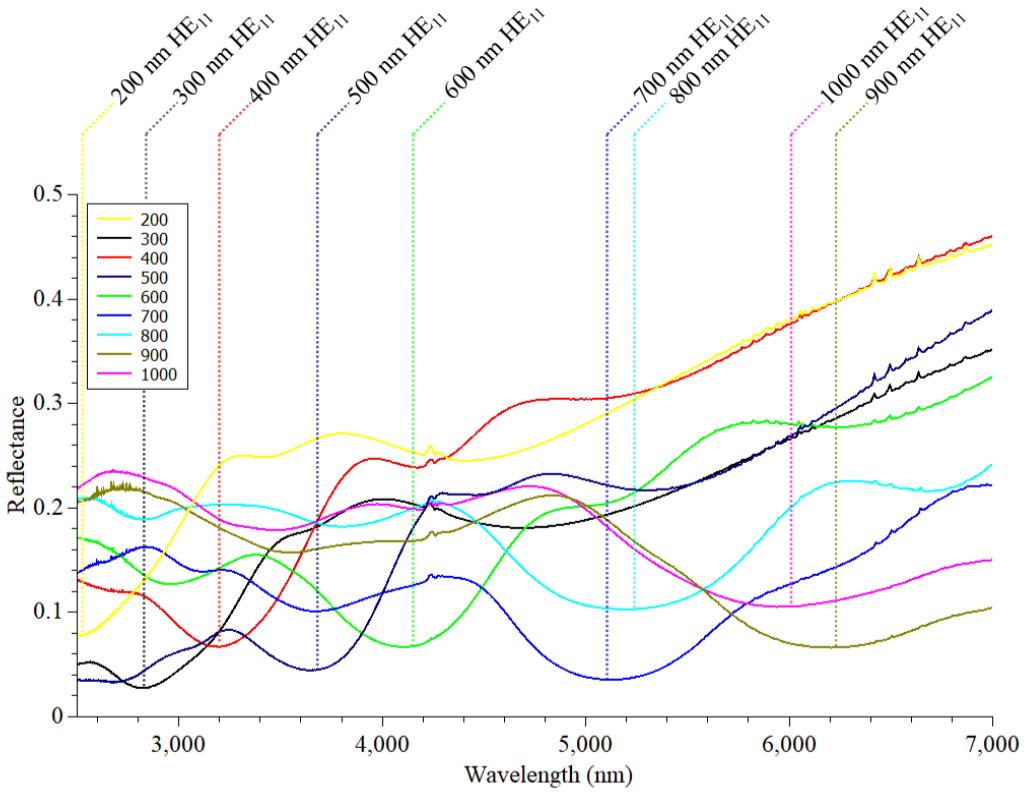

Figure 27. Spectral Reflectance Shifts with InSb Nanowire Array Geometry. *Specular reflection of on InSb samples with intended diameters of 200, 300, 400, 500, 600, 700, 800, 900, and 1000 nm. Dotted lines indicate the reflectance dip that is likely corresponding to resonance of the HE_{11} mode for each diameter.*

To gain a deeper understanding of the InSb nanowire interaction with light, simulations were run to be compared specifically to a fabricated nanowire sample. For these simulations, the simulated model was designed to match the dimensions of the fabricated structure. Again, the etched dimensions that were measured and used to model the simulation data can be found in Table 1. The primary simulated dip in reflectance seems to align with the measured response, however, the measured samples show a second broad drop in reflectance at lower wavelengths. This suggests that the InSb nanowires are likely absorbing light in the expected ranges, however, the variations in the fabricated sample are causing some additional, undesired antireflection behavior. Figure 28

compares the measured nanowire specular reflection, simulated reflection with fabricated nanowire dimensions, and simulated reflection of an ideal nanowire. The ideal nanowire included in this figure has a diameter close to the top diameter of the measured sample. This provides a frame of reference as to where we expect the peak HE_{11} resonance mode to occur. The same comparative figures for all samples from Figure 25 can be found in Supplementary Figure 11. The reasons for resonant wavelengths being shifted relative to the ideal nanowire geometry will be discussed in the next chapter.

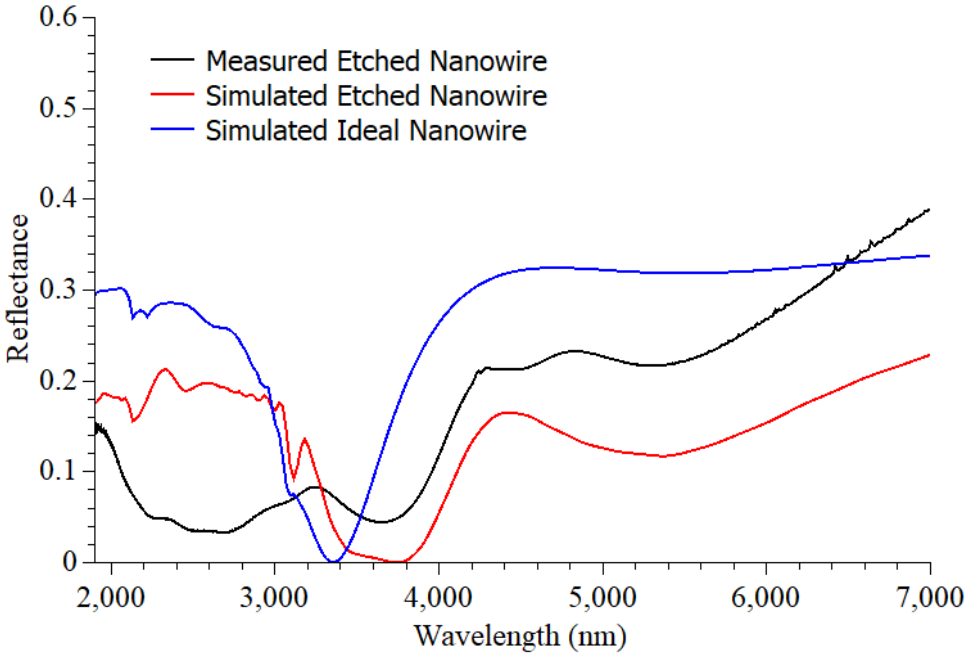

Figure 28. Measured and Simulated Reflection Compared.
Measured reflectance was obtained from an FT-IR microscope using the sample from Figure 25 (d). The intended diameter of the etched nanowires was 500 nm, however, the actual diameter was 610 nm. The geometry of 'Simulated Etched Nanowire' model was designed to match that of the etched sample. The 'Simulated Ideal Nanowire' had a diameter of 600 nm to match closely to the minimum diameter of the etched sample.

Table 1. Measured Dimensions of InSb Nanowire Arrays Used for FTIR and Simulations.

Intended Diameter (nm)	200	300	400	500	600	700	800	900	1000
Top Diameter (nm)	216	408	432	612	580	840	766	999	987
Bottom Diameter (nm)	1105	1155	1276	1266	1550	1870	1916	1913	2240
Nanowire Length (nm)	2767	3490	2706	3696	3106	3943	3946	4090	4105

Intended diameters refer to the diameter of the etching mask. The top diameter was measured at the smallest point, and the bottom diameter at the widest. Nanowire lengths were varied to less etching time for smaller diameters. This was to minimize the impact of re-deposition, however, may have negatively impacted spectral response.

Chapter IV.

Discussion

This chapter revisits aspects of the research that may require further explanation and analysis. It is covered in four sections. The first section will explain why the research focused on measured reflectance of InSb, rather than transmission as well. The second section will detail why the RIE process was chosen, its limitations, how those limitations were addressed, and offer alternative fabrication methods. The third section will provide deeper analysis of why the measured reflectance of the fabricated nanowire arrays varied from the simulated data. The last section will provide future research goals and a brief conclusion.

Optical System Design

InSb Nanowires on an InSb Substrate

As explained in the introduction, a goal of this research is to develop an infrared transmission filter system using InSb nanowire arrays on top of an infrared photodetector. While InSb nanowires would have been ideally etched on top of or embedded in an infrared transparent material to function as infrared transmission filters, fabricating this embodiment would have required resources outside the scope of this research. Bulk InSb wafers are commercially available, whereas infrared transparent wafers with several microns thick InSb are not. Several options were entertained, but ultimately, focus was placed on a proof of concept based on measured reflectance. Having custom wafers fabricated would have been too costly, and while reports of sputtering thin layers of InSb

have also been made (Webb and Halpin, 1985), the sputtering tools available for this project prohibited InSb due to their low vapor pressures, increasing the likelihood of contaminating the tool. Though embedding Si nanowires in a transparent substrate has also been shown (Park, Seo, and Crozier, 2012), this method was successful due to the small, sub-100 nm diameters, and would likely fail due to the larger diameter sizes of the InSb nanowires. Alternate methods of embedding the InSb nanowires in a transparent substrate have been considered, but not yet attempted.

InSb Nanowire Fabrication Process, Successes, Limitations, and Alternatives

InSb Etching Process Selection

Dry etching III-V semiconductor materials can be achieved with several gas chemistries. The RIE tool available for III-V etching during this research had CH_4, H_2, BCl_3, Cl_2, HBr, Ar, O_2, and N_2 gases available. Dry etching InSb with a CH_4/H_2/Ar based process was selected because of numerous reports suggesting advantages over Cl_2 and BCl_3 based dry etching chemistries, and HBr based dry etching chemistries have been much less frequently reported.

The etching mechanisms for these chemistries are well understood in III-V semiconductor materials, including InSb. CH_4, Cl, and Br target group III etchants, in this case, Indium. The expected etch products are $In(CH_3)_3$, $InCl_3$, or $InBr_3$, respectively (Pearton, Chakrabarti, Kinsella, Johnson, & Constantine, 1990; Sun & Kosel, 2012; Vawter & Wendt, 1991). Group V elements, in this case, Antimony, is more readily etched by all of the gases listed above. However due to varying levels of volatility,

expected etch products are SbH_x in the presence of hydrogen, and $SbCl_x$ when chlorine is present. While the chlorine based processes have often reported faster etch rates than CH_4/H_2 processes, it has also been shown that removing the $InCl_3$ etch products can be difficult due to low volatility, and preferential loss of Sb etch products because of its relatively higher volatility (Zhang, Sun, Xu, & Zhao, 2009). Reports of HBr etching processes provide strong evidence for InSb etching (Pearton et al., 1992), however, because of the limited data compared to CH_4/H_2 processes, HBr based etching was not initially pursued.

Disadvantages of CH_4/H_2 etching processes have been reported as potential hydrogen passivation of surface dopants, high mask etch rates, and polymer deposition (Sun & Kosel, 2012). However, as seen in this research, these issues have largely overcome as hard mask fabrication provided adequate etching selectivity, and high chamber temperature inhibits polymer film deposition. Additional support for improved CH_4/H_2 etching processes can be seen in reference (R. C. Keller, Seelmann-Eggebert, & Richter, 1995), as nitrogen was shown to inhibit polymer formation, and in reference (Pusino, Xie, Khalid, Thayne, & Cumming, 2016), that high temperature $CH_4/H_2/Ar$ etching will decrease micro masking and achieved smoother etch surfaces.

InSb Etching Limitations and Successes

Despite the abundance of positive results for etching InSb with CH_4/H_2 chemistries, this research has shown that when etching high aspect ratio InSb nanostructures, this process struggles to achieve a re-deposition free, highly anisotropic etch profile. Since etching vertical sidewalls was achieved, troubleshooting re-deposition

was given closer attention by further investigating the potential sources of re-deposition – low etch product volatility and sputtering. An attempt of etching the InSb samples in an ion beam etcher at room temperature with only Ar provided some insight as to the effects of re-deposition caused via physical sputtering. Figure 29 shows the SEM of the sample after ion beam etching accompanied with EDS analysis comparing the In:Sb ratios comprising the re-deposition. Like the $CH_4/H_2/Ar$ process, the top of the etched structure show both In and Sb, but with great proportions of In. However, the ratio is smaller than measured in the $CH_4/H_2/Ar$ process. While the process parameters differ significantly, these results potentially suggest that the $CH_4/H_2/Ar$ process re-deposition is likely a combination of physical sputtering and at least one another factor.

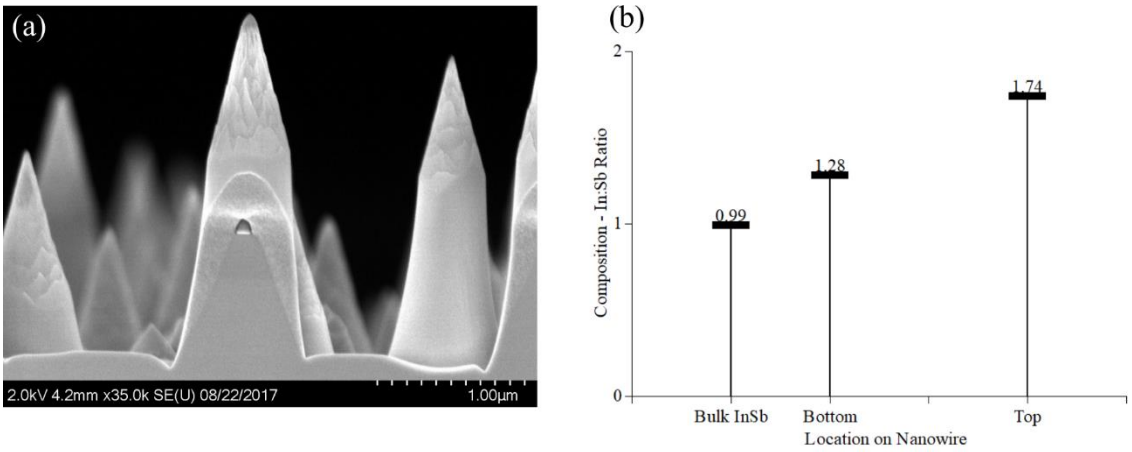

Figure 29. Ion Beam Etching InSb Re-deposition SEM and EDS Analysis.
(a)SEM image after Ar based Ion Beam Etching InSb for 30 minutes at 300 Volts. (b) EDS analysis comparing In:Sb ratios at the top and bottom of the structure.

Comparing melting points of products from several chemistries provides some insight into how effective these processes may be. In doing so, it can be seen that $In(CH_3)_3$ is the likely the most volatile potential product with a melting point of 88° C.

This is followed by $InBr_3$ at 220° C, and lastly $InCl_3$ at 586° C. While the low melting point of $In(CH_3)_3$ may suggest it is a great candidate to etch with, the melting point of indium is 156° C, suggesting there is greater bond strength between indium atoms than that of indium and CH_3. This sheds some light on the high rates of indium re-deposition when etching with the $CH_4/H_2/Ar$ process. It is likely that $In(CH_3)_3$ is decomposing, leaving indium behind, which can often be seen in the form of droplets, adhered to the walls of the nanowires. Additional support for the decomposition of $In(CH_3)_3$ may be found in (McDaniel & Allendorf, 2000) which reports an autocatalytic behavior of $In(CH_3)_3$ at temperatures over 90° C, meaning the decomposition rate of $In(CH_3)_3$ will increase as the produced In will facilitate further decomposition.

Results reported in this thesis have shown the composition of the re-deposited material from a $CH_4/H_2/Ar$ etch process to be both indium and antimony, with greater proportions of indium. The research also provided preliminary data showing that an addition of HBr to the $CH_4/H_2/Ar$ etch process could inhibit a majority of re-deposition, and maintain nearly equal parts indium and antimony after etching. This can be explained by several factors working in conjunction. First, the $InBr_3$ etch products formed are being effectively desorbed, contributing to a decreased presence of $In(CH_3)_3$ etch products. Second, fewer $In(CH_3)_3$ etch products would decrease re-deposition caused by the decomposition of that product. This is supported by the observed increased re-deposition of droplet-like morphology that accompanied an increased etch rate in several samples in Figure F13. This increased etch rate would have produced $In(CH_3)_3$ at higher rates, and therefore likely contributed to greater indium re-deposition. Lastly, the effect of Ar, which is believed to contribute more to desorption of $In(CH_3)_3$ products, may have a

further influenced decreased re-deposition. This could be explained by the proportion of $In(CH_3)_3$ products relative to Ar ions decreased due to the presence of $InBr_3$, which seems to be more readily desorbed during etching.

InSb Nanowire Fabrication Alternatives

In addition to changes in the dry etching processes, such and the $HBr/CH_4/H_2/Ar$ process highlighted above, alternative fabrication methods were considered throughout the course of this research. The most promising alternative to dry etching seems to be electrodeposition. Electrodeposition of InSb nanowires with diameters as small as 30 nm have been reported to be nearly stoichiometric and single crystalline (Khan, Wang, Bozhilov, & Ozkan, 2008). It seems reasonable that this technique could be adapted to create optimally shaped InSb nanowires. An additional benefit to this approach is a potential for depositing the InSb in a material that is transparent to infrared light, potentially clearing two of the most substantial hurdles in this research – fabricating vertical, orderly InSb nanowires that are on top of, or embedded in an infrared transparent material. However, this method may also prove challenging due to a need for fabricating orderly patterned, high aspect ratio holes of specific diameters, to serve as the template for the indium and antimony being deposited.

Spectral Analysis

There are three distinct characteristics of the measured reflectance of the fabricated InSb nanowire arrays, all of which can be seen in Figures 27, 28, and

Supplementary Figure 11. First, the measured reflectance shows HE_{11} dips which are much broader than what was shown in simulations. Second, the primary dip in measured reflectance is consistently shifted to slightly larger wavelengths than the expected HE_{11} wavelengths, as established in simulations. Third, the measured reflectance is lower than expected at wavelengths due to absorption in the pure HE_{11} mode. The first two attributes can be explained by characteristics that have been observed in tapered germanium nanowires (Solanki & Crozier, 2014). Germanium nanowires have been studied with the same approach used in this research. It was shown that introducing a taper to the nanowires, decreased spectral selectivity and broadened the spectral response. Further, they show that for a tapered nanowire, resonant absorption is at a wavelength corresponding to the tip diameter. As the wavelength increases, the resonance smoothly transitions through the nanowire with peak intensity being at the point where the local nanowire diameter allows for HE_{11} resonance. The longest resonant wavelength is given by the nanowire base diameter after which the nanowire no longer absorbs light. Thus, a tapered nanowire shows a much broader optical peak which can be understood as an average of the resonant response of all the diameters from the tip to the base of the nanowire. From this, it is reasonable to expected that by eliminating the large, non-linear taper seen in the measured InSb nanowire arrays, the resonant wavelengths will be in a narrower range. Lastly, the lower than expected reflection seen in wavelengths smaller than the primary dips could be due the fact that the taper of the wires effectively decreased the pitch, which could be creating a coupling effect that decreases reflectance. This behavior might also be attributed to inadequate nanowire lengths, which ended up being shorter than desired relative to their larger than intended diameters. While etch

times were decreased for smaller diameter nanowires to minimize the impact of re-deposition, the large taper may have negatively impacted the spectral response. As discussed in the simulation results sections, the average diameters of a nanowire can dictate the resonate wavelength, and that with a large taper, it is expected that the resonant wavelength will have increased.

Future Research and Conclusion

Future Research

This research will be continued in two pathways. One path is to fabricate the passive transmission filter system proposed in the introduction of this thesis. The second path forward is to move towards developing an active infrared detector based on orderly, vertical, InSb nanowire arrays.

This research presented proof of concept for a passive transmission filter system utilizing patterned InSb nanowire arrays. The next steps will entail optimizing the InSb nanowire etching process to result in a vertical sidewall with no re-deposition. Also, the InSb nanowire arrays must be etched on top of, or be embedded in a substrate that is transparent to the infrared ranges being filters. The fabrication results reported in this thesis support the feasibility of dry etching InSb nanowires. However, as shown, the process is very sensitive to re-deposition, and further optimizations are required to achieve ideal nanowire geometries that will yield greater spectral sensitivity. Preliminary data supports that an addition of HBr to the $CH_4/H_2/Ar$ process could resolve the dry etching issues. Producing InSb nanowire arrays on or in a transparent substrate will first

be attempted by dry etching a InSb layer that was sputtered on to an infrared transparent substrate. Though limited, there is support for depositing InSb via sputtering (B. Webb & Halpin, 1985; Giulian et al., 2017). The alternate fabrication methods utilizing electro deposition of InSb nanowire, as previously mentioned, would require substantially more development, but could be a suitable alternative to dry etching if ideal nanowire geometries remain elusive.

There are many hurdles in the way of engineering an active infrared sensor based on InSb nanowires, however, this remains a stretch goal for this research. A means of fabricating nanowires on a transparent substrate is, again, required. Even more complex, a nanowire based active device would have to be designed to collect the photocurrent which is generated by InSb nanowires. This would require creating nanowires with some form of a junction to separate charge carriers, or work in the photoconductive mode to get an electrical response. This leads to the need for integrated circuitry that can carry the photocurrent away from the nanowire-based pixels. With these considerations, it is likely too complicated for one-off prototyping, and may first require adapting the concept to existing infrared sensors.

Conclusions

The primary goal of this research was to provide a proof of concept for a passive infrared transmission filter system based on InSb nanowires. Optical simulations confirmed that InSb nanowires can be geometrically tuned to serve as spectrally selective absorbers in the near and mid infrared range. These simulations established that InSb nanowires with ideal, non-tapered, geometries can selectively absorb wavelengths from 1

μm to 6 μm with reasonable absorption intensity and reflection response. An ICP-RIE dry etching process capable of fabricating InSb nanowires was developed. This process does, however, require additional optimizations do resolve lingering issues with re-deposition and tapering. Lastly, with FT-IR measured reflectance of InSb nanowire arrays, we report spectrally selective shifts with changing nanowire diameters. While these results do suffer from the imperfect nanowire geometries, they do agree well with simulated reflectance data. This research provides a strong case for using InSb nanowire arrays as spectrally selective infrared filters and absorbers.

Appendix 1.

Supplementary Figures.

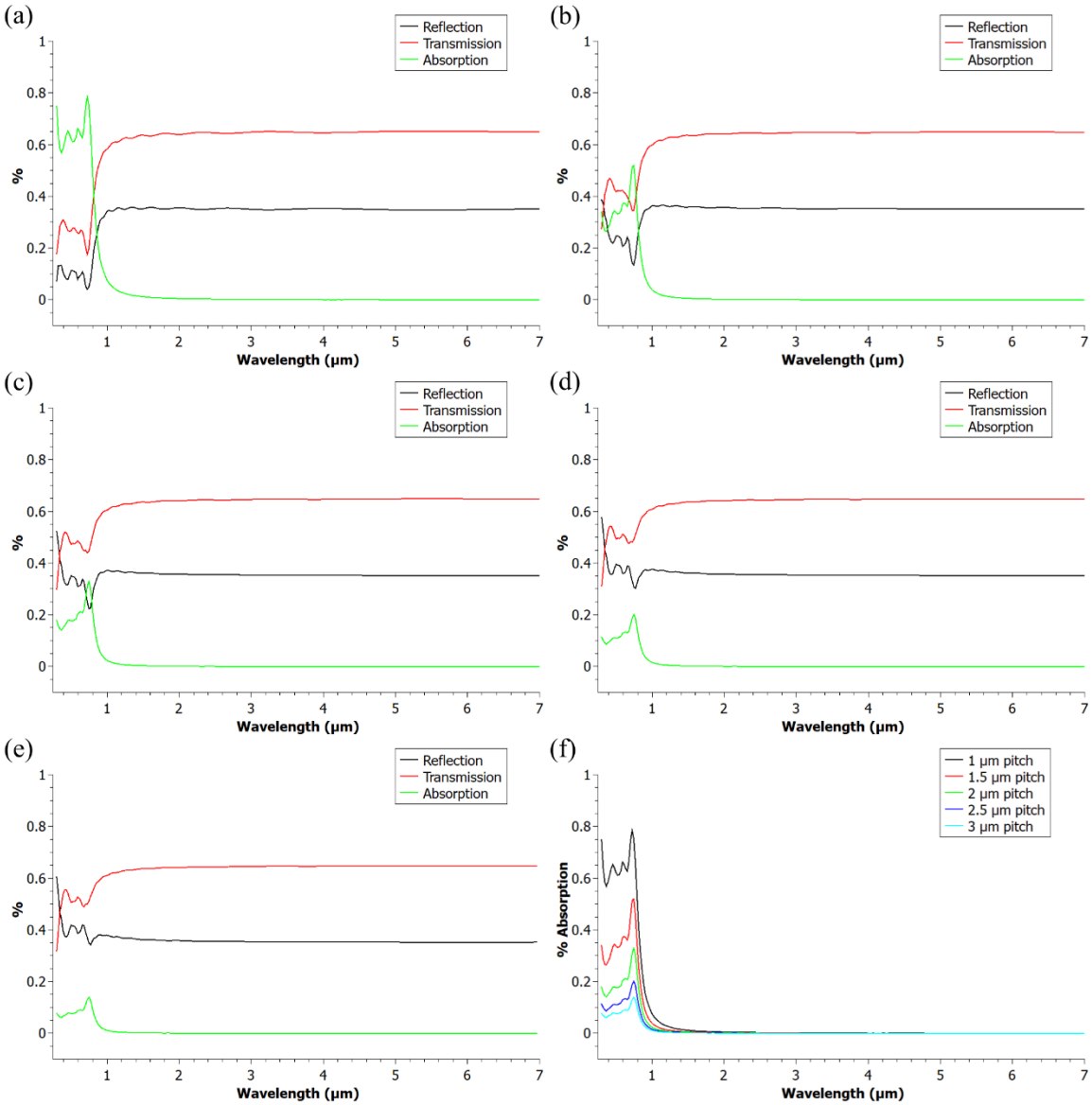

Supplementary Figure 1. Simulated spectral response of a 100 nm diameter nanowire array with varied pitch

(a) 1 µm pitch. (b) 1.5 µm pitch. (c) 2 µm pitch. (d) 2.5 µm pitch. (e) 3 µm pitch. (f) Percent absorption for each simulated pitch with a 100 nm diameter nanowire.

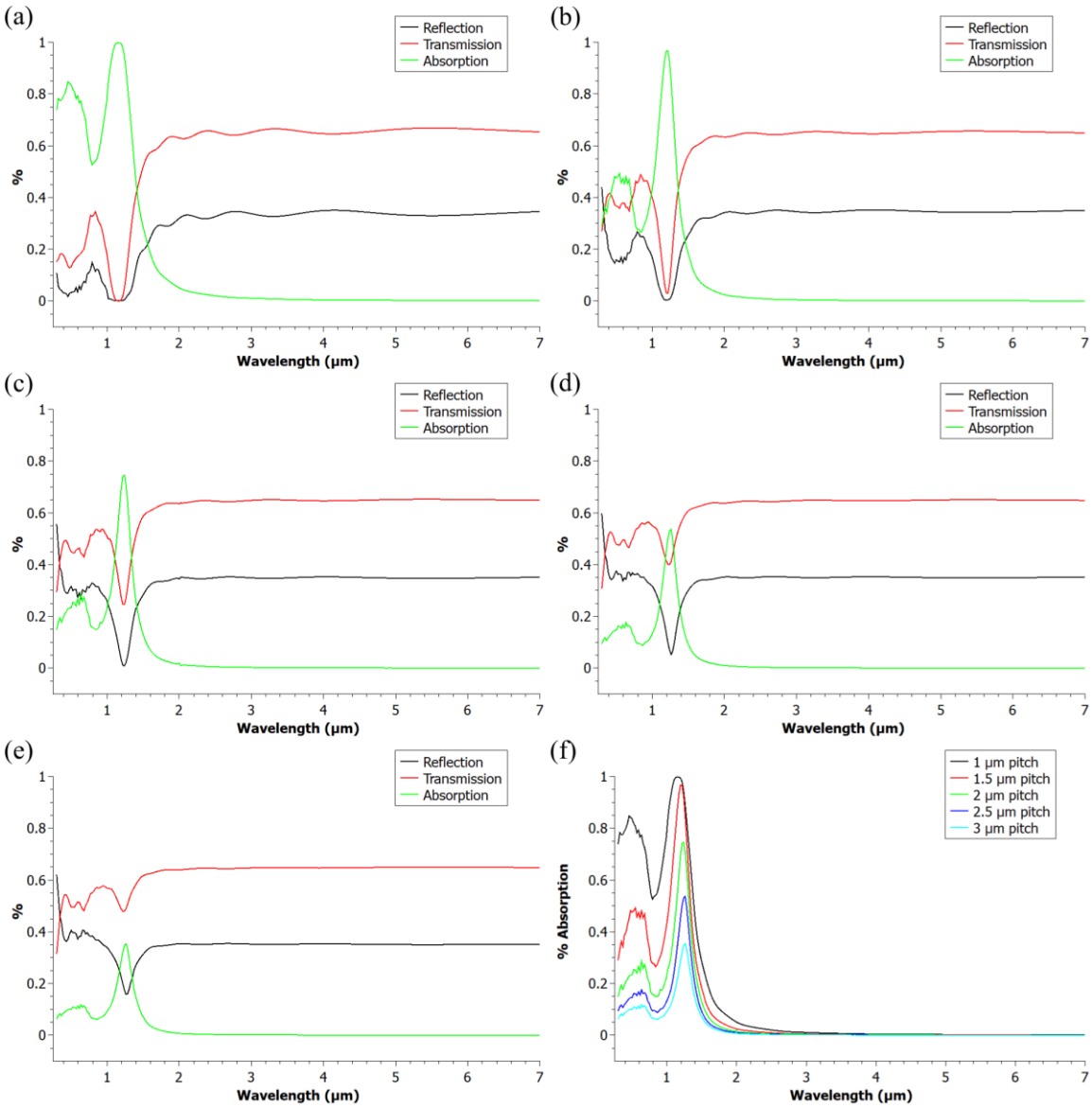

Supplementary Figure 2. Simulated spectral response of a 200 nm diameter nanowire array with varied pitch

(a) 1 µm pitch. (b) 1.5 µm pitch. (c) 2 µm pitch. (d) 2.5 µm pitch. (e) 3 µm pitch. (f) Percent absorption for each simulated pitch with a 200 nm diameter nanowire.

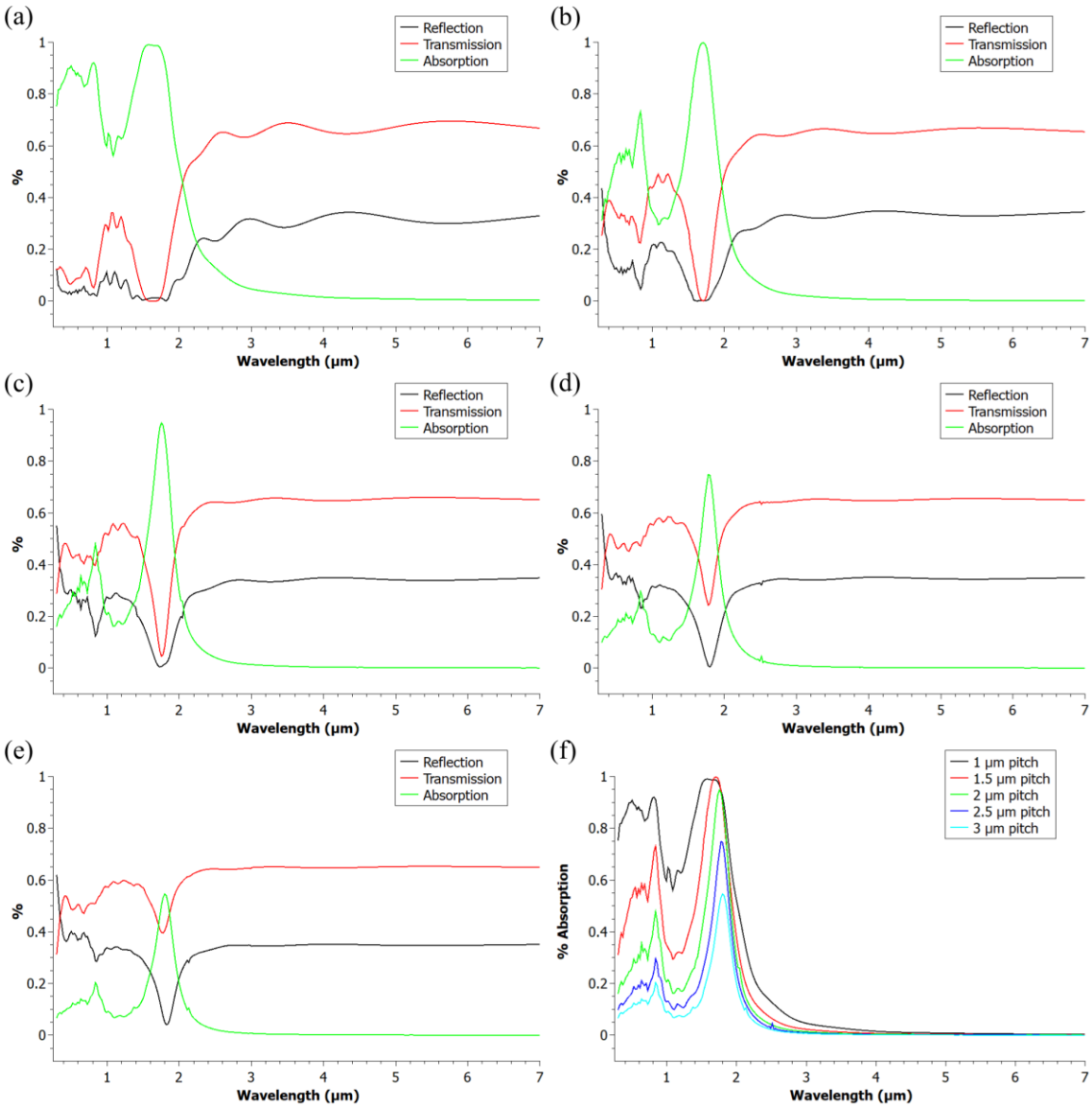

Supplementary Figure 3. Simulated spectral response of a 300 nm diameter nanowire array with varied pitch

(a) 1 µm pitch. (b) 1.5 µm pitch. (c) 2 µm pitch. (d) 2.5 µm pitch. (e) 3 µm pitch. (f) Percent absorption for each simulated pitch with a 300 nm diameter nanowire.

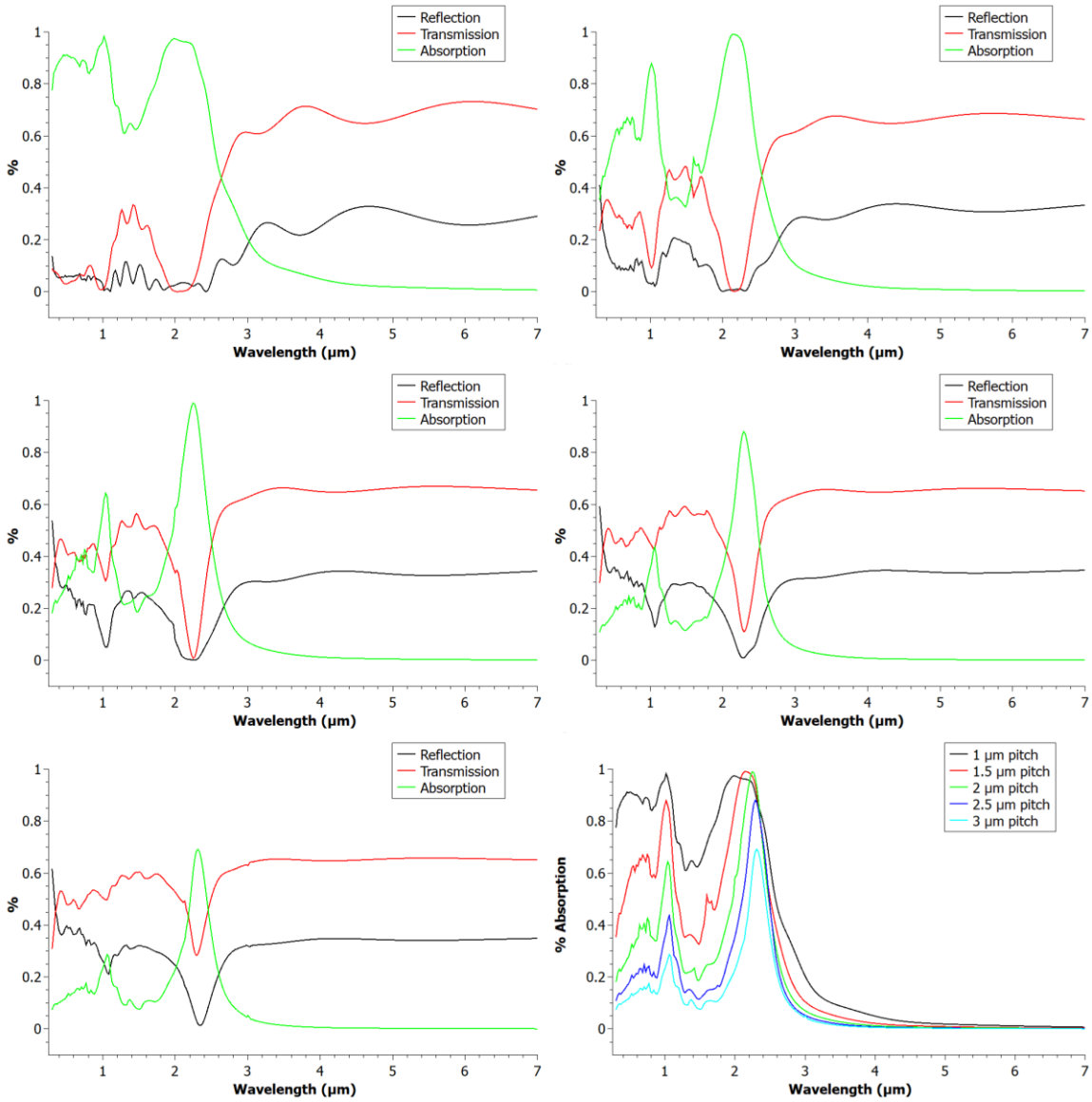

Supplementary Figure 4. Simulated spectral response of a 400 nm diameter nanowire array with varied pitch

(a) 1 µm pitch. (b) 1.5 µm pitch. (c) 2 µm pitch. (d) 2.5 µm pitch. (e) 3 µm pitch. (f) Percent absorption for each simulated pitch with a 400 nm diameter nanowire.

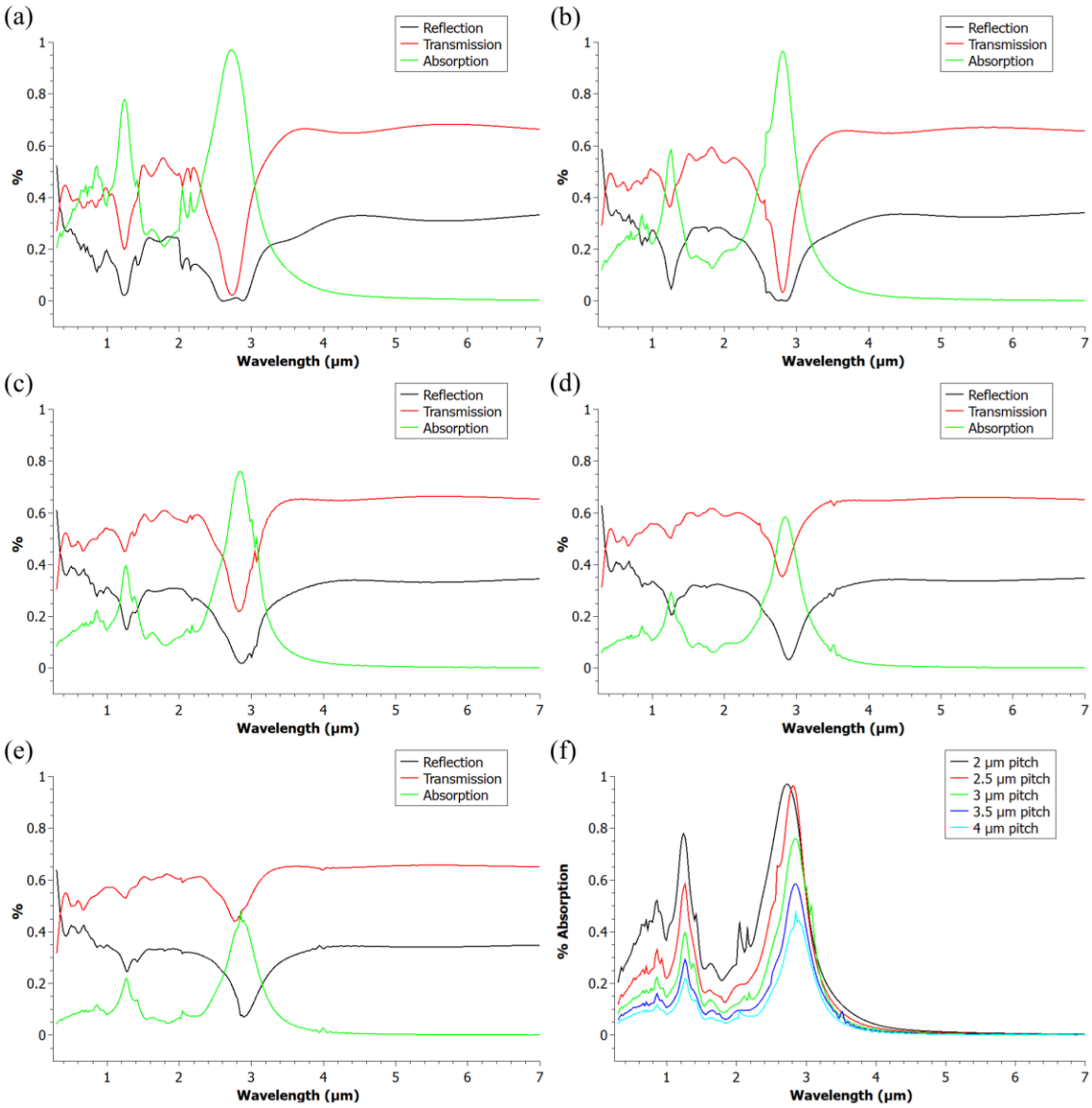

Supplementary Figure 5. Simulated spectral response of a 500 nm diameter nanowire array with varied pitch

(a) 2 µm pitch. (b) 2.5 µm pitch. (c) 3 µm pitch. (d) 3.5 µm pitch. (e) 4 µm pitch. (f) Percent absorption for each simulated pitch with a 500 nm diameter nanowire.

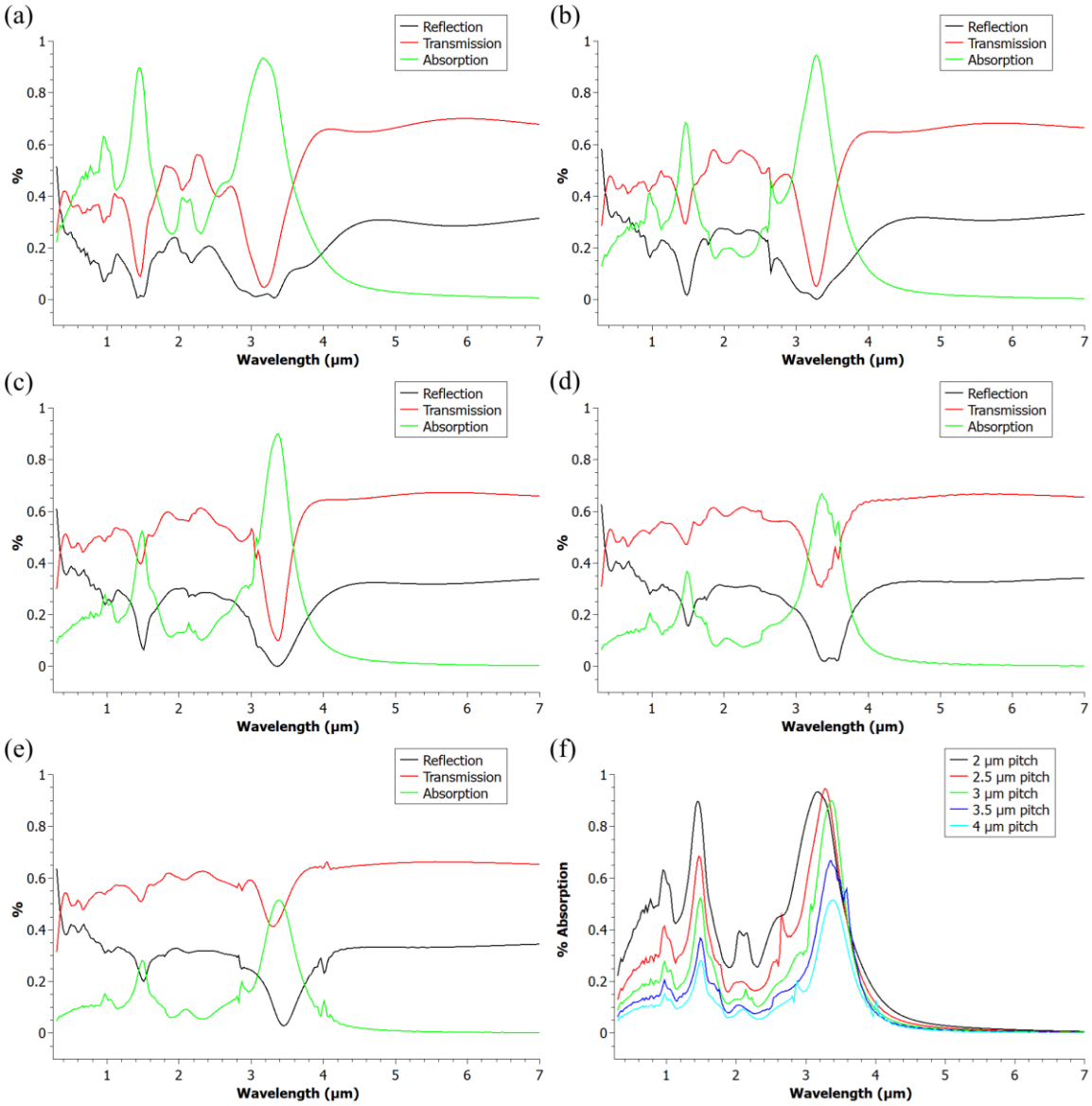

Supplementary Figure 6. Simulated spectral response of a 600 nm diameter nanowire array with varied pitch

(a) 2 µm pitch. (b) 2.5 µm pitch. (c) 3 µm pitch. (d) 3.5 µm pitch. (e) 4 µm pitch. (f) Percent absorption for each simulated pitch with a 600 nm diameter nanowire.

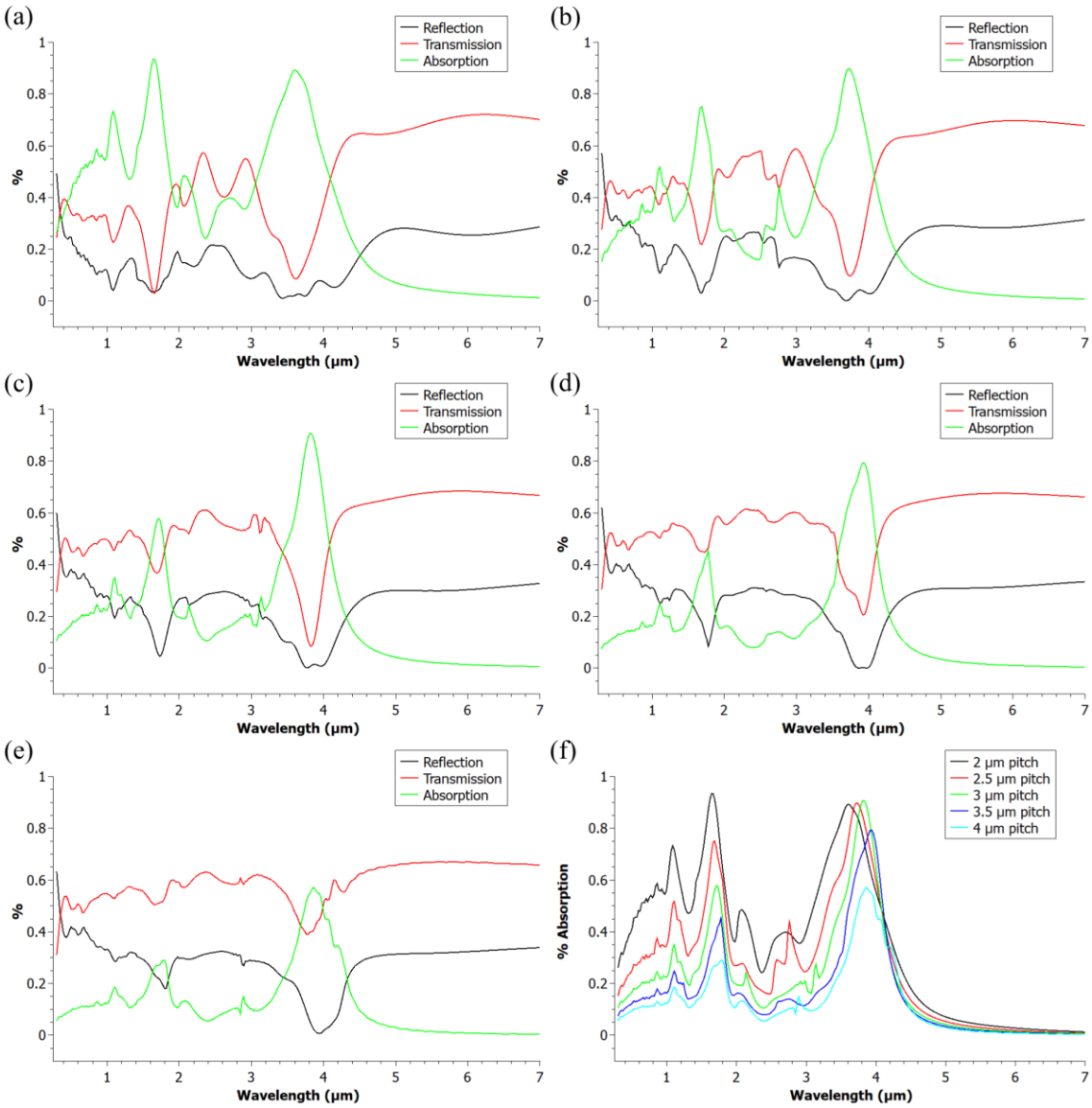

Supplementary Figure 7. Simulated spectral response of a 700 nm diameter nanowire array with varied pitch

(a) 2 µm pitch. (b) 2.5 µm pitch. (c) 3 µm pitch. (d) 3.5 µm pitch. (e) 4 µm pitch. (f) Percent absorption for each simulated pitch with a 700 nm diameter nanowire.

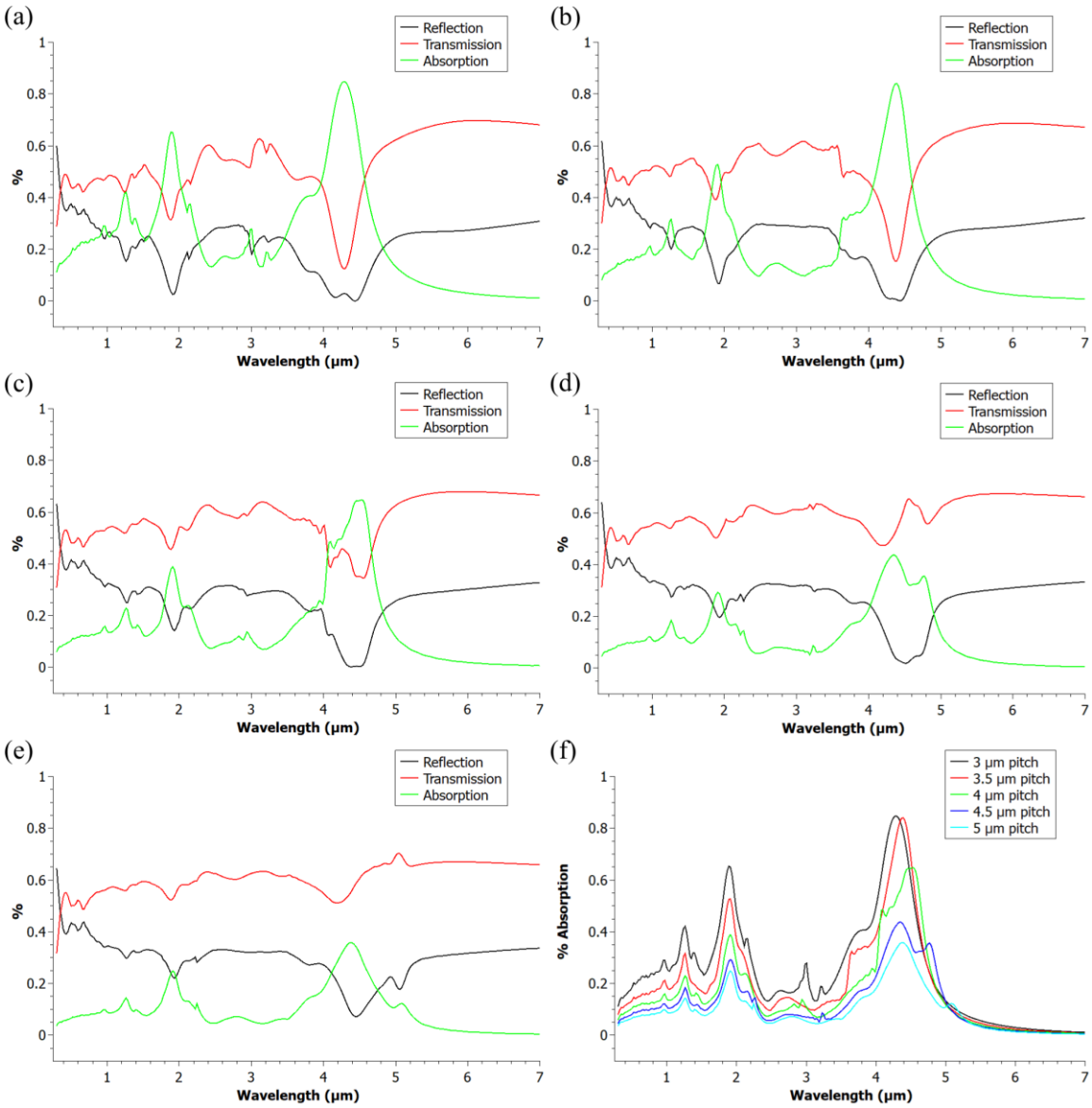

Supplementary Figure 8. Simulated spectral response of an 800 nm diameter nanowire array with varied pitch

(a) 3 µm pitch. (b) 3.5 µm pitch. (c) 4 µm pitch. (d) 4.5 µm pitch. (e) 5 µm pitch. (f) Percent absorption for each simulated pitch with an 800 nm diameter nanowire.

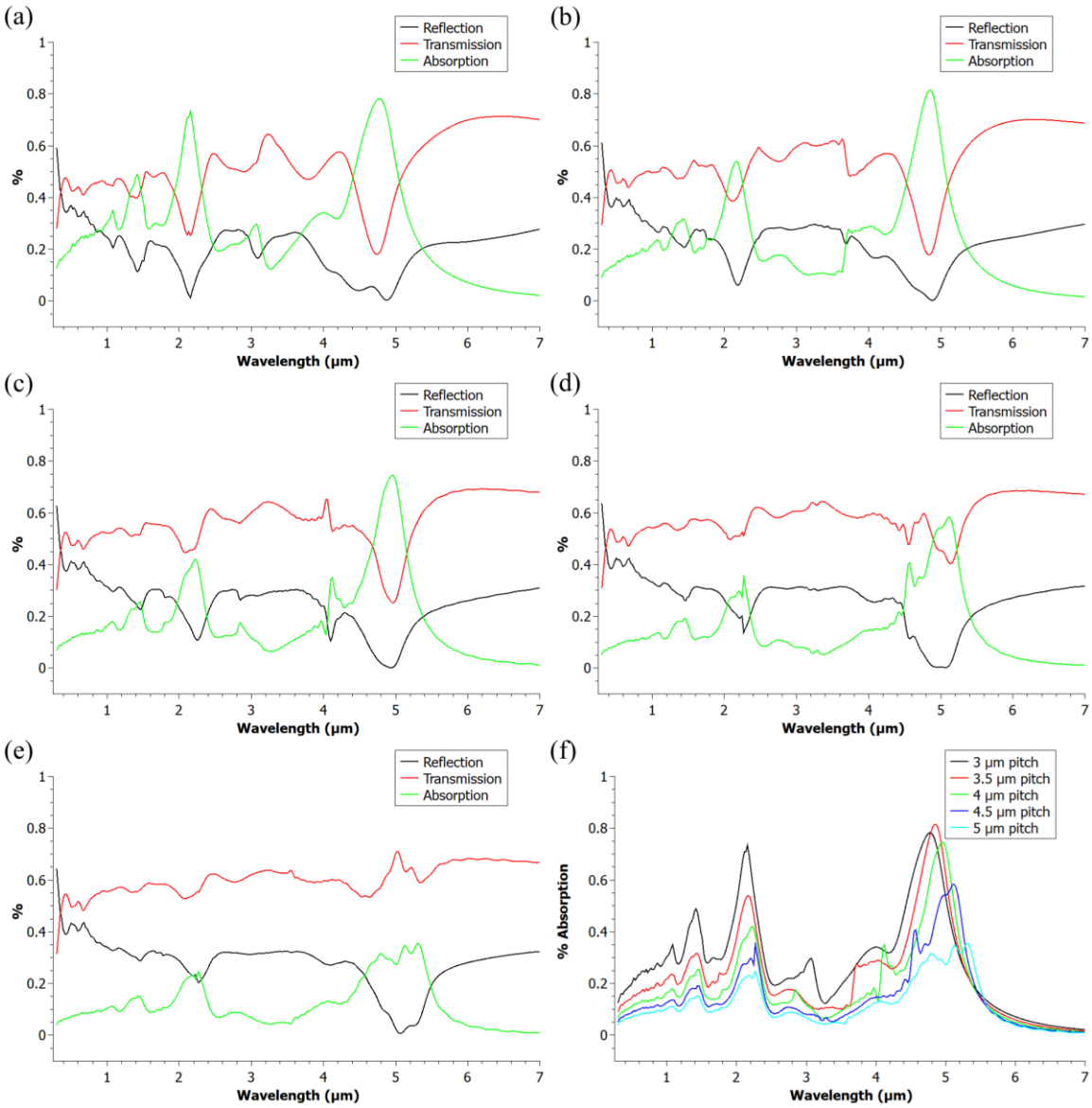

Supplementary Figure 9. Simulated spectral response of a 900 nm diameter nanowire array with varied pitch

(a) 3 µm pitch. (b) 3.5 µm pitch. (c) 4 µm pitch. (d) 4.5 µm pitch. (e) 5 µm pitch. (f) Percent absorption for each simulated pitch with a 900 nm diameter nanowire.

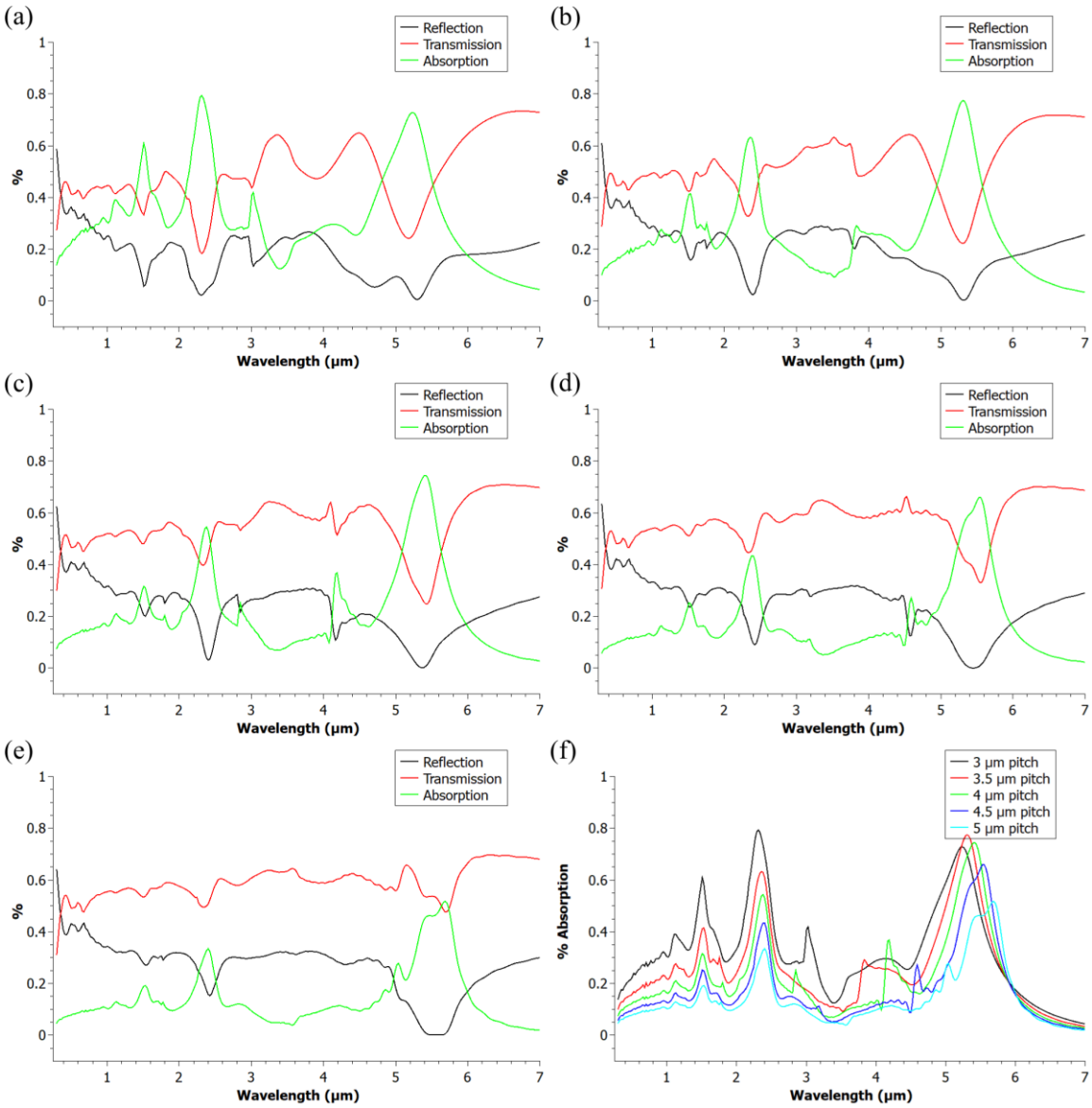

Supplementary Figure 10. Simulated spectral response of a 1000 nm diameter nanowire array with varied pitch

(a) 3 µm pitch. (b) 3.5 µm pitch. (c) 4 µm pitch. (d) 4.5 µm pitch. (e) 5 µm pitch. (f) Percent absorption for each simulated pitch with a 1000 nm diameter nanowire.

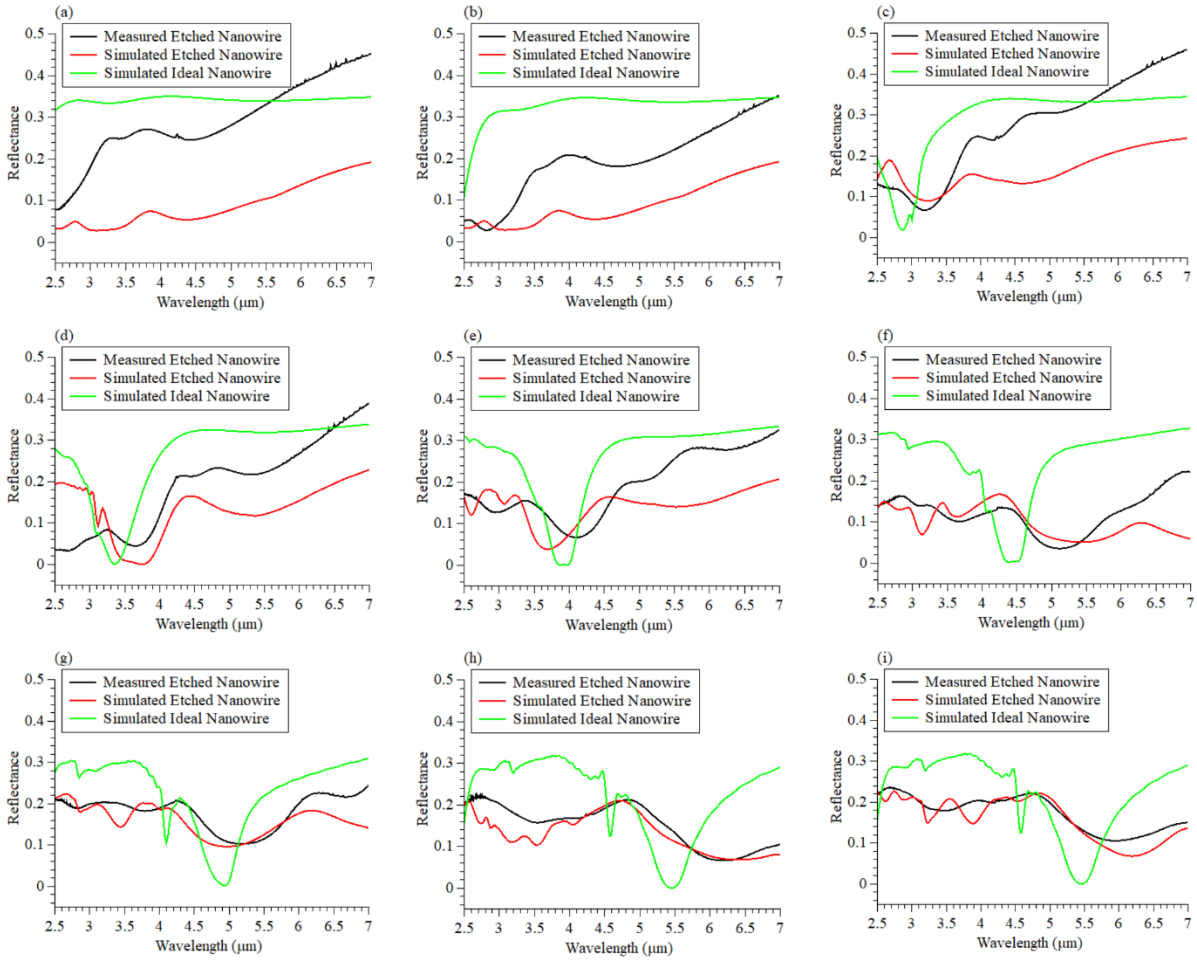

Supplementary Figure 11. Measured reflectance of etched InSb nanowires compared to simulated reflectance

(a) 200 nm intended diameter etched and simulated, compared with a 300 nm diameter ideal nanowire (b) 300 nm intended diameter etched and simulated, compared with a 400 nm diameter ideal nanowire (c) 400 nm intended diameter etched and simulated, compared with a 500 nm diameter ideal nanowire (d) 500 nm intended diameter etched and simulated, compared with a 600 nm diameter ideal nanowire (e) 600 nm intended diameter etched and simulated, compared with a 700 nm diameter ideal nanowire (f) 700 nm intended diameter etched and simulated, compared with a 800 nm diameter ideal nanowire (g) 800 nm intended diameter etched and simulated, compared with a 900 nm diameter ideal nanowire (h) 900 nm intended diameter etched and simulated, compared with a 1000 nm diameter ideal nanowire (i) 1000 nm intended diameter etched and simulated, compared with a 1000 nm diameter ideal nanowire

Table 1. CH_4/H_2/Ar Reactive Ion Etching Processes.

Name	CH_4 (sccm)	H_2 (sccm)	Ar (sccm)	Pressure (mTorr)	Platen Power (W)	Coil Power (W)	Temperature (°C)
13 (a)	15	50	5	7	100	600	20
13 (b)	15	50	5	7	100	600	20
13 (c)	10	50	5	7	100	600	20
13 (d)	10	50	5	7	100	600	20
14 (a)	10	50	5	15	20	800	20
14 (b)	15	50	5	15	20	800	20
14 (c)	25	50	5	15	20	800	20
14 (d)	25	50	5	15	100	800	20
15 (a)	15	50	5	7	100	600	20
15 (b)	15	50	5	7	100	600	130
16 (a)	5	50	5	10	100	800	130
16 (b)	9.2	45.8	5	10	100	800	130
16 (c)	12.7	42.3	5	10	100	800	130
16 (d)	15.7	39.3	5	10	100	800	130
16 (e)	18.3	36.7	5	10	100	800	130
16 (f)	20.6	34.4	5	10	100	800	130
16 (g)	22.6	32.4	5	10	100	800	130
17	15.7	39.3	5	10	100	800	130
18 (a)	15.7	39.3	5	10	100	800	130
18 (b)	15.7	39.3	5	10	200	800	130
18 (c)	15.7	39.3	5	10	275	800	130
18 (d)	15.7	39.3	15	10	100	800	130
19 (a)	15.7	39.3	5	10	275	800	130
19 (b)	15.7	39.3	5	10	275	800	160

19 (c)	15.7	39.3	15	10	275	800	160
20 (a)	5	50	5	30	200	800	160
20 (b)	9.2	45.8	5	30	200	800	160
20 (c)	12.7	42.3	5	30	200	800	160
20 (d)	15.7	39.3	5	30	200	800	160
20 (e)	18.3	36.7	5	30	200	800	160
20 (f)	20.6	34.4	5	30	200	800	160
20 (g)	22.6	32.4	5	30	200	800	160
20 (h)	24.4	30.6	5	30	200	800	160
20 (i)	26.1	28.9	5	30	200	800	160
21 (b)	9.2	45.8	5	30	200	800	160
21 (c)	12.7	42.3	5	30	200	800	160
21 (d)	15.7	39.3	5	30	200	800	160
22 (b)	12.7	42.3	20	30	200	800	160
22 (c)	12.7	42.3	40	30	200	800	160
22 (d)	12.7	42.3	40	30	200	800	160
24 (a)	12.7	42.3	5	10	50	800	160
24 (b)	12.7	42.3	5	10	100	800	160
24 (c)	12.7	42.3	5	10	200	800	160
24 (d)	12.7	42.3	40	10	50	800	160
24 (e)	12.7	42.3	40	10	100	800	160
25	12.7	42.3	40	10	100	800	160

This table contains all $CH_4/H_2/Ar$ based RIE processes that were referenced through the fabrication results section. The name in first column corresponds to the specific figure that the process was used in.

Table 2. HBr Reactive Ion Etching Processes.

Name	HBr	CH_4 (sccm)	H_2 (sccm)	Ar (sccm)	Pressure (mTorr)	Platen Power (W)	Coil Power (W)	Temperature (°C)
26 (a)	5	12.7	42.3	40	10	100	800	160
26 (b)	2	12.7	42.3	40	10	100	800	160

This table contains any RIE processes that included HBr. The Name of the process corresponds to the resulting figure.

References

Abautret, J., Evirgen, A., Perez, J.-P., Laaroussi, Y., Cordat, A., Boulard, F., & Christol, P. (2015). Gas mixture influence on the reactive ion etching of InSb in an inductively coupled methane-hydrogen plasma. *Semiconductor Science and Technology*, *30*(6), 65014. https://doi.org/10.1088/0268-1242/30/6/065014

Adachi S. Optical dispersion relations for GaP, GaAs, GaSb, InP, InAs, InSb, $Al_xGa_{1-x}As$, and $In_{1-x}Ga_xAs_yP_{1-y}$, *J. Appl. Phys.* 66, 6030-6040 (1989)

Averill, B., & Eldredge, P. (2013). *General Chemistry: Principles, Patterns and Applications*. Retrieved from https://images.flatworldknowledge.com/averillfwk/averillfwk-fig06_004.jpg. Accessed November 15, 2017.

Azizur-Rahman, K. M., & Lapierre, R. R. (2015). Wavelength-selective absorptance in GaAs, InP and InAs nanowire arrays. *Nanotechnology*. https://doi.org/10.1088/0957-4484/26/29/295202

Azizur-Rahman, K. M., & Lapierre, R. R. (2016). Optical design of a mid-wavelength infrared InSb nanowire photodetector. *Nanotechnology*. https://doi.org/10.1088/0957-4484/27/31/315202

B. Webb, J., & Halpin, C. (1985). *Deposition of indium antimonide films by metalorganic magnetron sputtering*. *Applied Physics Letters* (Vol. 47). https://doi.org/10.1063/1.95999

Cao, L., White, J. S., Park, J.-S., Schuller, J. A., Clemens, B. M., & Brongersma, M. L. (2009). Engineering light absorption in semiconductor nanowire devices. *Nature Materials*, *8*(8), 643–647. https://doi.org/10.1038/nmat2477

Carr, J. A., Valdez, T. A., Bruns, O. T., & Bawendi, M. G. (2016). Using the shortwave infrared to image middle ear pathologies. *Proceedings of the National Academy of Sciences*, *113*(36), 9989–9994. https://doi.org/10.1073/pnas.1610529113

Chen, H., Sun, X., Lai, K. W. C., Meyyappan, M., & Xi, N. (2009). Infrared detection using an insb nanowire. *2009 IEEE Nanotechnology Materials and Devices Conference, NMDC 2009*, 212–216. https://doi.org/10.1109/NMDC.2009.5167558

Diniz, J. ., Swart, J. ., Jung, K. ., Hong, J., & Pearton, S. . (1998). Inductively coupled plasma etchingof in-based compound semiconductorsin CH4/H2/Ar. *Solid-State Electronics*, *42*(11), 1947–1951. https://doi.org/10.1016/S0038-1101(98)00136-1

Fouad, K. (2014). A practical approach to reactive ion etching. *Journal of Physics D: Applied Physics*, *47*(23), 233501. https://doi.org/10.1088/0022-3727/47/23/233501

Giulian, R., Manzo, D. J., Salazar, J. B., Just, W., Andrade, A. M. H. de, Schoffen, J. R., … Bernardi, F. (2017). Structural and electronic characterization of antimonide films made by magnetron sputtering. *Journal of Physics D: Applied Physics*, *50*.

Green M.A. Self-consistent optical parameters of intrinsic silicon at 300K including temperature coefficients, *Sol. Energ. Mat. Sol. Cells* 92, 1305–1310 (2008)

Hahn, Y. B., Hays, D. C., Cho, H., Jung, K. B., Lambers, E. S., Abernathy, C. R., … Shul, R. J. (2000). Inductively Coupled Plasma Etching in ICL- and IBr-Based Chemistries. Part II: InP, InSb, InGaP, and InGaAs. *Plasma Chem. Plasma Process.*, *20*(3), 417–427.

Hu, J., Odom, T. W., & Lieber, C. M. (1999). Chemistry and physics in one dimension: Synthesis and properties of nanowires and nanotubes. *Accounts of Chemical Research*, *32*(5), 435–445. https://doi.org/10.1021/ar9700365

Huang, Z., Fang, H., & Zhu, J. (2007). Fabrication of Silicon Nanowire Arrays with Controlled Diameter, Length, and Density. *Advanced Materials*, *19*(5), 744–748. https://doi.org/10.1002/adma.200600892

Jain, V., Nowzari, A., Wallentin, J., Borgström, M. T., Messing, M. E., Asoli, D., … Pettersson, H. (2014). Study of photocurrent generation in InP nanowire-based p+-i-n+ photodetectors. *Nano Research*, *7*(4), 1–9. https://doi.org/10.1007/s12274-014-0422-2

Keller, J. (2014). Infrared Sensors Blending with Signal Processing to Yield New Levels of Surveillance. *Military & Aerospace Electronics*, (January).

Keller, R. C., Seelmann-Eggebert, M., & Richter, H. J. (1995). Addition of N2 as a polymer deposition inhibitor in CH 4/H2 electrocyclotron resonance plasma etching of Hg 1-xCdxTe. *Applied Physics Letters*. https://doi.org/10.1063/1.115371

Khan, M. I., Wang, X., Bozhilov, K. N., & Ozkan, C. S. (2008). Templated fabrication of InSb nanowires for nanoelectronics. *Journal of Nanomaterials*. https://doi.org/10.1155/2008/698759

Law, M., Goldberger, J., & Yang, P. (2004). Semiconductor Nanowires and Nanotubes. *Annual Review of Materials Research*, *34*(1), 83–122. https://doi.org/10.1146/annurev.matsci.34.040203.112300

McDaniel, A. H., & Allendorf, M. D. (2000). Autocatalytic behavior of trimethylindium during thermal decomposition. *Chemistry of Materials*. https://doi.org/10.1021/cm990497f

Mileham, J. R., Lee, J. W., Lambers, E. S., & Pearton, S. J. (1997). Dry etching of GaSb and InSb in CH 4 /H 2 /Ar. *Semicond. Sci. Technol*, *12*, 338–344.

Park, H., Dan, Y., Seo, K., Yu, Y. J., Duane, P. K., Wober, M., & Crozier, K. B. (2014). Filter-free image sensor pixels comprising silicon nanowires with selective color absorption. *Nano Letters*. https://doi.org/10.1021/nl404379w

Park, H., Seo, K., & Crozier, K. B. (2012). Adding colors to polydimethylsiloxane by embedding vertical silicon nanowires. *Applied Physics Letters*, *101*(19). https://doi.org/10.1063/1.4766944

Park, H. (2016). Vertical Silicon Nanowires for Image Sensor Applications.

Pearton, S. J. (1996). Comparison of dry etching techniques for III-V semiconductors in CH4, H2, Ar plasmas. *J. Electrochem. Soc.*, *134*(2), 19960201.

Pearton, S. J., Chakrabarti, U. K., Kinsella, A. P., Johnson, D., & Constantine, C. (1990). Electron cyclotron resonance plasma etching of InP in CH4/H2/Ar. *Applied Physics Letters*, *56*(15), 1424–1426. https://doi.org/10.1116/1.585026

Pearton, S. J., Chakrabarti, U. K., Lane, E., Perley, A. P., Abernathy, C. R., & Hobson, W. S. (1992). Characteristics of III-V Dry Etching In HBr-Based Discharges. *Journal of the Electrochemical Society*, *139*(3).

Pusino, V., Xie, C., Khalid, A., Thayne, I. G., & Cumming, D. R. S. (2016). Development of InSb dry etch for mid-IR applications. *Microelectronic Engineering*, *153*, 11–14. https://doi.org/10.1016/j.mee.2015.12.014

Rode, D. L. (1971). Electron transport in InSb, InAs, and InP. *Physical Review B*, *3*(10), 3287–3299. https://doi.org/10.1103/PhysRevB.3.3287

Rogalski, A. (2002). Infrared detectors: An overview. *Infrared Physics and Technology*, *43*(3–5), 187–210. https://doi.org/10.1016/S1350-4495(02)00140-8

Rogalski, A. (2011). *Infrared Detectors* (Second Edi). CRC Press.

Seeger, K. (2004). *Semiconductor Physics: An Introduction (9th Edition)* (Eighth Edi). Springer Verlag Berlin Heidelberg.

Selçuk, E. (2009). *Guided and Deterministic Self Organization of Quantum Dots*. https://doi.org/10.6100/IR642818

Seo, K., Wober, M., Steinvurzel, P., Schonbrun, E., Dan, Y., Ellenbogen, T., & Crozier, K. B. (2011). Multicolored vertical silicon nanowires. *Nano Letters*, *11*(4), 1851–1856. https://doi.org/10.1021/nl200201b

Shafa, M., Akbar, S., Gao, L., Fakhar-E-Alam, M., & Wang, Z. M. (2011). Indium Antimonide Nanowires: Synthesis and Properties. https://doi.org/10.1186/s11671-016-1370-4

Solanki, A., & Crozier, K. (2014). Vertical germanium nanowires as spectrally-selective absorbers across the visible-to-infrared. *Applied Physics Letters*, *105*(19). https://doi.org/10.1063/1.4901438

Sprafke, T., & Beletic, J. (2008). High Performance Infrared Focal Plane Arrays. *Optics & Photonics News*, *19*(6).

Sun, J., & Kosel, J. (2012). Room temperature inductively coupled plasma etching of InAs/InSb in BCl 3/Cl 2/Ar. *Microelectronic Engineering*, *98*(October), 222–225. https://doi.org/10.1016/j.mee.2012.07.018

Svensson, J., Anttu, N., Vainorius, N., Borg, B. M., & Wernersson, L. E. (2013). Diameter-dependent photocurrent in InAsSb nanowire infrared photodetectors. *Nano Letters*, *13*(4), 1380–1385. https://doi.org/10.1021/nl303751d

Vawter, G. A., & Wendt, J. R. (1991). Chlorine reactive ion beam etching of InSb and InAs0.15Sb0.85/InSb strained-layer superlattices. *Applied Physics Letters*, *58*(3), 289. https://doi.org/10.1063/1.104664

Vázquez-Guardado, A., Money, M., Mckinney, N., & Chanda, D. (2015). Multi-spectral infrared spectroscopy for robust plastic identification. *Applied Optics*. https://doi.org/10.1364/AO.54.007396

Wilson, R. H., Nadeau, K. P., Jaworski, F. B., Rowland, R., Nguyen, J. Q., Crouzet, C., … Durkin, A. J. (2014). Quantitative short-wave infrared multispectral imaging of *in vivo* tissue optical properties. *Journal of Biomedical Optics*, *19*(8), 86011. https://doi.org/10.1117/1.JBO.19.8.086011

Wook Shin, H., Jun Lee, S., Gun Kim, D., Bae, M.-H., Heo, J., Jin Choi, K., … Cheol Shin, J. (2015). Short-wavelength infrared photodetector on Si employing strain-induced growth of very tall InAs nanowire arrays. *Scientific Reports*, *5*(April), 10764. https://doi.org/10.1038/srep10764

Xiao, H. (2012). *Introduction to Semiconductor Manufacturing Technology* (Second Edi). SPIE Press.

Yariv, A., & Yeh, P. (1984). *Optical waves in crystals: propagation and control of laser radiation*. *John Wiley Sons Inc New York* (Wiley Clas, Vol. 12). John Wiley & Sons, Inc. https://doi.org/10.1109/JQE.1984.1072309

Zhang, G.-D., Sun, W.-G., Xu, S.-L., & Zhao, H.-Y. (2009). Inductively coupled plasma-reactive ion etching of InSb using CH 4 / H 2 / Ar plasma. *American Vacuum Society*, 681–685. https://doi.org/10.1116/1.3143664